Study of bone-metal interface in orthopaedic application using spectral CT

Maya Rajeswari Amma

Te Whare Wānanga o Otāgo

NEW ZEALAND

A thesis submitted for the degree of

Doctor of Philosophy

at the University of Otago, Christchurch,

New Zealand.

January 2020

I dedicate this thesis to my
kind loving mother (Ms. Rajeswari Amma), inspiring husband (Mr. Vivek Nair) and adorable sons (Surya Nair and Sree Nair)

Abstract

This thesis investigates the diagnostic potential of MARS spectral photon counting computed tomography (CT) in assessing musculoskeletal disorders such as bone fractures and crystal arthritis. The hypothesis states that the high spatial resolution, quantitative material specific information and reduced metal artefacts of spectral photon counting CT makes the MARS spectral CT scanner a promising imaging tool to confirm or rule out a diagnosis.

Being a new imaging modality, a protocol to scan samples with metal implants has to be optimised, before it can be implemented clinically for patient imaging. I contributed to optimising a protocol for imaging bone-implant specimens. Different biomaterials (titanium and stainless steel) used for fracture fixation were imaged. The artefacts were evaluated in both the energy and material domain. A bone analysis tool for measuring bone morphological parameters such as trabecular thickness and spacing was developed in collaboration with the Human Interface Technology Lab. Bone healing at the bone-metal interface was studied and the results were compared with plain radiographs, dual energy x-ray absorptiometry and clinical single and dual energy CT. The advantages of photon counting spectral CT in the early assessment of bone healing due to reduced artefacts was demonstrated.

This thesis also investigated the potential of spectral photon counting CT to differentiate calcium crystals present in phantoms and osteoarthritic human meniscus samples. Our results show that MARS spectral CT can moderately discriminate calcium pyrophosphate (crystals inducing pseudogout) and calcium hydroxyapatite crystals. The results were compared with plain radiographs, polarised light microscopy and x-ray diffraction methods.

In conclusion, this thesis demonstrated the clinical potential of MARS preclinical spectral photon counting CT scanner for the non-invasive and non-destructive imaging of bone-metal interfaces, for early assessment of bone healing, and for the detection and characterisation of articular crystals.

Acknowledgements

I would like to express my sincere gratitude to Prof. Anthony Butler and Prof. Phil Butler for recognising my potential and giving me an opportunity to conduct research with the first commercial photon counting spectral CT scanner 'MARS'. Special thanks to the University of Otago for awarding the Doctoral Scholarship and providing all the educational resources to complete the project. I would like to acknowledge my supervisors Prof. Anthony Butler, Dr. Aamir Raja, Dr. Benjamin Bamford and Dr. Nigel Anderson for their constant support, motivation and valuable feedback.

My heartfelt thanks to all the MARS team members who contributed in delivering a well calibrated scanner for imaging, software, and tools and techniques for data analysis and image visualisation. My sincere gratitude to MARS group members Dr. Raj Panta, Ms. Aysouda Matanaghi, Ms. Jenifer Clarke, Dr. Jonathan Crighton, Dr. Hannah Prebble, Dr. Stuart Lansley, Dr. Mahdieh Moghiseh, Dr. Marzieh Anjoumroz, Mr. Praveenkumar Kanithi, Dr. Niels de Ruiter, Dr. Alexander Chernoglazov, Dr. Harish Mandalika, Dr. Srinidhi Bheesette, Dr. Ali Atharifard, Mr. Brian Goulter, Dr. Stephen Bell and Dr. Robert Doesburg for their insightful discussions and encouragement to this research. I would also like to thank Dr. Peter Walker and all the national and international collaborators for offering the samples mentioned in this thesis.

I am thankful to Dean Dr. Rachel Sproken Smith for constantly monitoring my research progress and encouraging me to strive hard throughout. I thank the Divison of Health Sciences, MBIE, MedTech CoRE and the University of Otago for providing grants to present the research at national and international conferences. I would also like to thank Ms. Ruth Helms, Ms. Sam Gurney and Mr. Peter Hilton for giving advices and administrative support for completing the course. Special thanks to Ms. Sam Gurney for her time and patience in proofreading this thesis.

Finally, my sincere gratitude to my family and friends for their endless love, support and encouragement.

Scientific contributions

Peer reviewed Publications/Conference Proceedings

1. **Amma M. R**, Anthony P. H. Butler, Aamir Y. Raja, Benjamin Bamford, Philip Butler, et al. Assessment of metal implant induced artefacts using photon counting spectral CT, Proc. SPIE 11113, Developments in X-Ray Tomography XII, 111131D (September 2019); doi: 10.1117/12.2531003 (Conference Proceedings)
   This paper presents the experimental study on metal implant induced artefacts using MARS spectral CT. The novelty of the research was in identifying whether MARS scanner has the potential to accurately measure concentrations of bone equivalent materials in the vicinity of the implant. I contributed to the study conception and design, data collection and processing, analysis and interpretation. I am the primary author of this conference proceedings and presented this work on 15th August, 2019 at SPIE Optics and Photonics conference in San Diego.

2. Stamp, L. K., Anderson, N. G., Becce, F., **Rajeswari, M.**, Polson, M., Guyen, O., Viry,A., Choi, C., Kirkbride, T. E., and Raja, A. Y. Clinical utility of multi-energy spectral photon-counting CT in crystal arthritis. (2019)71. 10.1002/art.40848. Arthritis and Rheumatology (Journal article).
   This article discusses the clinical utility of MARS scanner in differentiating gout and pseudogout. I was involved in data acquisition, analysis and interpretation, and manuscript revision. The image of the gouty finger in this article was the **cover page of the journal** published in July 2019.

3. R.Aamir, A.Viry, T.E.Kirkbride, **M. Rajeswari**, L.Stamp, M.Polson, O.Guyen, F. Becce, N. Anderson. Characterisation of calcium crystal types in osteoarthritic meniscus at spectral photon-counting CT. Proceedings of European Society of Radiology (ESR) 2018, http://dx.doi.org/10.1594/ecr2018/C-1731 (Conference

proceedings)
This proceeding highlights the classification of different calcium crystal types present in an osteoarthritic human knee meniscus using MARS CT. This study shows that MARS spectral CT can noninvasively differentiate calcium hydroxyapatite and calcium pyrophosphate crystals present in the meniscus. I collaborated with Anais Viry, PhD student, Lausanne University, Switzerland for scanning the human meniscus specimens. I contributed to further processing the datasets in the MARS imaging chain including data collection, processing, image analysis and image visualisation.

4. Becce F, Viry, Anais, K Stamp, Lisa, Pascart Tristan, Francois Jean, Sikiru A Adebileje, Steven D Alexander, **Maya R Amma**, Marzieh Anjomrouz et.al. Winds of change in imaging of calcium crystal deposition diseases. Joint Bone Spine (May 2019), https://doi.org/10.1016/j.jbspin.2019.04.005 (Journal article)
This article emphasises the potential of MARS CT in the diagnosis of crystal arthritis and calcific periarthritis/tendonitis, and to provide a better understanding and deeper insights into the possibly pathogenic role that various calcium crystals play within joints in vivo, including in osteoarthritis. I contributed to scanning synthetic crystal samples using the MARS scanner and in the preparation of the images.

5. Butler, Philip H and Adebileje, Sikiru A and Alexander, Steven D and **Amma, Maya R** and Amjomrouz, Marzieh and Asghariomabad, Fatemeh and Atharifard, Ali and Atlas, James and Bamford, Benjamin and Bell, Stephen T et al. MARS preclinical imaging: the benefits of small pixels and good energy data. Developments in X-Ray Tomography XII, 11113, 111130C, International Society for Optics and Photonics, 2019 (Conference proceedings)
This proceeding presents the benefits of improved specificity and sensitivity of the MARS scanner and its applications in preclinical imaging. My contribution was in the data acquisition, data analysis and image interpretation of applications discussed under bone-implant imaging.

6. Panta, Raj Kumar , Butler, Anthony , Butler, Philip , Ruiter, Niels Bell, Stephen , Walsh, Michael , Doesburg, Robert , Chernoglazov, Alexander , Goulter, Brian , Carbonez, Damet, Jérôme Adebileje, Sikiru , Alexander, Steven , **Rajeswari Amma, Maya** Anjomrouz, Marzieh , Asghariomabad, Fatemeh , Atharifard, Ali , Baer, Kenzie , Bamford, Benjamin , Woodfield, Tim. (2018). First human

imaging with MARS photon-counting CT. 1-7. 10.1109/NSSMIC.2018.8824513 (Conference Proceedings).

The proceedings demonstrate the translation of MARS preclinical scans to human imaging. I assisted in scanning the human ankle and performed the data analysis using in-built MARS MD.

Contribution as a team member of MARS Collaboration

As a member of MARS Collaboration, I assisted students in calibrating the scanner by performing pixel masking prior to data acquisition, familiarised them with the MARS imaging chain, and trained them on in-house developed image processing tools. Additionally, I helped the MARS development team in testing new software releases and contributed in the preparation of user manuals for the MARS scanner and for data analysis. The following proceedings demonstrate this contribution.

7. Searle, Emily K., et al. Distinguishing Iron and Calcium using MARS Spectral CT. IEEE Nuclear Science Symposium and Medical Imaging Conference Proceedings (NSS/MIC). IEEE, 2018.

8. Lowe, Chiara D., et al. MARS pulmonary spectral molecular imaging: potential for locating tuberculosis involvement. IEEE Nuclear Science Symposium and Medical Imaging Conference Proceedings (NSS/MIC). IEEE, 2018.

9. Moghiseh, Mahdieh, et al. Cancer Imaging with Nanoparticles Using MARS Spectral Scanner. IEEE Nuclear Science Symposium and Medical Imaging Conference Proceedings (NSS/MIC). IEEE, 2018.

10. Bheesette, Srinidhi, et al. Medipix3RX neutron camera for ambient radiation measurements in the CMS cavern. IEEE Nuclear Science Symposium and Medical Imaging Conference Proceedings (NSS/MIC). IEEE, 2018.

Under preparation

11. **Amma, M. R** et al: Spectral photon counting CT to assess bone-metal interfaces.

    This paper demonstrates that the MARS preclinical scanner can facilitate the assessment of bone-metal interface with fewer artefacts, and quantify bone mineral density (BMD) and morphology simultaneously. I contributed to study design, data analysis and interpretation. I collaborated with the HIT Lab,

University of Canterbury, in developing a bone analysis tool for measuring bone architectural parameters which is integrated into MARS Vision for future users. I am the primary author of this paper.

12. **Amma, M. R** et al: Assessment of bone healing at the bone-metal interface using spectral photon counting CT.
    This paper presents the benefits of using photon counting spectral CT for assessing early fracture healing at the bone-metal interface. I contributed to scanning of the samples and quantitative and qualitative evaluation of bone healing. I am the primary author of this paper.

Published abstracts

1. **Amma, M. R**, Tara Dalefield, Aliakbar Atharifard, Aamir Younus Raja, Nigel Anderson, Benjamin Bamford, Anthony Butler. Optimisation of parameters for imaging bone metal interface using spectral photon counting computed tomography. Journal of Medical Radiation Sciences,Volume 65,116-117.

2. **M.Rajeswari Amma**, C Leary and the MARS collaboration. Bone strength assessment using MARS spectral CT. UOC Postgraduate Students Symposium (July 2018, Christchurch, New Zealand)

3. **Maya Rajeswari Amma**, Tara Dalefield, Aamir Younus Raja, Nigel Anderson,Anthony Butler. Spectral CT Imaging of bone and implants using MARS CT. University of Otago Student Research Symposium (August 2017, Dunedin, New Zealand).

4. Matanaghi, Aysouda, Aamir Raja, Celeste Leary, **Maya Rajeswari Amma**, Raj Panta, Marzieh Anjomrouz, Mahdieh Moghiseh, Anthony Butler, Benjamin Bamford, and MARS Collaboration. Semi-automatic quantitative assessment of site-specific bone health using spectral photon counting CT. Journal of Nuclear Medicine 60, no. supplement 1 (2019): 1297-1297.

As a team member of MARS Collaboration

5. Vanden Broeke, Lieza and the MARS Team: Calibrating MARS Cameras using X-ray Fluorescence. Proceedings of the 20th International Workshop on Radiation Imaging Detectors, Sundsvall, Sweden, June 2018.

6. Raja, A and the MARS team: Spectral CT imaging using CZT Medipix3RX. Proceedings of the 20th International Workshop on Radiation Imaging Detectors, Sundsvall, Sweden, June 2018.

7. Ali, A. and the MARS team: Pulse pile up models for spectral X-ray imaging. Proceedings of the 20th International Workshop on Radiation Imaging Detectors, Sundsvall, Sweden, June 2018.

8. Chamber, C and the MARS team: Quantifying Phosphorous and calcium in fossils using MARS imaging. NZIP and PHYSIKOS conference, Christchurch, April 2019.

9. Adebileje, S and the MARS team: Dictionary Learning to reduce dose in MARS datasets. NZIP and PHYSIKOS conference, Christchurch, April 2019.

10. Duncan, N and the MARS team: Imaging of geological samples using MARS scanner. NZIP and PHYSIKOS conference, Christchurch, April 2019.

11. Sreedharan, J and the MARS team: Improving the accuracy of MARS reconstruction algorithm. NZIP and PHYSIKOS conference, Christchurch, April 2019.

Presentations

1. **Amma, M. R**. Study of bone health using MARS spectral CT. 3 Minute Thesis competition held at the University of Otago, Christchurch, New Zealand, July 2017.

2. **Amma, M. R**. MARS- An emerging imaging modality to study bone metal interface presented at the Australian and New Zealand Society of Nuclear Medicine (ANZSNM) Branch Meeting, Hamilton, New Zealand, September 2017.

3. **Amma, M. R**. Study of bone health using MARS SPCCT delivered to medical students at Christchurch school of Medicine, Christchurch, New Zealand, November 2017.

4. **Amma, M. R**. Bone analysis. MARS research group seminar, Department of Physics and Astronomy, University of Canterbury, Christchurch, New Zealand, March, 2018.

5. **Amma, M. R**. Imaging of crystal induced arthritis using MARS spectral CT. 3 Minute Thesis competition held at the University of Otago, Christchurch, New Zealand, July 2018.

6. **Amma, M. R**. Bone implant imaging. MARS Spectral CT Workshop held at Christchurch, New Zealand, November 2018.

7. **Amma, M. R**. Advantages of photon counting spectral CT in assessing bone-metal interfaces, CMDT Emerging Researcher Award presentation, MedTech CoRE Day, Health Tech Week, Auckland, July 2019.

8. **Amma, M. R**. Colour x-rays for medicine presented to U3A members, Christchurch, November 2019.

Scientific Collaborations

Local Collaboration

1. Christchurch Regenerative Medicine and Tissue Engineering (CReaTE) Group, University of Otago, Christchurch, NZ.
   I collaborated with this group to scan titanium scaffolds to determine bone growth in the vicinity of the implant. This collaboration has led to a conference proceeding presented at SPIE Optics and Photonics, San Diego, 2019.

2. The Human Interface Technology Laboratory (HIT Lab), University of Canterbury, Christchurch, New Zealand.
   I collaborated with this group to develop a bone analysis tool integrated to MARS visualisation software for analysing bone morphology and bone strength.

3. Department of Mechanical Engineering, University of Canterbury, Christchurch, New Zealand.
   I collaborated with the Orthomag group to scan biodegradable magnesium screws to investigate the potential of MARS scanner to identify biodegradability of the screw.

4. Lincoln University, Christchurch, New Zealand.
   I collaborated with Dr. Nadia Mitchel and Dr. Samantha Murray to scan sheep samples to compare the potential of MARS scanner in imaging bone-metal interface with clinical single and dual energy CT.

5. St. George's Hospital, Christchurch, New Zealand.
   I collaborated with Ms. Jenifer Clarke (Radiographer) to validate the clinical applicability of MARS scanner in imaging bone healing at the bone-metal interface.

6. Christchurch Hospital, Christchurch, New Zealand.
   Dr. Alex Malone, Orthopaedic surgeon, Christchurch hospital provided the titanium and stainless steel implants used in this study.

7. Southern Cross Hospital, Christchurch, New Zealand.
   I presented the concept of MARS scanner to an Orthopaedic surgeon Dr Ram Chandru. I could successfully demonstrate the need of this tool and, as a result, he has visited our facilities and agreed to provide volunteers for our clinical trial.

International Collaboration

1. Oregon State University and Oregon Health and Science University, USA.
   I worked with Celeste Leary, PhD student from this group in preprocessing, post-processing and data analysis of bone samples for bone strength assessment.

2. Institute of Radiation Physics, Lausanne University Hospital, Lausanne, Switzerland.
   The osteoarthritic knee meniscus samples were obtained through this research collaboration. This study has led to two journal articles and a conference proceeding.

Industrial Collaboration

I shared my results using implants with orthopaedic implant manufacturers (Ossis Ltd.) and gave a demonstration of MARS Vision and the bone analysis tool. The results of sheep specimens with bone implants and comparison with clinical single and dual energy CT as proof of concept positively influenced the collaboration.

Student Supervision

1. Tara Dalefield
   Assessment of bone ingrowth in titanium implants using MARS spectral CT.
   Master's Student, University of Canterbury, Christchurch, 2018.

2. Bradon Noordanus
   Characterisation, Quantification and Mapping of Calcium Crystals in

Osteoarthritic Knees using the MARS Spectral CT.
Summer student, University of Canterbury, Christchurch, 2019.

3. Joosje de Bakker
Characterisation of crystal-induced arthropathies using MARS imaging.
Intern student, University of Twente, Netherlands, 2019.

Award/Grant

1. University of Otago Doctoral Scholarship award to support my PhD research since February 2017.

2. Received appreciation mail from Professor Rachel Spronken-Smith, Dean, Graduate Research School, University of Otago, twice for outstanding progress report.

3. Division of Health Sciences, University of Otago Travel grant for research presentation at SPIE conference, San Diego, August 2019.

4. Finalist of the CMDT Emerging Researcher Award conducted by MedTech CoRE to promote novel and outstanding research.

List of Figures

List of Tables

Contents

Chapter 1

Introduction

1.1 Aim and significance of research

The aim of this research is to investigate the diagnostic potential of spectral photon counting CT for bone health analysis. This is significant because musculoskeletal disorders are the leading cause of disability which costs New Zealand more than 5,570 million dollars per year Bosley and Miles (2009). The musculoskeletal disorder is any injury or pain that affects the musculoskeletal system including bones, joints and muscles. Such musculoskeletal disorders include bone fractures, osteoarthritis, rheumatoid arthritis and osteoporosis. Imaging is an important tool to confirm or rule out a diagnosis. Existing imaging modalities have limitations in the quantitative and qualitative evaluation of musculoskeletal disorders such as osteoporosis, bone fractures and crystal arthritis. This research explores the diagnostic potential of photon counting spectral CT in addressing these clinical problems. Photon counting spectral CT has demonstrated its potential as a clinical tool for reducing radiation dose Symons *et al.* (2016), quantifying different tissues and biomarkers of diseases Chen *et al.* (2011), measurement of cartilage health Rajendran *et al.* (2017), soft tissue imaging of atherosclerosis Zainon *et al.* (2012) and reducing metal artefacts Rajendran *et al.* (2014).

The National Institute of Health (NIH) defines osteoporosis as a skeletal disease identified by low bone density and deterioration of bone microarchitecture.

Simultaneous measurement of bone mineral density (BMD) and structure has always been a clinical problem. There are different imaging techniques namely radiographs, Dual Energy X-ray Absorptiometry (DXA), Quantitative Computed Tomography (QCT), Magnetic Resonance Imaging (MRI) and Computed Tomography (CT), to diagnose bone diseases. Bone x-rays are the fastest and easiest way to assess bone injuries and diagnose bone cancer, but determination of osteoporosis and detection of bone contusion can be difficult using radiography Lohman *et al.* (2001). DXA is considered as the gold standard for diagnosing osteoporosis and predicting fracture risk. While DXA measures areal bone density (milligrams per square centimetre of BMD), QCT measures volumetric bone density (milligrams per cubic centimetre of BMD) which makes it an excellent method for prediction of vertebral fractures when compared to DXA Kalkwarf *et al.* (2011). Also disorders such as spinal degenerative diseases, obesity and aortic calcification in patients can result in high BMD measurements in DXA Pappou *et al.* (2006).

In clinical CT, when x-rays pass through metal implants, many physical effects such as beam hardening, photon starvation and partial volume effects cause artefacts Fornaro *et al.* (2011). Beam hardening artefact is caused by absorption of low energy photons Bechara *et al.* (2012). Photon starvation is observed as streaks in highly attenuating regions due to insufficient number of photons reaching the detector Mori *et al.* (2013). Partial volume effects occur when high contrasting materials lie in the same CT voxel thereby producing attenuation values proportional to the average of these materials Kuhnigk *et al.* (2006). Due to these artefacts, the accurate quantification of bone growth near metal implants is not possible. MRI provides better soft tissue information than CT but causes image artefacts which limits its diagnostic utility in evaluating bone-metal interface Hargreaves *et al.* (2011).

Non-invasive characterisation of crystals by imaging tissues is desirable as it would facilitate faster detection of articular cartilage crystals. Conventional radiology is less sensitive and provides 2D images and may miss calcium crystals in small joints Freire *et al.* (2018). Dual energy CT has shown some promise in crystal detection at high concentrations whereas detection between calcium crystal types (calcium pyrophosphate and calcium hydroxyapatite) is still a challenge Nicolaou *et al.* (2010);

Rajiah *et al.* (2019). Due to less sensitivity and specificity, calcification is not well visualised in articular tissues during MRI scans Dirim *et al.* (2013). Ultrasound imaging is an ideal tool to diagnose and monitor rheumatic diseases including gout Codreanu and Enache (2015) but it can be challenging to distinguish gout from pseudo gout Löffler *et al.* (2015). Since pseudo gout is a clinically heterogeneous form of arthritis, accurate differentiation of crystals will facilitate capability of noninvasive diagnosis.

My research can be categorised into two parts: the study of bone health with and without implants. The study of bone health with implants included optimisation of imaging parameters for studying bone-metal interface and assessing the effect of artefacts on bone density measurements in the presence of implants. I optimised a protocol for imaging bone with implants. Our research has led to the development of a bone analysis tool for quantitative evaluation of bone health. Osseointegration at the bone-implant interface was quantified and compared with plain radiographs, clinical CT and iDXA. Our results of bone with plate and multiple screws (titanium and stainless steel) shows that the MARS spectral photon counting CT can assess bone-metal interface with less pronounced artefacts compared to existing imaging modalities. Study of bone health without implants dealt with the assessment of crystal induced arthritis and quantification of density and morphology of bone for assessing bone health. Our studies on excised osteoarthritic knee samples have proved that spectral photon counting CT has the potential to diagnose crystal arthritis noninvasively. The long term goal of this research is to facilitate improved diagnosis of bone-metal interfaces and complications arising due to joint replacements and implant loosening using MARS spectral photon counting CT scanner.

The key research questions of my thesis are:

1. Can MARS spectral photon counting CT detect the effect of factors such as temperature and decalcification on bone density and morphology?

   Previous studies using MARS spectral CT have proved that the accuracy of trabecular thickness measurement is not affected by the orientation of the sample. The effect of change in temperature (frozen and thawed samples)

and decalcification on quantification of bone health was not studied before. We studied the effect of these external factors to evaluate bone density and structural parameters. Our studies also contributed to the development of a semi-automated tool in the MARS visualisation software for the assessment of bone micro-architecture such as trabecular thickness and spacing.

2. Is MARS photon counting CT able to qualitatively and quantitatively assess tissue density at the bone-metal interface?
   Previous studies on metal samples with MARS spectral CT have demonstrated that reconstructing images in narrow high energy bins will reduce metal artefacts. I optimised a protocol for imaging bone specimens with implant. I also assessed the impact of metal artefacts on the density of samples adjacent to orthopaedic implants. The clinical potential of MARS spectral CT scanner in assessing bone-metal interface was compared with plain radiographs and single and dual energy clinical CT. The quantification of bone healing in the vicinity of the implant was studied and validated against iDXA.

3. Can MARS spectral CT differentiate different types of crystals present in osteoarthritic knee samples?
   Previous studies have shown that MARS can differentiate monosodium urate (MSU) and calcium pyrophosphate (CPPD) crystals. The challenge lies in separating CPPD and calcium hydroxyapatite (HA) due to its similar atomic number and densities. Our results shows that spectral CT can moderately discriminate different calcium crystals.

1.2 Background

On November 8, 1895, Wilhelm Conrad Roentgen announced the discovery of rays (x-rays) which could penetrate skin and visualise the skeleton. Since then, x-rays have been extensively used by physicians around the world for diagnosing broken bones and in radiation therapy. Advances in imaging modalities and analytic techniques using x-rays increased the potential for noninvasive study of bone anatomy and physiology.

When an x-ray passes through a material five basic interactions occur; namely photoelectric effect, Compton scattering, Rayleigh scattering, Thompson scattering and pair production. The two major form of interactions in which diagnostic x-ray interact with tissue are photoelectric effect and Compton scattering. Photoelectric effect is the dominant interaction for x-rays with energies below 30 keV and Compton scattering for energies above 30 keV. As the x-ray beam passes through a tissue, photons gets absorbed. According to Beer Lambert's law, the amount of radiation that passes through the tissue is given by

$$I = I_0 e^{-\mu x},$$

where I is the intensity of the measured radiation, I_0 is the intensity of the incident radiation, μ is the linear attenuation coefficient and x is the distance travelled by the photon through the tissue. The linear attenuation coefficient (μ) measures the amount of photon beam absorbed or scattered while passing through a tissue.

Sir Godfrey Hounsfield is considered as the co-inventor of computer-assisted or computerised axial tomography (CAT), who was awarded the Nobel prize for his accomplishment in medicine in 1979 Shampo and Kyle (1996). According to Richmond (2004), by 1973 the CT scanners were used clinically, first for the brain and then, after modification, for whole body imaging. Conventional CT uses a polychromatic x-ray beam (70 to 140 kVp) emitted from a source and received by a detector. As an x-ray beam passes through an object, it is attenuated according to variations in material density, composition and the energy distribution of the beam. In clinical CT, the linear attenuation coefficients (μ) is converted to Hounsfield units (HU) to normalise image intensity with respect to water as

$$HU = ((\mu - \mu_{water})/(\mu_{water} - \mu_{air})) \times 1000$$

HU of water is defined as 0, air as -1000 and bone as +1000. Detectors used in traditional CT record only the intensity of the x-ray beam and not its energy distribution. Hence information regarding the composition is discarded reducing it's ability to distinguish one material type from another. Also, energy integrating detectors used in traditional CT weighs low energy photons less, resulting in increased

noise and decreased contrast.

Clinical dual-energy CT (DECT) is typically performed using either dual-source Johnson *et al.* (2011), kVp switching Wu *et al.* (2009), or dual-layered detectors Grajo *et al.* (2016). In DECT, materials can be distinguished by using two different x-ray spectra or a combination detector with different energy ranges. In DECT, the tissue attenuation depends on the atomic number (Z) and the density, and energy of the incident photon (E). While Compton scattering mainly depends on electron density and is independent of photon energy, photoelectric effect depends on atomic number and photon energy (Z^3/E^3) Beutel *et al.* (2000). Compton scattering is the predominant interaction for soft tissue, whereas photoelectric effect determines material differentiation and is the predominant interaction involving bone and contrast agents Ahmed *et al.* (2004). Due to the signal overlapping between the high and low energy acquisition steps, neither the kVp switching nor the dual source method have produced optimal material differentiation. Dual energy CT identifies and classifies materials when there is large differences in their atomic numbers and can only differentiate two materials.

Spectral CT systems use photon counting detectors (PCD) to obtain different x-ray energy bins per image. Some examples of energy resolving PCD used in x-ray imaging are XPAD, Medipix and Pilatus Delpierre (2014); Bech *et al.* (2008). When an x-ray photon hits semiconductor detector, electron hole pairs proportional to the amount of energy deposited are generated due to photoelectric absorption or Compton scattering. The electron hole pairs (charge cloud) created is separated using an external bias voltage which induces an electric current on the electrodes of the readout layer. This pulse associated with the photon energy is compared with user defined thresholds and subsequently binned into respective counters. The pixel electronics process the electrical signal on an event-by-event basis. In energy-resolving PCDs each energy is acquired simultaneously. Arbitrary energy ranges are defined by the user to optimise the imaging parameters to discover the imaging problem. PCDs can improve signal-to-noise ratio by setting an energy threshold above the noise level which reduces electronic noise. Spectral photon counting CT uses multiple energies to study attenuation characteristics and uses narrow energy ranges which

result in differentiation and classification of more than two materials having similar attenuation values. Figure 1.1 shows simultaneous detection and quantification of multiple materials in a single scan using spectral CT. The benefit of simultaneous detection is the reduction of artefacts due to sample movement, dose reduction and time savings.

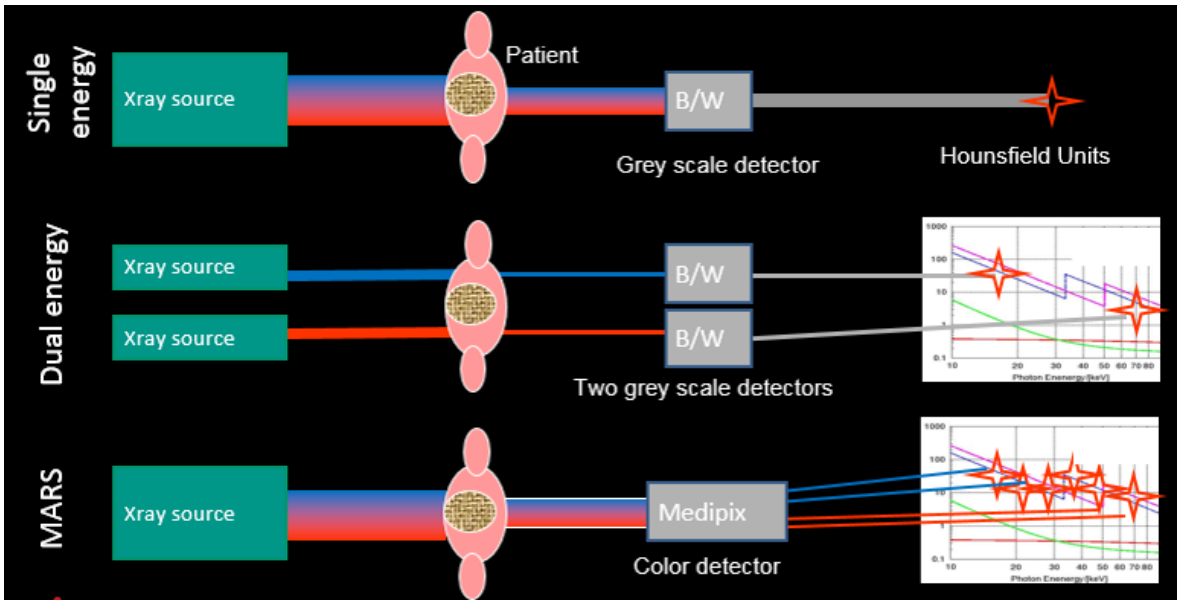

Figure 1.1: This figure gives a brief explanation of how spectral CT is different from conventional and dual energy CT. Spectral photon counting CT uses energy differentiating detectors. This enables detection and classification of different materials with similar attenuation values in a single scan.

The major factors which affect energy resolution of PCDs are pulse pile up, charge sharing effects, charge trapping and polarisation Guerra *et al.* (2009); Taguchi and Iwanczyk (2013). Pulse pile up is a form of sensor saturation in which two low energy electron hole pairs will be simultaneously recorded in the detector as a single high energy x-ray Taguchi *et al.* (2011). This will distort the spectral resolution and limit the count rate at which the detector can be operated. Ideally, when photon energy is absorbed by a sensor, the charge cloud generated should be contained within a pixel. Charge sharing occurs when the charge cloud from a single photon is split across adjacent pixels and are counted as separate low energy photons Zeller *et al.* (2009). Charge sharing not only degrades the spatial information, but also distorts the spectral information in the original pixel as well as in the adjacent pixels.

1.3 MARS spectral photon counting CT

The MARS spectral photon counting CT scanner is the first commercially available photon counting CT scanner which produces in vivo images by quantifying elements and compounds of the sample in a single scan. The MARS CT system comprises the scanning unit, controller software (graphical user interface), and the workstation. The major components of the scanning unit is a gantry which contains micro-focus x-ray tube (Source-Ray Inc, NY), a sample holder and a MARS camera. The MARS gantry contains two mounting points and rotates on a single axis. One of the mounting points is for the x-ray source and allows for the radial translation of the x-ray and controls source to object distance. The micro-focus x-ray tube has a tungsten anode with focal spot size of 50 μm which can be operated with a maximum tube potential of 120 kVp and tube current of 350 μA. The low power x-ray tube with small focal spot and short focal distance is favourable for obtaining images with high resolution and magnification Bugaev *et al.* (2013). The second mounting point on the gantry is for the MARS camera comprised of a hybrid pixelated detector (Medipix3RX) developed at European Organization for Nuclear Research (CERN), for applications in medical imaging. The mounting stage allows the MARS camera to be translated both radially and tangentially. These translations control the object to detector distance and enables to cover the scanning length of the specimen.

A hybrid pixel detector is a 2-dimensional matrix of microscopic sensitive elements, connected to its own readout electronics. The Medipix detector incorporates a direct conversion semiconducting sensor layer bump bonded to a Complementary Metal Oxide Semiconductor (CMOS) Application Specific Integrated Circuit (ASIC) readout layer. A schematic view of the hybrid pixel detector is shown in Figure 1.2 a. Depending on the application, different sensor materials (eg. Silicon (Si), Gallium Arsenide (GaAs), Cadmium Telluride (CdTe), Cadmium Zinc Telluride (CZT)) are chosen based on detection efficiency and operating x-ray range. The thickness, atomic number and density of the sensor determine the quantum detection efficiency Medjoubi *et al.* (2010). CdTe and CZT have close to 100 % detection efficiency upto

70 keV and 70% detection efficiency at 120 keV making it suitable for human imaging range (30 to 120 keV) Heismann *et al.* (2008). A bias voltage of -600 V is applied across the sensor layer to separate the electron hole pairs. The Medipix ASIC has a small pixel pitch (55-110 μm). Various versions of Medipix chips (Medipix2, Medipix3, Medipix3.1, Medipix3RX) have progressively evolved to improve on the lapses of the previous versions.

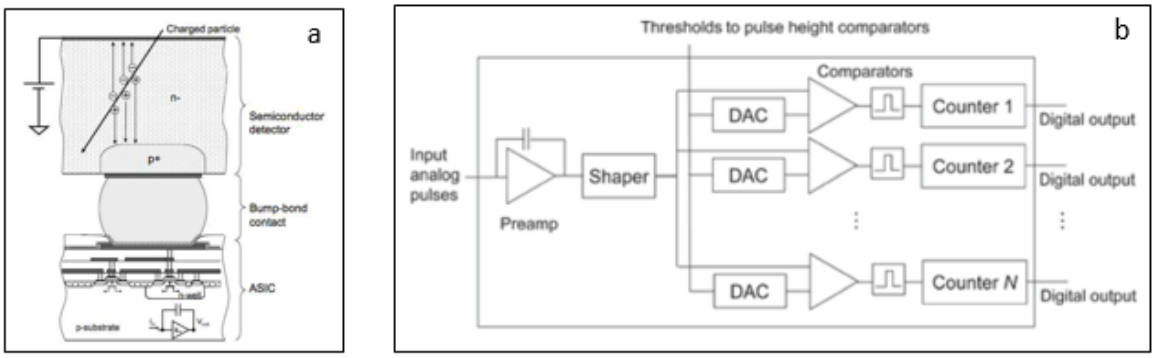

Figure 1.2: (a) A schematic view of a Medipix hybrid pixel detector with sensor layer bump bonded to the ASIC. When a photon strikes the semiconductor detector, an electron hole pair is created due to the ionisation of the sensor material. The bias voltage drives the electron hole pair towards the ASIC through the bump-bond contact (Image courtesy of Ballabriga (2009)). (b) The architecture of the ASIC readout circuit. Each pixel contains a charge sensitive preamplifier, a band-pass filter (shaper), two threshold discriminators (comparators) and counters which increments if the height of the preamplifier output pulse lies within the energy window defined by the two discriminators (Image courtesy of Taguchi and Iwanczyk (2013)).

The Medipix3 version can be bump bonded in either fine pitch or spectroscopic mode. In fine pitch mode, the Medipix3 has 256 x 256 pixels arranged in a square matrix with a pitch of 55 μm operated either in single pixel mode (SPM) or charge summing mode (CSM). Each pixel cell of the Medipix3 ASIC contains an analogue section to integrate and shape the incoming charge followed by a digital circuitry to count the individual pulses Ballabriga *et al.* (2018). Figure 1.2 b displays the architecture of a channel with N energy thresholds in the ASIC. In the analogue section of each pixel, it is possible to set an energy threshold which is transferred to a reference voltage using a digital to analogue converter (DAC). This DAC determines

the minimum level for an input pulse to be counted and select charge clouds based on the photon energy that created them. The discriminator in the analogue section compares the pulse height of a collected charge after amplification with the reference current set by the energy threshold DAC. The counter in the digital part of the pixel is incremented, if the pulse height of the collected charge is higher than the reference current. Two pulse height discriminators per pixel are provided in the fine pitch mode. In spectroscopic mode, the bump bonding is done at a pitch of 110 μm. The spectroscopic mode combines 2 x 2 clusters of pixels to create a super pixel with 8 energy discriminators. This increases the pitch to 110 μm in a 128 x 128 cluster array with 8 counters per pixel. The energy threshold DACs can be modified by the user to select the photon energies to be counted. The ability to adjust energy threshold DAC permits a hybrid pixel detector to be used as an energy resolving or spectral detector. The Medipix3RX, the latest modification in the Medipix family, is designed for spectroscopic imaging using 110 μm pitch. The pixels of the Medipix3RX ASIC can be operated either in single pixel or charge summing mode. In SPM, each pixel (110 μm) works independently of its neighbour resulting in charge sharing effect. Each pixel in Medipix3RX ASIC was designed to overcome the charge sharing effect by implementing charge summing mode which uses analogue summing circuits and coincidence detection using charge summing algorithms. When operated in CSM, the Medipix3RX arbitration circuit is used to identify a single event spread across multiple pixels using interpixel communication. The charge summing algorithm works over an area of 2 x 2 pixels (220 x 220 μm^2). The arbitration circuit distributes the reconstructed charge to the pixel closest to the original site of interaction (Figure 1.3 b). The measurements recorded in this thesis were acquired using a 2 mm CZT sensor attached to Medipix 3RX detector.

The MARS controller software allows the operator to select imaging parameters such as energy thresholds, tube current, exposure time, scanning length of the specimen and then temporarily stores the scanning data in the MARS workstation prior to processing. Images stored in the MARS console are transferred to the MARS workstation for image pre-processing, image reconstruction and 3D visualisation. MARS technology will advance to human imaging in the near future, as illustrated in

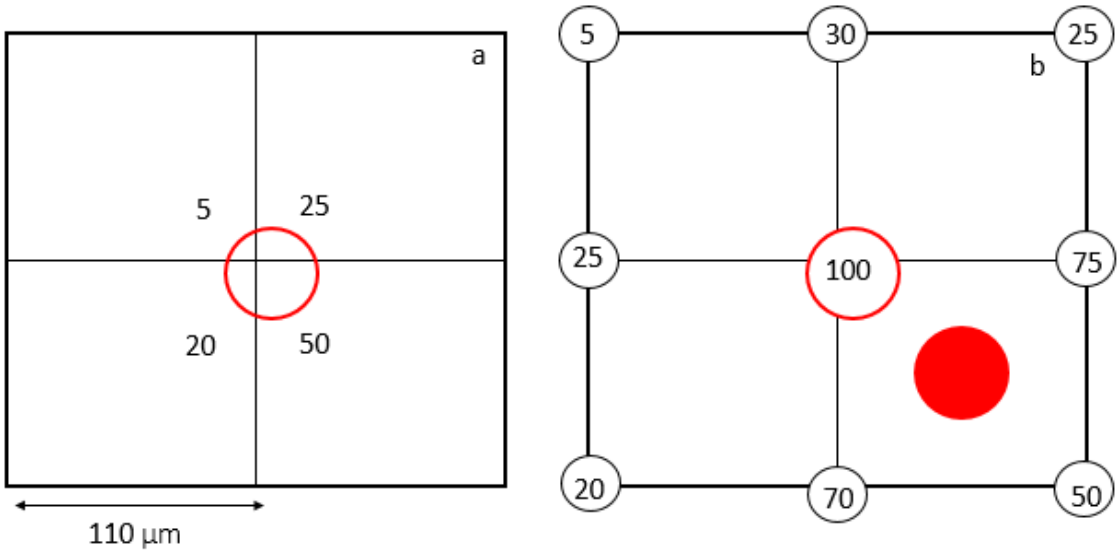

Figure 1.3: (a) Illustration of charge summing mode in Medipix3RX spectroscopic configuration. A charge of 100 keV deposited over a 220 x 220 μm^2 area is split over four pixels. (b) The charge is summed in the corners of nine adjacent pixels and assigned to the pixel (red) that initially received highest charge share.

Figure 1.4.

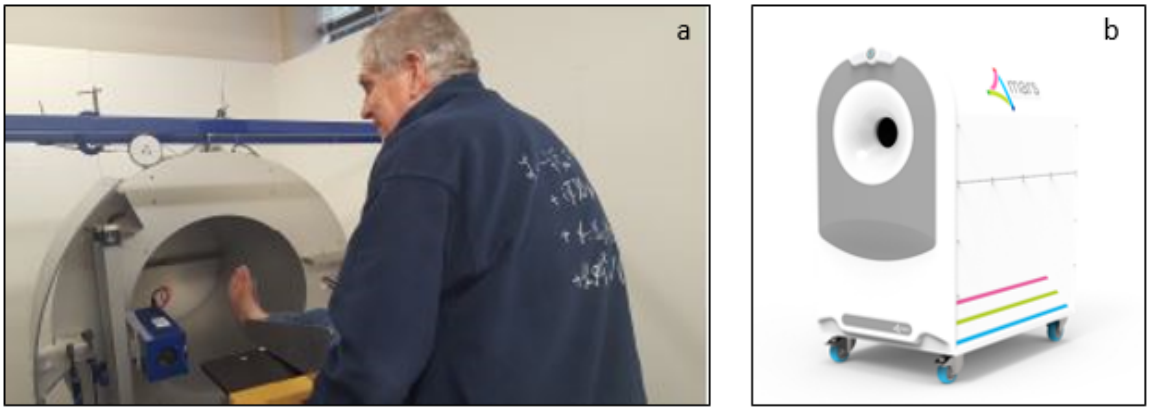

Figure 1.4: (a) A volunteer having his lower leg scanned with the large bore MARS spectral photon counting CT scanner (b) Prototype of the arm scanner under production. Images reproduced with the permission of MARS Bioimaging Ltd.

1.3.1 MARS Imaging

The MARS imaging chain begins with the acquisition of data from a calibrated scanner with suitable protocols optimised for various imaging purposes. Prior to scanning the sample, the faulty pixels are masked and a map is generated by acquiring 20 dark field and 400 flat field images. The dark field images are used in pixel masking to identify noisy pixels. The pixel mask is saved for masking or interpolation on dead and noisy pixels in the scan data sets. After pixel masking the projection images are collected at a number of angles by rotating the gantry around the sample. The projection images represents a set of overlapping broad energy bins (photon counts from the 8 counters). The spectral data is reconstructed using a customised polychromatic iterative reconstruction technique (De Ruiter *et al.* (2017)). The MARS iterative reconstruction technique takes projection images and converts it to a set of energy volumes. The CT reconstruction is performed in narrow energy bins to reconstruct the non-overlapping photon counts between the two subsequent counters. For instance, a set of adjacent, non-overlapping attenuation volumes (7-45 keV, 45-55 keV, 55-65 keV, 65-75 keV, 75-120 keV) can be reconstructed from the raw overlapping counters (7-120 keV, 45-120 keV, 55-120 keV, 65-120 keV, 75-120 keV) of the detector. Medipix3RX detector has eight energy bins which include one arbitration counter, four counters in charge summing mode and three in single pixel mode. In this study only those counters which contain charge summing circuitry were reconstructed. Lack of charge summing circuitry results in those counters using single pixel mode to have a complex energy response Rajendran (2016); Panta *et al.* (2014).

In spectral CT, different materials are represented with attenuation values depending on their density, atomic number and energy of photons. The conversion of energy information into material information is known as material decomposition (MD). MD can be performed in three different ways, namely, pre-reconstruction (projection based), post reconstruction (image based) and simultaneous or joint reconstruction. In pre-reconstruction MD, the projection data is pre-processed to extract energy independent information before the reconstruction Alvarez and Macovski (1976); Schlomka *et al.* (2008). In post-reconstuction MD, the energy independent information

is extracted from a reconstructed image in each energy range Heismann *et al.* (2003). In joint reconstruction, the material basis coefficients are directly reconstructed with CT image reconstruction Schioppa (2014). Pre-reconstruction as well as joint reconstruction allow for the modelling of the polychromacity of the x-ray beam (reduces beam hardening artefacts). This requires use of non-linear optimisation techniques which can be computationally intensive. Post-reconstruction MD can be performed quickly. The beam hardening artefacts in the reconstructed data are minimised by applying beam hardening correction techniques, using synchrotron x-ray sources or reconstructing data using narrow energy bins.

In MARS spectral CT, MD is performed in the image domain. The MD algorithm converts the attenuation volumes to material volumes using the linear least square method Bateman *et al.* (2018); Ronaldson *et al.* (2012); Liu *et al.* (2009). MARS-MD first measures the spectral response of the phantom containing known materials. Each voxel of the image provides an estimation of the attenuation in that voxel for the energy bin. The mass attenuation (μ/ρ) values for each material obtained from the phantom experiment is used to estimate material densities of unknown materials using linear least square algorithm. For each voxel, the MARS-MD algorithms decompose the linear attenuation into a set of mass attenuation bases for different materials. The MD algorithm produces an estimated densities (mg/ml) of the given basis materials.

MARS vision is the software for visualising and analysing the data acquired by the MARS scanner and processed by the MARS software tool chain Mandalika *et al.* (2018). MARS vision supports both energy and material data types, and allows the user to display this data using 2D and 3D visualisation techniques.

1.3.2 Applications

1.3.2.1 Material identification and quantification

Identification and quantification of different materials such as fat, soft tissue and bone is vital in clinical imaging. Spectral CT uses measurements of photon energy for simultaneous identification and quantification of different materials. MARS Vision enables users to assign different colours to different material channels as displayed in

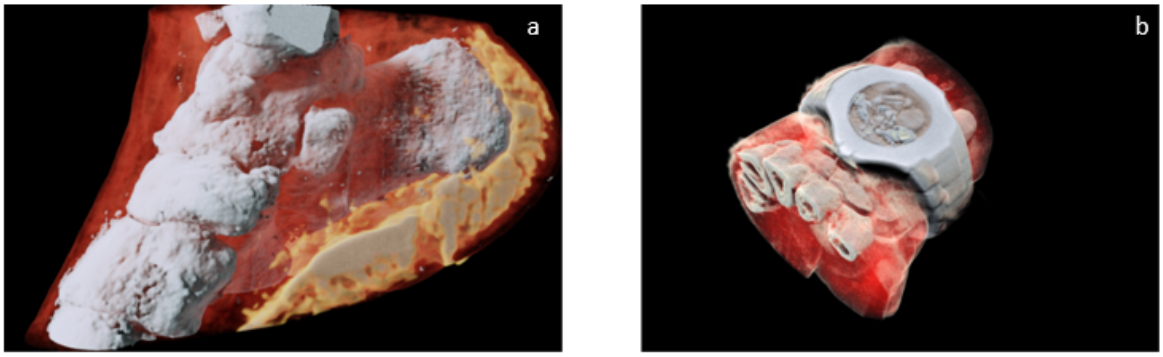

Figure 1.5: 3D volume rendering of first human images (a) ankle (b) wrist. Bone-like material displayed as white, water-like as red and fat-like as yellow. Images reproduced with the permission of MARS Bioimaging Ltd.

Figure 1.5.

1.3.2.2 K-edge imaging

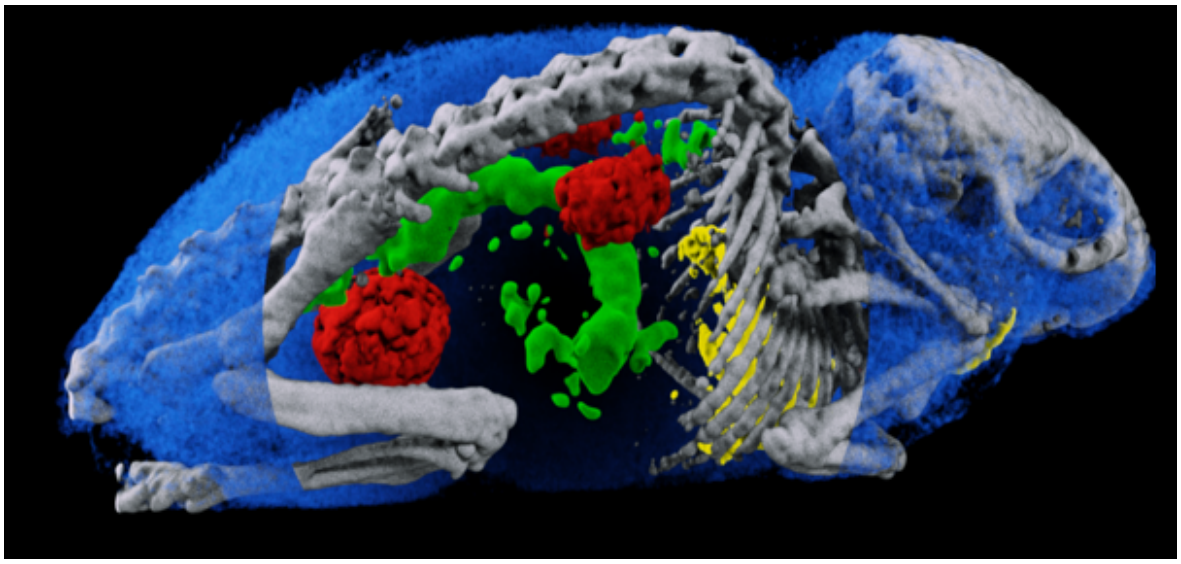

Figure 1.6: MD image of mouse model with multiple contrast agents. Gold nanoparticles are located in the lungs, iodine in the bladder and kidneys, and gadolinium in the stomach and intestines. Soft tissues are represented in blue and bones in white. Image reproduced with the permission of MARS Bioimaging Ltd.

Contrast pharmaceuticals are used in medical imaging to highlight anatomical regions which are not clear with different imaging modalities. Contrast pharmaceuticals contain highly attenuating materials (eg: Gadolinium, Iodine, gold

nanoparticles) when compared to targeted soft tissue. Contrast pharmaceuticals have a characteristic jump in their attenuation (k-edge) within the diagnostic x-ray range (30-120 keV). Some applications of contrast agents are cartilage imaging (Rajendran *et al.* (2017)), angiography (Lusic and Grinstaff (2012)) and to locate cancer (Popovtzer *et al.* (2008)). In spectral CT, energy thresholds can be set on either sides of the k-edge of multiple contrast agents at a time. This improves the ability to locate and quantify anatomical regions in a single scan as shown in Figure 1.6. The multiple energy binning feature of the spectral CT scanner can be exploited to optimise the use of contrast agents and for quantitative imaging in comparison with current CT technology.

1.3.2.3 Soft tissue imaging

In conventional CT, the contribution of low energy photons is underestimated by the energy integrating detectors. The x-ray attenuation difference between different soft tissues is maximum at the low energy range (< 40 keV). In spectral photon counting CT, the user can select an energy threshold above the electronic noise and acquire information from low energy photons to enhance soft tissue contrast. Selecting the photon energy threshold above the electronic noise will further improve soft tissue contrast and signal-to-noise ratio. Soft tissue imaging such as atherosclerosis, is characterised by the deposition of calcified plaques on the inner artery wall. MARS spectral photon counting CT has the potential to identify tissue type and quantify disease activity in plaques Searle *et al.* (2018) by identifying biomarkers of the disease and using potential imaging targets such as haemorrhage or cytokines within the plaque as demonstrated in Figure 1.7. This allows surgeons and cardiologists to be informed of the plaque's vulnerability to rupture.

1.4 Thesis outline

This chapter introduces the aim and significance of my research. It also provides a brief explanation of the working of MARS spectral photon counting CT and how it is different from other conventional CT imaging modalities.

Chapter 2 investigates the effect of external parameters such as temperature, field of

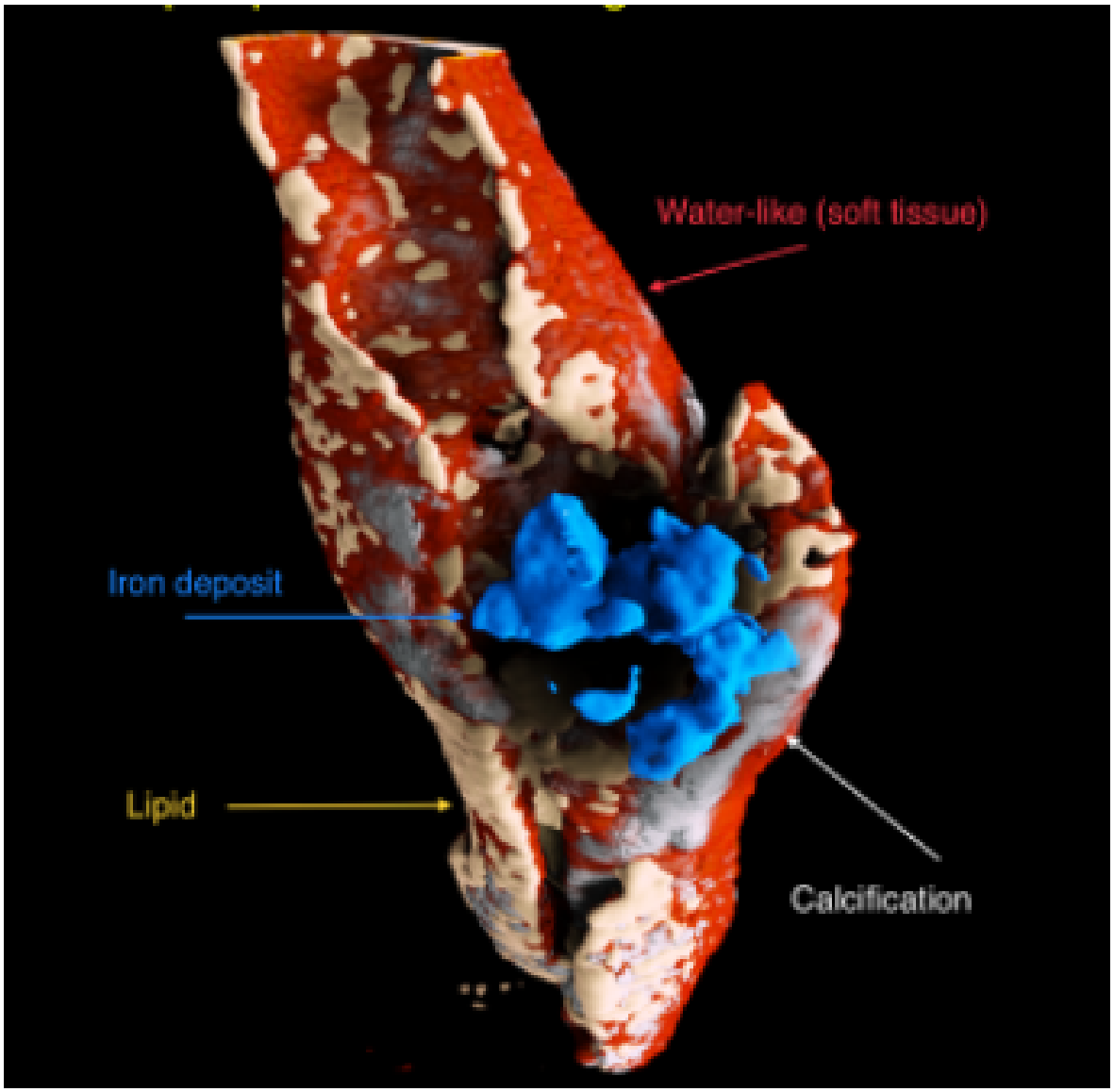

Figure 1.7: Plaque specimen displaying intraplaque haemorrhage through iron deposit. The iron-like material is blue, calcifications are white, lipid-like material is yellow and water-like material is red. Image reproduced with the permission of MARS Bioimaging Ltd.

view and decalcification on bone density and morphology.

Chapter 3 describes the process of optimisation of a protocol for imaging bone samples with implants.

Chapter 4 discusses the assessment of metal induced artefacts on tissue density using spectral photon counting CT.

Chapter 5 demonstrates the potential of MARS spectral CT in quantifying bone growth at the bone-metal interface and compares with the existing imaging modalities.

Chapter 6 confirms the potential of using spectral photon counting CT in differentiating calcium crystals in crystal-induced arthritis.

Chapter 7 concludes the thesis with discussion.

Chapter 2

Assessment of the effect of image acquisition related parameters on bone strength

This chapter describes the sensitivity of MARS spectral photon counting CT (SPCCT) scanner in determining changes in bone density and morphology. Bone mineral density (BMD) studies are used to diagnose osteoporosis and monitor its response to treatment Bonnick and Shulman (2006); Lufkin *et al.* (1992). In this study we used the same physics principles as Dual energy x-ray absorptiometry (DXA) but demonstrated the utility of a new type of spectral (multi-energy) photon counting CT scanner to simultaneously quantify bone microstructure and density. Sheep samples were used in this study for studying changes in BMD as they have a similar remodelling process to that of humans Lill *et al.* (2000); Goldhahn *et al.* (2005). Using energy resolving x-ray detectors, the spectral photon counting CT scanner quantifies bone density (g/cm^3) in a 3D image with a spatial resolution of approximately 90 μm. With this resolution it is possible to measure cortical thickness, trabecular thickness, and trabecular spacing Link *et al.* (1998); Hsu *et al.* (2014). We hypothesised that the ability of the MARS spectral CT scanner to simultaneously measure localised bone density and bone microstructure will provide researchers and clinicians with more information than DXA and traditional CT. The research discussed in this chapter has

led to the following publications Panta *et al.* (2018); Matanaghi *et al.* (2019).

2.1 Introduction

Bone mineral density is defined as the amount of bone mineral present in bone tissue. Bone mineral density is tested to assist in the diagnosis of osteoporosis, determine fracture risk in future and assess the effect of osteoporosis treatment Srinivasan *et al.* (2012); Felsenberg and Boonen (2005). Previously BMD was considered to be the determinant of bone strength. Studies have shown that in addition to BMD, changes in structural parameters such as trabecular thickness and spacing also contribute significantly to determine bone health Carter and Beaupré (2007); Oei *et al.* (2016); Adams (2013). DXA is the clinical tool currently used for identifying osteoporosis and fracture risk. DXA measures areal BMD (g/cm^2) and cannot simultaneously measure cortical and trabecular bone mineral density Perilli *et al.* (2012); Briggs *et al.* (2010). Also DXA cannot measure slight variations in trabecular bone density. DXA is population based and has limitations in monitoring treatment to osteoporosis El Maghraoui and Roux (2008); Bouxsein and Seeman (2009). FRAX is a clinical assessment of fracture risk that uses information of bone density from DXA and other fracture risk factors (age, gender, fracture history) for breaking bone to estimate the 10-year fracture risk at high risk bone sites Kanis *et al.* (2010). Due to low spatial resolution (350 - 1250 μm), quantifying bone microarchitectural changes using clinical single or dual energy CT is a challenge. High resolution peripheral quantitative CT (HR-pQCT), currently a research tool, has the potential to measure bone microarchitecture and volumetric bone mineral density in vivo Cheung *et al.* (2013); Zhou *et al.* (2016). HR-pQCT can be used to assess fracture risk in peripheral sites such as the distal radius and tibia. Common osteoporotic fracture sites such as the lumbar spine and proximal femur cannot be assessed using HR-pQCT due to its limited gantry size Link (2012).

Previous studies have demonstrated that MARS spectral CT can measure volumetric bone mineral density and bone morphology simultaneously. Four femoral neck specimens from Caucasian premenopausal and postmenopausal women of different

ages (from 42 to 87) were scanned with DXA, HR-pQCT and MARS spectral CT. The results of density measurement from spectral CT were compared with DXA and morphological measurements were compared to the results obtained from HR-pQCT Mohsen (2017), and were found to be consistent. The literature reports that BMD measurements are affected by many factors such as sample storage Wähnert *et al.* (2009); Trudel *et al.* (2005) and decalcification Castania *et al.* (2015); Lin *et al.* (2003). In this chapter we aimed to study the potential of the spectral CT scanner to measure the effect of field of view, temperature, and decalcification on bone strength assessment. Another objective of this study was to develop a semi-automated tool which could be integrated into MARS visualisation software for determining bone health. We hypothesised that MARS spectral CT will be able to detect variation in density and structural parameters due to changes in external factors.

2.2 Materials and methods

Image acquisition was performed using a preclinical MARS spectral CT scanner equipped with a 2 mm Cadmium Zinc Telluride (CZT) sensor bump bonded to Medipix3RX detectors in charge summing mode (CSM). Since CSM provides improved energy response and better material discrimination, energy bins in CSM were used in this study Panta *et al.* (2014); Ballabriga *et al.* (2013). The scanner was operated at 120 kVp at tube current of 26 μA, 220 ms exposure time and 0.375 mm brass filter. We used four CSM counters across the energy ranges 30-45, 45-60, 60-78, 78-118 keV. Image acquisition was performed using 720 projections over a 360°circular trajectory.

A customised calibration phantom which included bone equivalent (calcium hydroxyapatite) and soft tissue (water) and fat (lipid) equivalent materials was scanned with a previously optimised protocol for scanning bone specimens Mohsen (2017). To study the effect of field of view on BMD measurements, a sheep tibia was scanned with and without calibration phantom with a field of view of 32 mm. In the first study, the calibration vials were scanned prior to the biological specimen. In the second study, the calibration phantom was scanned simultaneously with the biological

specimen. The difference between the BMD measurements of two datasets of sample size (n=66 slices) were quantified using Bland Altman analysis Giavarina (2015) using a scatter plot in which x-axis represented the average and y-axis represented the difference of the BMD measurements in the two scans.

Freezing is considered to be a standard preservation technique for storing biological specimens. We hypothesised that ice crystals from freezing of bone could impair x-ray absorption and affect BMD measurements. To quantify the effect of bone temperature on BMD, density and morphological measurements of the same sheep femur were compared in frozen (stored at -20°C) and thawed (after thawing for 24 hours) states. However, while scanning the frozen sample the scanner was operated at room temperature.

Images were reconstructed for each energy bin using a proprietary MARS iterative reconstruction algorithm. PCDs have the ability to differentiate incoming photons based on their energies, obtaining spectral information in a single scan. The greater the capability of spectral separation, the greater the reliability of material decomposition. The basis for material decomposition (MD) was generated from the linear attenuation coefficients and concentrations of calibration rods. To measure bone density and morphology, material decomposition (MD) was applied to the biological specimens to distinguish water-like, lipid-like and calcium-like materials. MD images of the calcium-like channel were used to measure bone mineral density.

Image segmentation is the process of separating the image into different parts. For accurate quantification of architectural parameters the critical step is the segmentation of cortical and trabecular bone compartments. Trainable Weka segmentation is a Fiji plugin Doube *et al.* (2010) that uses machine learning algorithms and a set of selected image features to produce pixel-based segmentation. For training the classifier, Hessian feature with fast random forest algorithm was utilised Huynh *et al.* (2015). Segmented images were used to separate the calcium-like channel to cortical and trabecular bone. Otsu thresholding was applied to binarise images Fripp *et al.* (2007); Tassani *et al.* (2014). Binary images were used to measure morphological parameters such as thickness and spacing Gordon *et al.* (1998); Lespessailles *et al.* (2006).

For studying decalcification, a sheep femur was dissolved in 50 mL of 10 mM nitric

acid Liu *et al.* (2017). We scanned the biological sample at various times (0, 3, 6 and 10 days) and at each stage we sampled and replaced the acid solution. The total and cortical BMD was quantified after 0, 3, 6 and 10 days of sheep bone in nitric acid solution. For determining the calcium content in the nitric acid solution, the solutions were analysed using atomic absorption spectroscopy (AAS). The BMD (calcium content) obtained from spectral CT was compared with calcium content quantified from AAS.

2.3 Results and discussion

2.3.1 Effect of field of view (FOV) on BMD

In quantitative computed tomography (QCT), an external reference phantom of known concentrations is used for BMD measurements to reduce inter-scan variations. The reliability of the spectral CT scanner in measuring the known concentration of the calibration phantom was quantified as mean ± standard error as shown in Figure 2.1. The results demonstrates that there was a decrease in the density of the concentrations

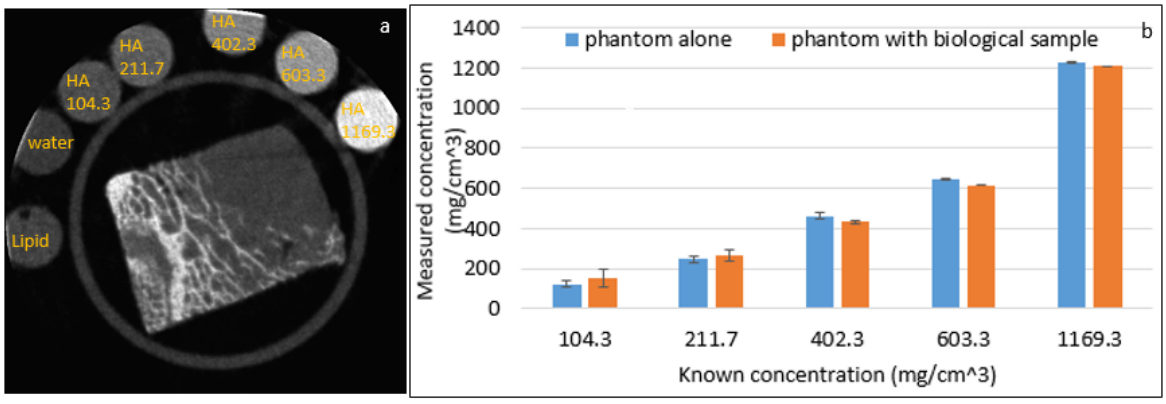

Figure 2.1: (a) A sheep tibia scanned with calibration vials outside the field of view. (b) The graph displays underestimation of higher concentrations of calibration vials located outside the field of view.

of bone equivalent materials (HA 402.3, HA 603.3 and HA 1169.3 mg/cm^3) outside the field of view. This could be due to the discontinuity of the projection data caused by the superimposition of the nonhomogeneous and asymmetrical tissue equivalent

materials outside the field of view. Also the beam hardening and partial volume effect can affect the density measurements if the FOV of the imaging phantom is less than the phantom size.

The basis values quantified from two scans were applied to decompose the sheep

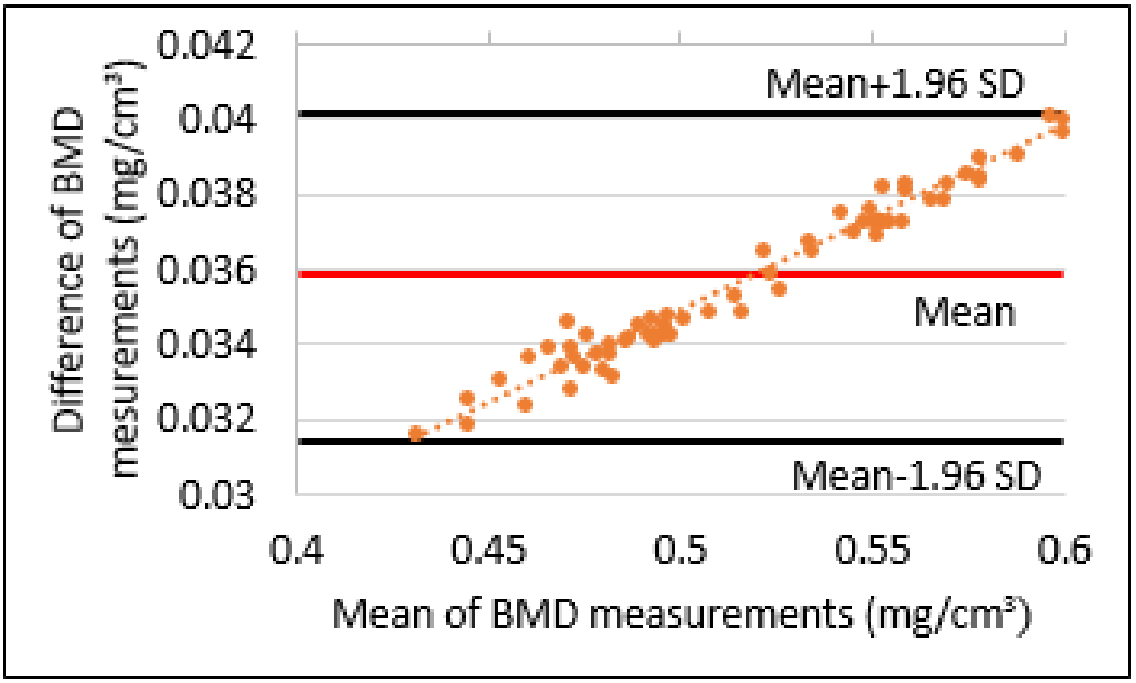

Figure 2.2: Scatter plot illustrates correlation between the BMD measured from two datasets measured using Bland Altman analysis. Horizontal lines are drawn at the mean difference and at the limits of agreement (mean $\pm$ 1.96 $\times$ SD).

tibia to calcium-like material. The BMD measurements obtained from the two scans for the same sample scanned with similar acquisition parameters were compared using Bland Altmann method. The fundamental rationale for Bland Altman analysis is the recognition that good correlation across a widespread sample does not imply good agreement at all ranges. The mean difference of BMD measured from two datasets was 0.036 with a SD of 0.002. The upper limit of agreement (LOA) was 0.040 and lower limit was 0.031. In the scatter plot (Figure 2.2), the points lie relatively close to the line which represented mean bias.

The magnitude of the difference of BMD measurement displayed a linear trend which could be due to the calibration error in one of the measurements. The Bland

Altman plot displays that the BMD quantified from the sheep tibia scanned with the calibration phantom outside the field of view is slightly lower than the BMD estimated from the same biological sample with calibration phantom scanned within the field of view. Hence imaging phantoms and samples with field of view greater than the phantom size is essential for the accurate assessment of the density measurement.

2.3.2 Effect of temperature on BMD and morphology

The sample size (n=71 slices) was used from frozen and thawed samples to measure bone density and morphology. Using an inbuilt MARS-MD algorithm, the spectral data was decomposed to combinations of hydroxyapatite, lipid and water as shown in Figure 2.3. The gradient in density of the trabecular region is represented from orange to yellow and the cortical region as green.

The classified image and the corresponding probability maps for cortical and trabecular region are displayed in Figure 2.4 .

Results demonstrate that there was an increase in total BMD and cortical BMD for the frozen sample, whereas no change was observed in the trabecular BMD (Figure 2.5). Bone morphological parameters, such as cortical and trabecular thickness, increased for thawed specimens. Our results demonstrate that MARS spectral CT was able to quantify slight changes in bone density and morphology in the frozen and thawed samples.

2.3.3 Effect of decalcification on BMD

Table 2.1 shows the quantification of total and cortical BMD obtained from spectral CT (n=71 slices) in comparison with the AAS results. A decreasing trend in the cortical and total BMD indicates loss in bone mineral density with decalcification. The calcium content measured from nitric acid solutions analysed using AAS increased from the first day to the last day of the experiment.

Our results show that MARS spectral CT can measure slight variations in BMD which demonstrate its potential to identify changes in osteoporotic bone. While AAS quantified calcium content in the whole solution, bone mineral density was measured

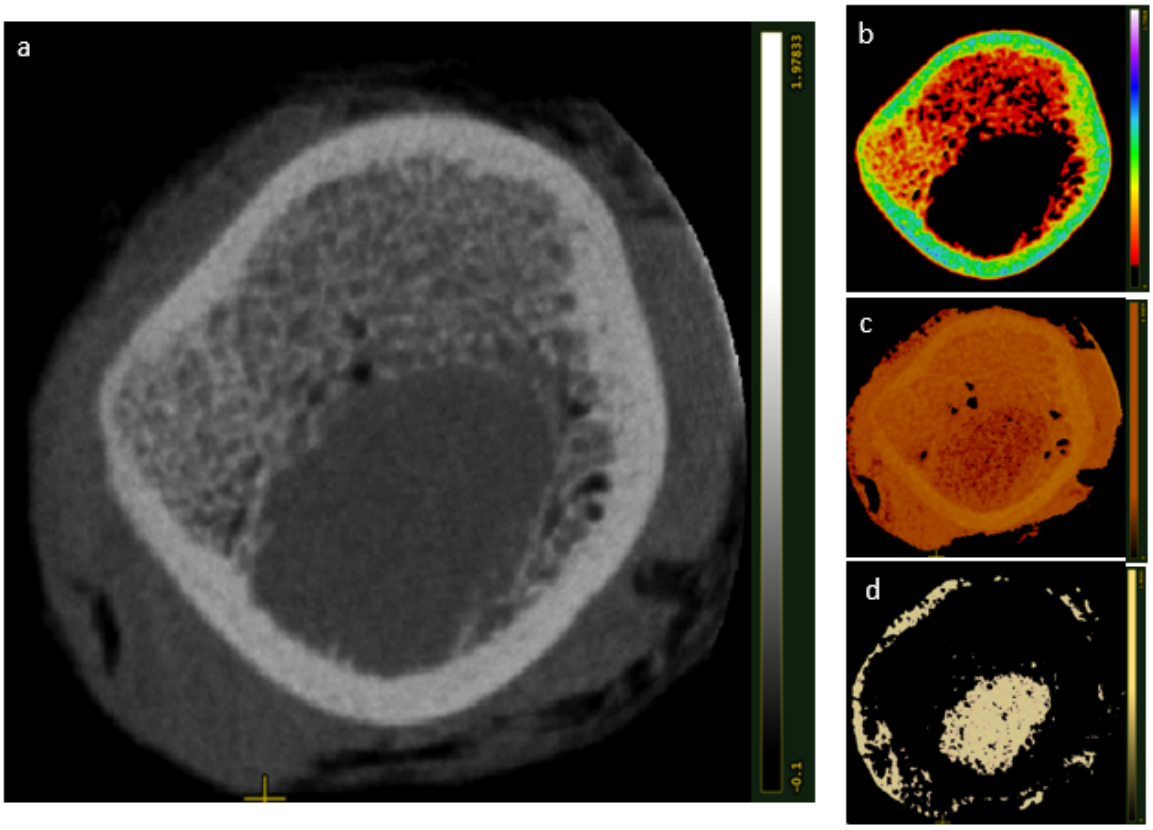

Figure 2.3: Images of frozen sheep femur (a) CT image. The scale represents linear attenuation in cm^{-1}. MD image of (b) HA-like material. Based on the density values the cortical and trabecular bone can be separated and represented with different colours. (c) water-like material (d) lipid-like material. The scales represents density of the material in g/cm^3.

Table 2.1: Comparison of calcium content quantified from spectral CT with AAS

Days in acid	Spectral CT		**AAS**
	Total BMD (mg/cm^3)	**Cortical BMD (mg/cm^3)**	**Calcium content (mg/ml)**
0	**0.72 ± 0.01**	**1.13 ± 0.01**	**0**
3	**0.72 ± 0.01**	**1.08 ± 0.01**	**0.09**
6	**0.70 ± 0.01**	**1.06 ± 0.01**	**0.19**
16	**0.69 ± 0.01**	**1.03 ± 0.01**	**0.32**

for a length of ≈ 6 mm of the femoral bone. This might be the reason for the decrease in calcium content quantified using spectral CT (0.03 mg/cm^3) when compared to the AAS results (0.3 mg/ml).

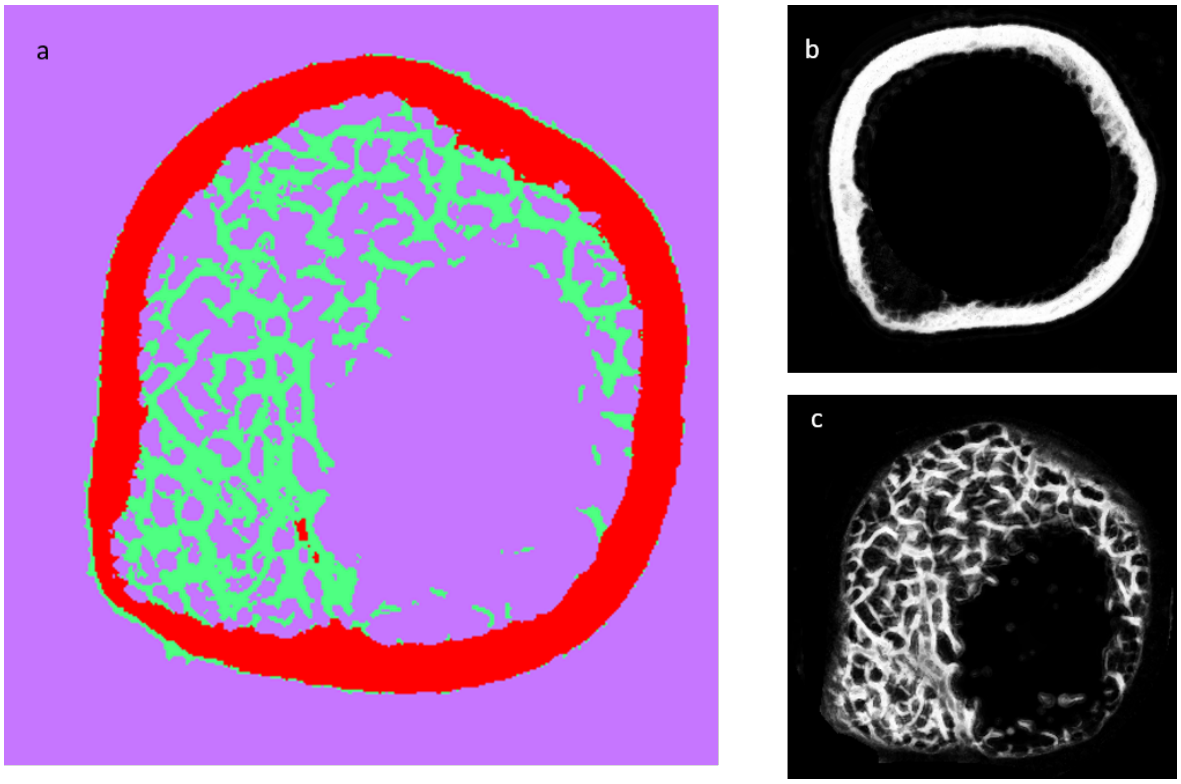

Figure 2.4: (a) Fast random forest algorithm was used to classify HA-like image to cortical and trabecular regions. Based on the classification of image, probability maps are generated for (b) cortical bone (c) trabecular bone.

2.4 Discussion

The aim of this study was to explore the potential of MARS spectral CT in measuring variations in BMD and morphology due to change in external factors. In this study the correlation between field of view of phantoms, specimen temperature and decalcification on BMD and bone architecture was studied. The results demonstrated that calibration phantom scans, sample preparation and decalcification affects BMD measurements. The improved energy resolution (3.5 keV) and spatial resolution of MARS spectral CT enabled measurement of changes in BMD and bone micro-architecture. The major limitation of this study was the number of samples scanned as proof of concept for establishing the capability of spectral CT in monitoring changes in BMD and architecture. Further studies with more biological samples were performed by a PhD student, showing a consistent trend.

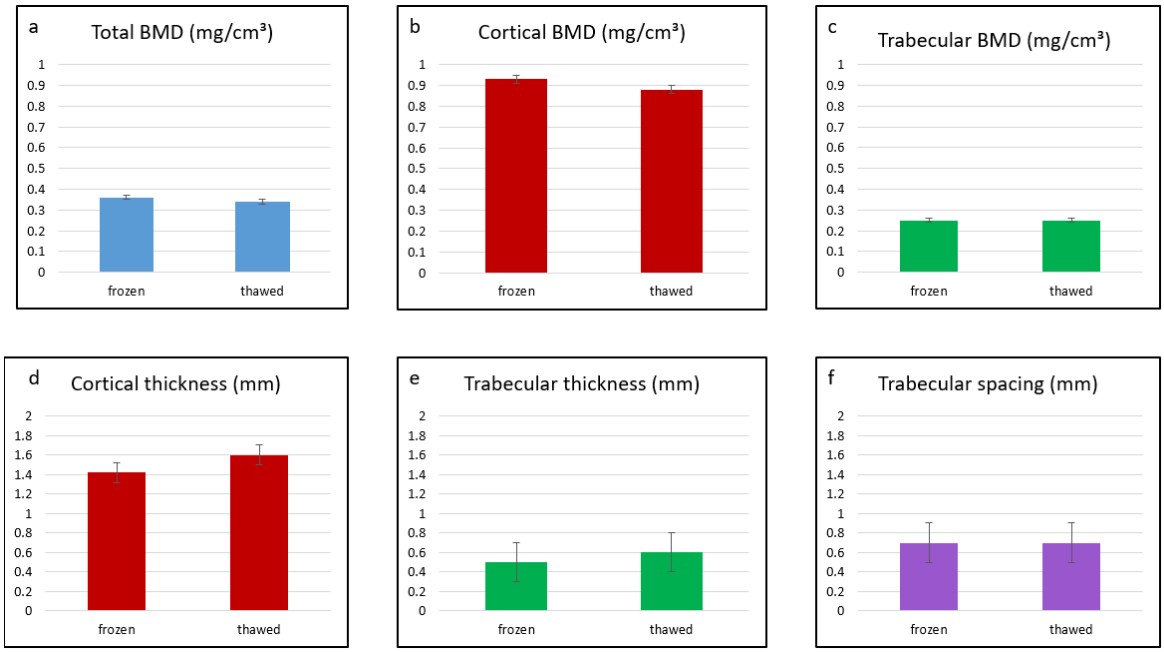

Figure 2.5: Quantification of bone density and morphology (a) Total BMD (b) Cortical BMD (c) Trabecular BMD (d) Cortical thickness (e) Trabecular thickness (f) Trabecular spacing.

In previous studies, BMD and bone micro-architecture were measured using ImageJ and manual contouring methods. In this study a semi-automatic contouring method using active contours to quantify BMD and morphology was developed by Celeste Leary (PhD student, Oregon Health and Science University). This semi-automatic method was modified by Aysouda Matanaghi (PhD student, University of Otago, New Zealand) including a Trainable Weka segmentation and classifier model to improve the reliability and repeatability of bone measurements. This study also led to the discussion for the need to integrate a bone analysis tool with MARS Visualisation software.

Future studies can be done to scan cadaveric forearms obtained from PAVmed (USA), with MARS, DXA, clinical CT and HR-pQCT scanners to assess forearm fracture risk. Combining data quantified from DXA, dual energy CT and HR-pQCT, a scoring sheet incorporating factors which defines bone strength such as bone morphology, bone density and location can be devised. The advantage of this scoring sheet is that it will be based on the quality and quantity of bone, and therefore independent of age, gender etc.

2.5 Conclusion

MARS spectral CT is a potential tool to identify and monitor changes in bone mineral density and microarchitecture. The frozen samples should be completely thawed prior to scanning the specimens. The scan field of view should be greater than the size of the sample. A semi-automatic method for quantifying bone density and microarchitecture was developed.

2.6 Dissemination of this research

The methods and results from this chapter have led to the following journal articles and conference proceedings.

1. Matanaghi, Aysouda, Aamir Raja, Celeste Leary, **Maya Rajeswari Amma**, Raj Panta, Marzieh Anjomrouz, Mahdieh Moghiseh, Anthony Butler, Benjamin Bamford, and MARS Collaboration. Semi-automatic quantitative assessment of site-specific bone health using spectral photon counting CT. Journal of Nuclear Medicine 60, no. supplement 1 (2019): 1297-1297.
   This abstract explains the semi-automatic method developed for quantifying bone strength and compares it to the contouring method. This abstract received the **best international abstract** for the Society of Nuclear Medicine and Molecular Imaging (SNMMI) symposium, 2019.

2. Panta, Raj Kumar , Butler, Anthony , Butler, Philip , Ruiter, Niels , Bell, Stephen , Walsh, Michael , Doesburg, Robert , Chernoglazov, Alexander , Goulter, Brian , Carbonez, P. , Damet, Jérôme , Adebileje, Sikiru , Alexander, Steven , **Rajeswari Amma, Maya** , Anjomrouz, Marzieh , Asghariomabad, Fatemeh , Atharifard, Ali , Baer, Kenzie , Bamford, Benjamin , Woodfield, Tim. (2018). First human imaging with MARS photon-counting CT. 1-7. 10.1109/NSSMIC.2018.8824513.
   The proceedings demonstrate the translation of MARS preclinical scanner to

human imaging. I assisted with scanning a human ankle and performed the data analysis using inbuilt MARS MD.

This study was done in collaboration with Oregon University, USA. I collaborated with Celeste Leary, PhD student from Oregon University to perform the scans. I also contributed to data analysis and post processing of the images. I collaborated with scientists and researchers of the HIT Lab by providing insights into the development of a bone analysis tool. As a result of the collaboration, a bone analysis tool (refer Chapter 4 subsection 4.2.3) was integrated to MARS visualisation software for future users to quantify bone morphological parameters. This research also led to two oral and two poster presentations

1. **Amma, M. R**. Study of bone health using MARS spectral CT. Maya Rajeswari presented in the 3 Minute thesis competition held at the University of Otago, Christchurch, New Zealand, July 2017.

2. **Amma, M. R**, C Leary and the MARS collaboration. Bone strength assessment using MARS spectral CT. Maya Rajeswari presented at UOC Postgraduate Students Symposium (July 2018, Christchurch, New Zealand).

3. Matanaghi, Aysouda, Aamir Raja, Celeste Leary, **Maya Rajeswari Amma**, Raj Panta, Marzieh Anjomrouz, Mahdieh Moghiseh, Anthony Butler, Benjamin Bamford, and Mars Collaboration. Semi-automatic quantitative assessment of site-specific bone health using spectral photon counting CT. Celeste Leary presented the ePoster at the SNMMI Annual meeting held from in January 2019, California. Aysouda Matanaghi presented the poster at the Bioengineering showcase held at Dunedin, November 2019 and won the **second best poster** award.

2.7 Summary

• The potential of the MARS spectral CT scanner to measure the effect of field of view, temperature, and decalcification on bone morphology was assessed.

• MARS spectral CT can quantify variations in bone density and morphology.

• A semi-automatic method for the measurement of bone microarchitecture was developed.

• Improved spectral and spatial resolution of MARS spectral CT scanner might enable earlier detection of osteoporosis and monitor response to the treatment.

Chapter 3

Optimisation of protocol to image tissue-metal interface

MARS spectral photon counting CT (SPCCT) is an emerging imaging modality which could assess tissue-metal interfaces with reduced artefact. Before it can be implemented clinically for patient imaging, a protocol to scan samples with metal implants has to be optimised. The characteristics of image quality such as contrast, spatial resolution and noise can be adjusted by optimising image acquisition parameters for maximum clinical benefit Kalender *et al.* (2008). Optimising image quality requires understanding of the cause of artefacts and methods to suppress it Barrett and Keat (2004). Protocol optimisation begins with factors such as adjusting the x-ray spectrum by choosing appropriate filters, selecting suitable tube current and exposure time, optimising desirable energy ranges, modifying the field of view, determining the number of circular projections and deciding effective voxel sizes for reconstruction. In this chapter, the various acquisition parameters studied for protocol optimisation to scan tissue-metal interface are discussed. The methods mentioned in this chapter have already been published Amma *et al.* (2018); Butler *et al.* (2019).

3.1 Introduction

The major limitation of existing imaging modalities in analysing tissue-metal interface is the artefacts that obscure information and impair the detection of tissues in the vicinity of the implant. In clinical CT, physical effects such as beam hardening, photon starvation, and partial volume effects can severely limit the assessment of any tissue lying in the vicinity of the implant Rinkel *et al.* (2008); Yazdi and Mohammadi (2017).

Beam hardening occurs when a polychromatic x-ray beam passes through a dense material and increases the overall mean energy of the beam (due to the higher absorption of low energy photons). Most CT reconstruction algorithms do not take this into account resulting in two types of artefacts, namely cupping and streak artefacts. Solid metal implants highly attenuate the beam, which can lead to photon starvation that produces bright and dark streaks around the metal implant in the direction of greatest attenuation Boas and Fleischmann (2012). Partial volume effects occur when high contrasting materials, such as metals, lie in the same voxel thereby producing attenuation values proportional to the average of these materials, resulting in a blur Kuhnigk *et al.* (2006). Due to these artefacts, diagnosis of images of patients with metal implants is challenging.

The correction of these artefacts using hardware based approaches and algorithm methods has been an active area of research since the invention of CT Sun *et al.* (2004); Meyer *et al.* (2010, 2012); Bamberg *et al.* (2011). While conventional clinical CT systems use energy integrating detectors, dual energy CT reduces the beam hardening effect by scanning at two different energies and using image processing algorithms. Even though MRI provides better soft tissue information than CT, for patients with metal implants, difference in magnetic susceptibility between the implant and the soft tissue causes metal artefacts. Metal implants lead to low signal-to-noise ratio, geometric distortion, signal void and pile up, and failed fat suppression, which limit its diagnostic utility in evaluating bone-metal interface Hargreaves *et al.* (2011); Stradiotti *et al.* (2009).

Photon counting spectral CT counts the number of incoming photons and measures the photon energy. Spectral CT splits the x-ray spectrum into predefined energy bins facilitating the acquisition of CT data in different energy bins. Photon counting CT can reduce radiation dose, reconstruct images with higher resolution and minimise beam hardening Ballabriga *et al.* (2016); Shikhaliev (2005). The objective of this study was to optimise acquisition parameters to reduce the effect of metal artefacts at the tissue-metal interface.

3.2 Materials and methods

Phantom (mimicking tissue equivalent substances such as lipid, water and hydroxyapatite or calcium chloride) studies were carried out to optimise the acquisition parameters as shown in Figure 3.1. Scans were acquired using a MARS small bore spectral CT scanner. In each of the scans acquisition parameters were varied to determine the optimal scan protocol.

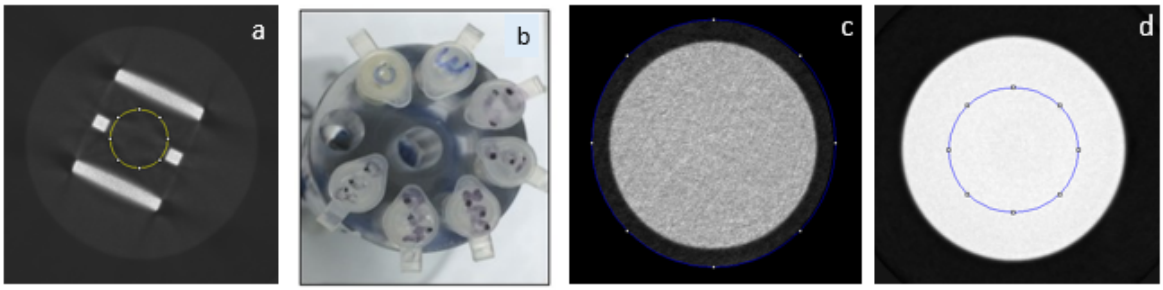

Figure 3.1: (a) Cylindrical phantom consisting of four 316L stainless steel implants to compare artefact added value at the centre of a PMMA phantom in the presence of brass and aluminium filters (b) Calibration phantom consisting of lipid, water and known concentrations of calcium chloride solution to determine material decomposition (MD) basis values (c) Polished polymethyl methacrylate (PMMA) phantom for calculating modulation transfer function (MTF) (d) PMMA phantom for determining the optimal number of circular projections.

3.2.1 Choosing appropriate filters

The artefact which mainly affects tissue-metal interface is beam hardening caused by the absorption of low energy photons. Correction of beam hardening can be done

during image acquisition by adding extrinsic x-ray filters Meganck *et al.* (2009). In order to eliminate low energy photons one of the method is to use external filters such as Cu, Al, Brass and lead. In this study, the x-ray spectrum produced by adding extrinsic filters (0.375mm brass filter, 2mm aluminium filter) to the intrinsic 1.8 mm aluminium equivalent filtration was simulated using SpekCalc Poludniowski *et al.* (2009). A 25 mm diameter cylindrical polymethyl methacrylate (PMMA) phantom with four 316L surgical steel implant and a PMMA phantom without surgical steel (for reference) was imaged with aluminium and brass filters (Figure 3.1 a) to quantify artefact added value (AAV) due to the implant. A region of interest with an area of $\approx$ 4300 voxels was drawn at the centre of the fifty slices in five energy bins (7-45 keV, 45-55 keV, 55-65 keV, 65-75 keV, 75-118 keV). This position was chosen because of its proximity to the stainless steel implant as it includes significant sampling of the metal streak artefacts. The artefact added value with extrinsic brass and aluminium filters was calculated as

$$AAV = ((MVV_{art} - MVV_{PMMA})/MVV_{PMMA});$$

where MVV_{art} and MVV_{PMMA} are the mean voxel values at the centre of the PMMA with and without metal implants.

3.2.2 Selecting suitable acquisition parameters

Spectral response is the efficiency of a CT system in differentiating tissue materials with respect to energy. It affects the sensitivity and specificity of material identification and characterisation. A phantom consisting of different known concentrations of calcium hydroxyapatite (HA) along with lipid and water was scanned at two different tube currents (26 μA and 40 μA) to assess the capability of MARS scanner in separating different materials (Figure 3.1 b).

3.2.3 Optimising desirable energy ranges

Spectral imaging simultaneously allows for the quantification and identification of multiple materials. Material decomposition uses the energy dependence of x-ray

attenuation of each voxel from different energy bins to estimate basis materials in the material volume. Each data channel measures density (mg/ml) of the material. Mass attenuation profiles of calcium chloride and calcium hydroxyapatite are similar, making them both suitable as calibration materials for bone. Previous studies demonstrated the reduction of metal artefacts in high energy bins. Hence, a calibration phantom containing lipid, water and five different concentrations of calcium chloride/ hydroxyapatite was scanned with two different energy protocols - P1 (45-55, 55-65, 65-75, 75-118 keV (only high energy bins)); P2 (7-45, 45-55, 55-65, 65-75, 75-118 keV (a combination of low and high energy bins)) to quantify material identification.

3.2.4 Deciding voxel size

The spatial resolution of the system was assessed using modulation transfer function (MTF). MTF defines how many physical line pairs per millimetre in an object can be fully reproduced by the imaging system. A polished polymethyl methacrylate (PMMA) phantom (Figure 3.1 c) was scanned at 110 μm and the images were reconstructed at 90 and 70 μm to quantify MTF Wang (2013). The mean voxel values from the region of interest were used to produce an edge response function (ERF). The point spread function (PSF) was derived from the ERF using numerical differentiation. The fast Fourier transform of the PSF yields the MTF for the CT system.

3.2.5 Determining the number of projections in a circular scan

The image quality of a CT system is affected by the number of circular projections. The larger the number of projections, the better the reconstruction quality. Fewer projections can reduce radiation dose and scanning time. In order to assess the variation of image quality with the number of circular projections, an MTF phantom (Figure 3.1 d) was scanned in air. The signal-to-noise ratio (SNR) was measured as the ratio of the mean to standard deviation for different numbers of projections for the selected ROI for fifty slices.

SNR = μ/σ;

where μ is the mean and σ is the standard deviation of the measured signal.

3.3 Results

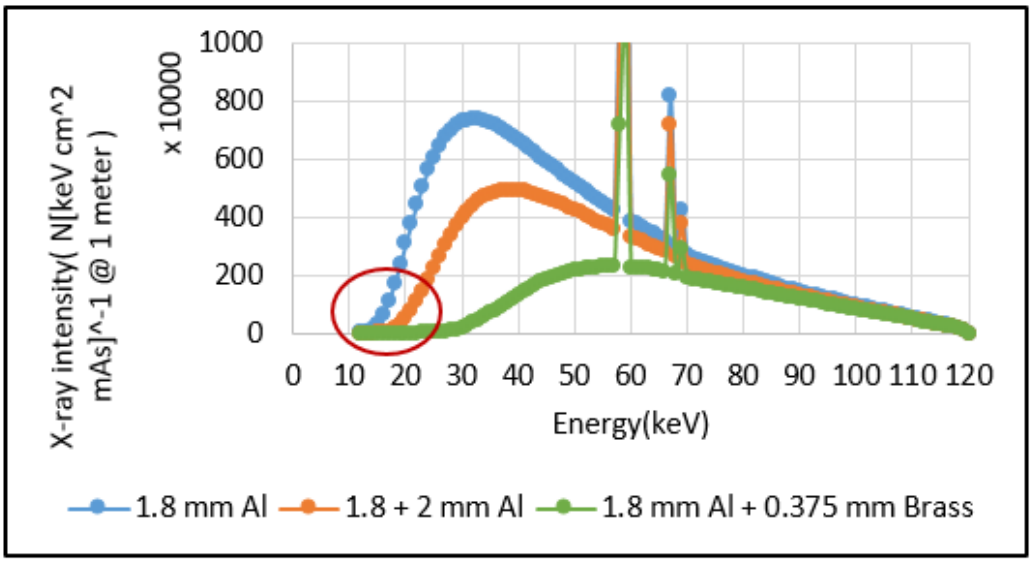

Figure 3.2: Simulated x-ray spectra produced using SpekCalc demonstrates the effect of external filters on low energy photons. A combination of 1.8 mm Al and 0.375 mm brass filter absorbs low energy photons of ≈ 25 keV when compared to other filters, reducing beam hardening.

Table 3.1: Optimised protocol for scanning tissue-metal interface

Tube voltage	**120 kVp**
Tube current	**26 μA**
Exposure time	**220 ms**
Energy bins	**7-45, 45-55, 55-65, 65-75, 75-118 keV**
Filtration	**1.8 mm Al + 0.375 mm brass**
Number of projections	**720**
Pixel size	**90 μm**

Simulated x-ray beam spectra produced using SpekCalc with intrinsic and added filtration is shown in Figure 3.2. The simulated x-ray spectrum displays that increasing filtration will reduce the quantity of the beam by absorbing most of the low energy photons which will be absorbed by tissues thus reducing radiation dose and beam hardening.

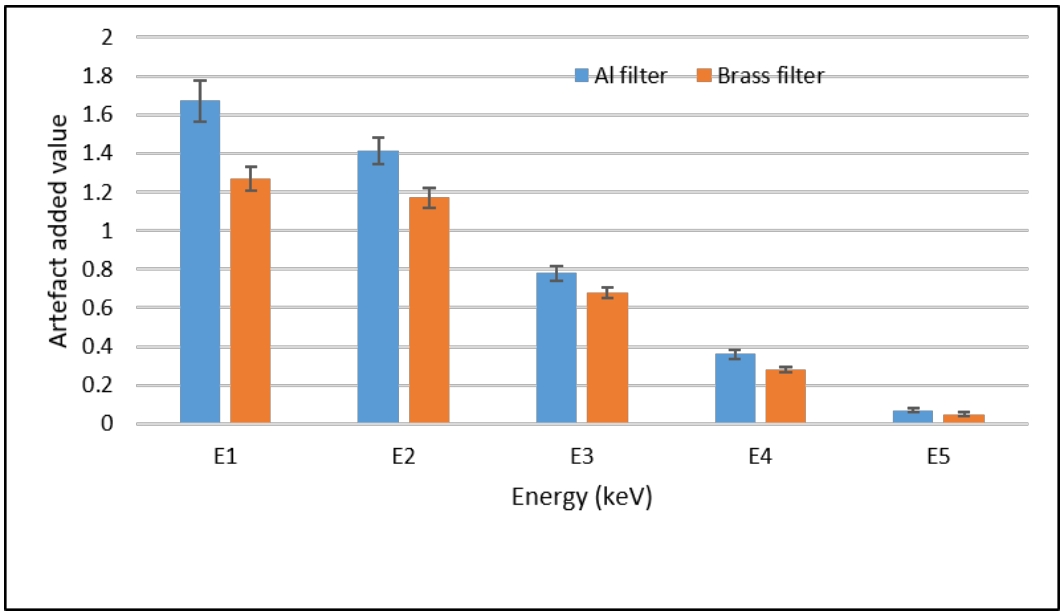

Figure 3.3: Artefact added value quantified from the centre of the ROI in the PMMA with aluminium and brass filtration reduced in higher energy bins (E1 (7-45 keV), E2 (45-55 keV), E3 (55-65 keV), E4 (65-75 keV), E5 (75-118 keV)). The artefacts were less pronounced with brass filter when compared to aluminium filter.

The artefact added value quantified from the phantom (Figure 3.1 a) with extrinsic aluminium and brass filter decreased with higher energy bins. The artefact added value quantified from the phantom with brass filter in low energy bins was much less compared to the aluminium filter as shown in Figure 3.3. This can be explained with reference to the simulated spectrum, as most of the low energy photons are absorbed by brass filter leading to less beam hardening.

Spectral response of different concentrations of HA at two different tube currents illustrated that at high tube current (40 μA), the attenuation values of lower concentrations of HA (54.3 and 104.3 mg/cm^3) are too close to differentiate (Figure 3.4) at higher energy bins. Hence tube current of 26 μA was chosen as the optimal current. Increasing the tube current can reduce photon starvation but could also increase the radiation dose and adversely affect material identification of lower concentrations of bone-like material (HA).

The misidentification chart of known concentrations of calcium chloride (bone-like material) is shown in Figure 3.5. Results show that there is better identification of

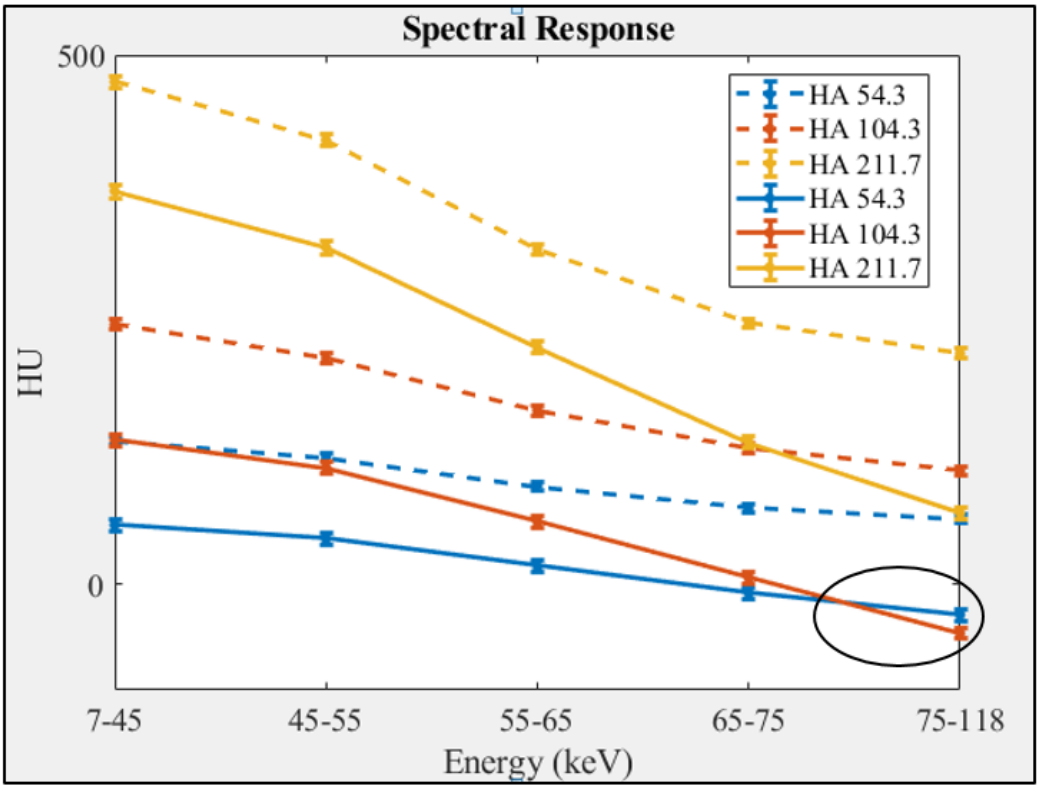

Figure 3.4: Solid lines represent spectral response of different concentrations of HA at 40 μA and dotted lines shows spectral response at 26 μA. The highlighted region illustrates that the attenuation values of HA 54.3 mg/cm^3 and HA 104.3 mg/cm^3 are so close and hence cannot be differentiated at high tube currents.

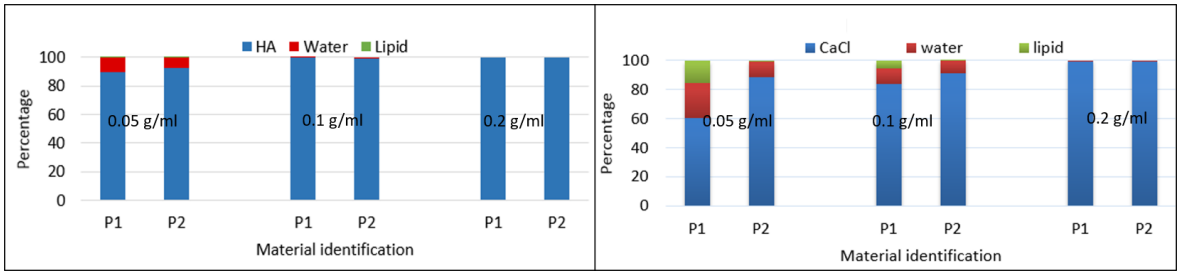

Figure 3.5: The misidentification chart displays better discrimination of lower concentrations of CaCl and HA with protocol 2 which is a combination of low broad energy bin and narrow high energy bins.

lower concentrations of calcium chloride with protocol 2 (combination of low and high energy bins). A broad low energy bin gives better identification of lower concentrations of calcium.

Quantification of 10% MTF from polished PMMA phantom at 110, 90 and 70 um yielded limiting resolution of the system as 2.6, 2.4 and 2.6 line pairs/mm respectively.

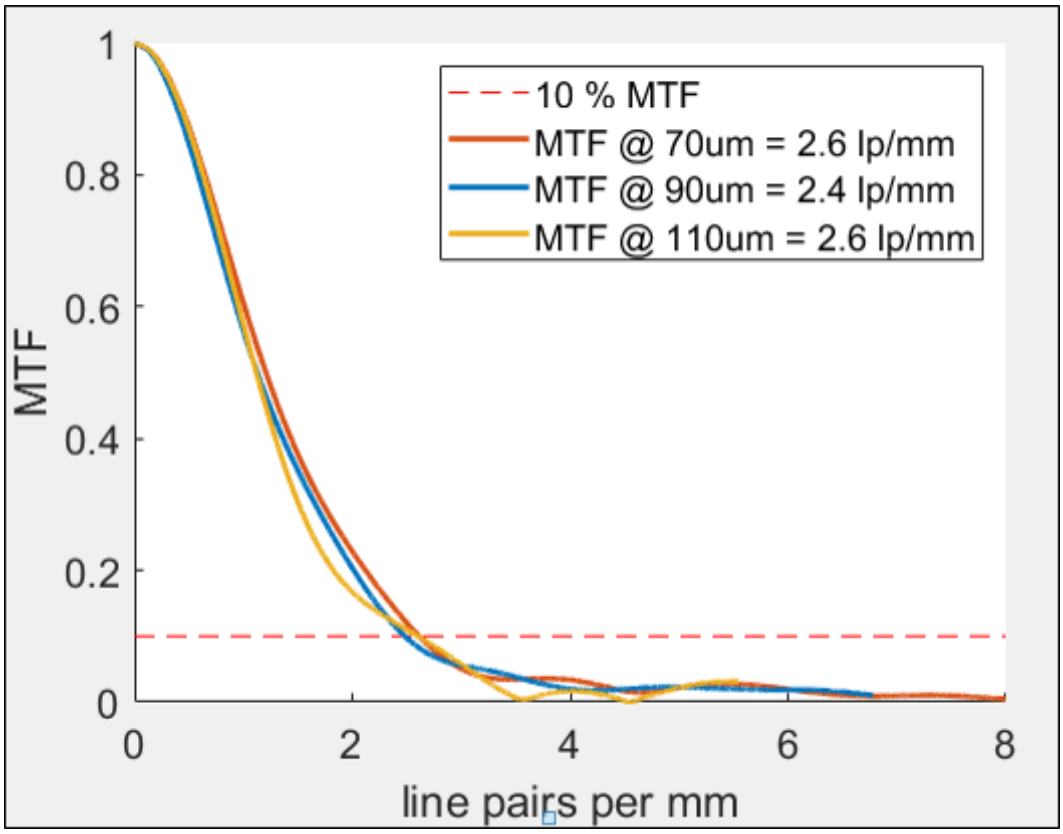

Figure 3.6: MTF calculated from the PMMA phantom for different pixel sizes shows that spatial resolution of the system is $\approx$ 2.5 lp/mm.

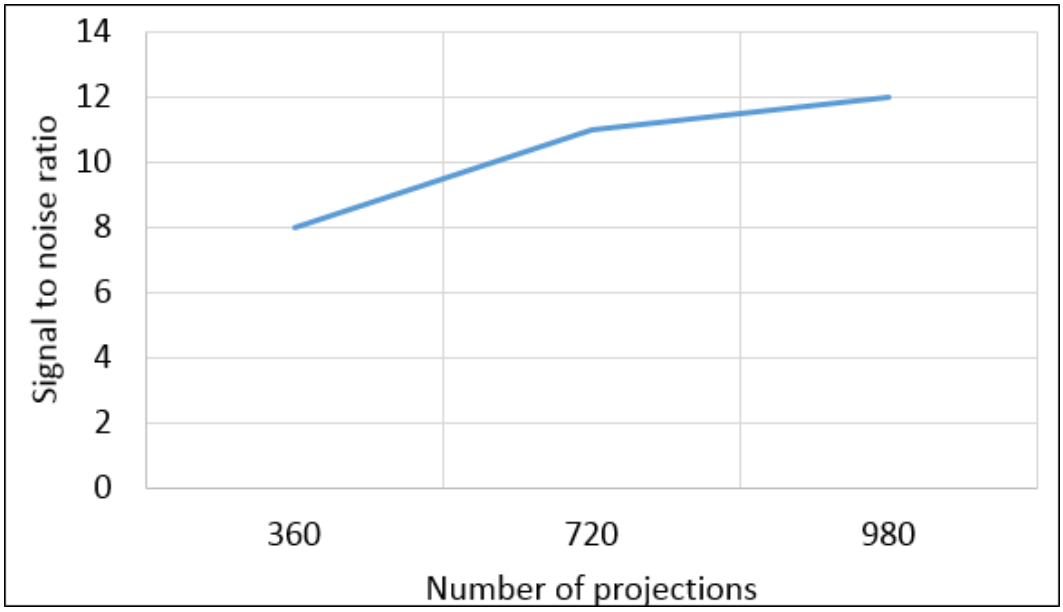

Figure 3.7: Graph demonstrates that the signal-to-noise ratio increased with the increase in the number of projections.

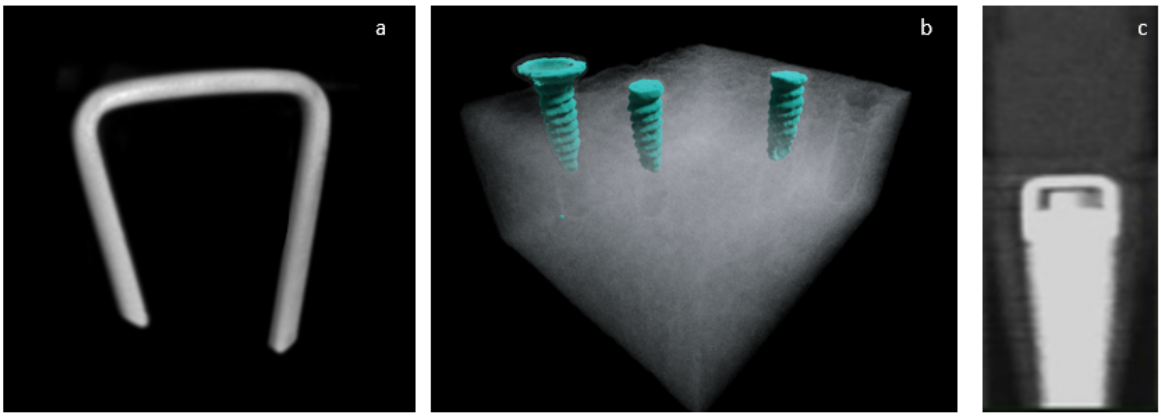

Figure 3.8: (a) K-wires used for fracture fixation scanned in air (b) biodegradable magnesium screws embedded in synthetic bone (c) titanium screw immersed in calcium chloride solution.

Considering the time for reconstruction while scanning bigger samples, 90 μm was selected as the optimal voxel size.

The SNR for different projections were measured as displayed in Figure 3.7. The SNR increased with the increase in the number of circular projections.

The protocol optimised for scanning bone-metal interface is given in Table 3.1.

Different biomaterials (stainless steel, magnesium and titanium) used in orthopaedics and dentistry were scanned with the optimised protocol to visualise the tissue-metal interface (Figure 3.8). Our results show that the tissue-metal interface can be clearly differentiated with the optimised protocol.

3.4 Discussion

The future of metal artefact reduction is a combined approach of improving the acquisition process using photon-counting detectors, along with advanced polychromatic iterative reconstruction techniques. In this chapter we have demonstrated the need for optimising acquisition parameters for imaging samples with metal implants. Protocol optimisation is crucial in improving material identification and signal-to-noise ratio. Noise and artefact reduction in data will improve material identification and quantification. Our results show that metal artefacts can be reduced at the acquisition phase by adding filters and utilising multiple energy bins. The

ability of MARS spectral CT to use the photon energy information provides the capability to identify specific materials in the scan volume and to avoid artefacts originating from beam hardening. Even though high energy photons reduce beam hardening artefacts, a broad low energy bin (7-45 keV) gives better identification of lower concentrations of calcium, which is crucial in identifying new bone growth. Hence a trade-off between beam hardening and material identification was essential resulting in the utilisation of low broad energy channel to study bone-metal interfaces. Also, use of a low energy bin provides better soft tissue contrast enabling identification of bone bruises from fractures and soft tissue injuries such as ligament and tendon damage. Better spatial resolution and signal-to-noise ratio was observed at 70 μm and 980 projections. Scanning time depends on the number of projections and exposure time. The reconstruction time depends on the voxel size to be reconstructed. Considering the reconstruction and scanning time, 90 μm and 720 projections were used for scanning tissue-metal interface. The spectral information is dependent on the energy bins and the degree of beam hardening caused by the sample. The MD algorithm relies on the information measured from the spectral domain and the decomposition bases that are used. Hence the protocol optimised for bone-implant imaging may not be optimal for other applications. Even though photon counting spectral CT reduces radiation dose, further studies to measure radiation dose with the optimised protocol are required prior to clinical imaging. In the next chapter the assessment of metal implant induced artefacts at the bone-metal interface using spectral CT will be discussed. We will also compare the advantage of using MARS photon counting spectral CT in assessing bone-metal interface with single and dual energy clinical CT.

3.5 Conclusion

A protocol was optimised for imaging samples with metal implants. The latest generation of MARS spectral CT scanners uses the same hardware and software for data acquisition, image reconstruction, material decomposition and visualisation as on the small bore scanner. The acquisition parameters used in this study should be scaled up for conducting in vivo scans of much larger structures with more tissue interfaces.

3.6 Dissemination of this research

The methods and results discussed in this chapter have led to the following journal abstract, a conference proceeding and the supervision of a Master student.

1. **Maya Rajeswari Amma**, Tara Dalefield, Aliakbar Atharifard, Aamir Younus Raja, Nigel Anderson, Benjamin Bamford, Anthony Butler. Optimisation of parameters for imaging bone metal interface using spectral photon counting computed tomography. Journal of Medical Radiation Sciences, Volume 65, 116-117 (Journal abstract).
   This abstract emphasises the need for optimising acquisition parameters for imaging bone-metal interface. I was the primary author of this abstract.

2. Butler, Philip H and Adebileje, Sikiru A and Alexander, Steven D and **Amma, Maya R** and Anjomrouz, Marzieh and Aghariomabad, Fatemeh and Atharifard, Ali and Atlas, James and Bamford, Benjamin and Bell, Stephen T et al. MARS preclinical imaging: the benefits of small pixels and good energy data. Developments in X-Ray Tomography XII, 11113, 111130C, International Society for Optics and Photonics, 2019 (Conference proceedings)

   This proceeding presents the benefits of improved specificity and sensitivity of MARS scanner and its applications in preclinical imaging. My contribution was in the data acquisition, data analysis and image interpretation of applications discussed under bone-implant imaging.

I also supervised Tara Dalefield (Master's student, University of Canterbury) in assessing bone ingrowth in titanium implants using MARS spectral CT. This study also led to two oral and one poster presentation

1. **Amma, M. R**. MARS- An emerging imaging modality to study bone metal interface. Maya Rajeswari presented the potential of MARS spectral CT to study bone-metal interface at the Australian and New Zealand Society of Nuclear Medicine (ANZSNM) Branch Meeting, Hamilton, New Zealand, September 2017.

2. Butler, Philip H and Adebileje, Sikiru A and Alexander, Steven D and **Amma, Maya R** and Anjomrouz, Marzieh and Asghariomabad, Fatemeh and Atharifard, Ali and Atlas, James and Bamford, Benjamin and Bell, Stephen T et al . MARS preclinical imaging: the benefits of small pixels and good energy data. Phil Butler presented the benefits of MARS preclinical imaging at SPIE Optics and Photonics conference, San Diego, August, 2019.

3. **Amma, M. R**, Tara Dalefield, Aliakbar Atharifard, Aamir Younis Raja, Nigel Anderson, Benjamin Bamford, Anthony Butler. Optimisation of parameters for imaging bone metal interface using spectral photon counting computed tomography. Maya Rajeswari presented the ePoster at the Australian Society of Molecular Imaging and Radiation Therapy (ASMIRT) conference held at Canberra, March, 2018.

3.7 Summary

• A protocol was optimised to scan specimens with metal implants.

• Even though metal artefacts reduced at narrow high energy bins, a combination of low and high energy bin is required for better material discrimination.

• MARS spectral photon counting CT is a potential tool for evaluating tissue-metal interface with reduced artefacts.

Chapter 4

Assessment of metal induced artefacts using spectral photon counting CT

The aim of this study was to assess the impact of metal induced artefacts on material density using MARS spectral photon counting CT. We hypothesised that the high spatial resolution, material specific quantitative information, and reduced metal artefacts of MARS photon counting CT technology will make it a promising imaging tool for analysing bone-metal interfaces. The effect of metal artefacts was determined on calcium chloride solutions/HA rods and biological samples. We compared images of calibration phantoms and biological samples with plate and multiple screws (titanium and stainless steel) obtained from MARS spectral CT, with single and dual energy clinical CT. The results discussed in this chapter has led to the following publication Amma *et al.* (2019).

4.1 Introduction

Bone fractures can occur due to traumatic incidents such as vehicle accidents, falls or due to some bone disease. Fracture management involves resetting the bone in place and immobilising it in a cast or splint to allow time to heal. Bone healing is a complex

and sequential set of physiological process in which the body facilitates restoration of bone tissue and function after a fracture. If bone healing is not progressing, orthopaedic prostheses are used to support damaged bone or replace a missing joint. Even though a large number of metals and biomaterials have been developed for various biomedical applications, titanium and its alloys are the most frequently used biomaterials in orthopaedics and dentistry Santos (2017). Solid implants are dense and suffer from problems of biomechanical mismatch and lack of adequate space for the growth of bone tissue into the implant. Porous scaffolds having similar architecture and mechanical properties of bone enhance bone-implant contact and promote bone ingrowth. Measurement of bone density in the vicinity of biomaterial helps in assessing fracture healing as well as the effectiveness of the implant treatment.

The inadequacies of existing imaging modalities in assessing bone-metal interface is explained in Chapter 3 Section 3.1. Previous studies demonstrated that the ability of MARS photon counting CT to use the high energy photon information will reduce metal artefacts at higher energy bins Rajendran *et al.* (2014). Also, utilisation of multiple energy channels will allow spectral photon counting CT to measure bone mineral density (BMD) and morphology simultaneously Mohsen (2017). We hypothesised that the simultaneous assessment of BMD and morphology at the bone-metal interface with reduced artefacts will provide more information of the density and morphological changes at the bone-metal interface. The MARS preclinical scanner is translatable to human imaging Panta *et al.* (2018).

4.2 Materials and methods

Common fracture sites (femur, knee and clavicle), requiring open reduction and internal fixation using plates and screws Huttunen *et al.* (2016); Zlowodzki *et al.* (2005) were investigated in this study to explore the potential of MARS spectral CT in assessing bone-metal interface. A calibration phantom as well as biological samples were scanned using a protocol optimised for scanning bone-metal interface as given in Chapter 3 Table 3.1. The qualitative and quantitative assessment of cupping and

streak artefacts was performed on the phantoms and biological samples.

4.2.1 Assessment of artefacts

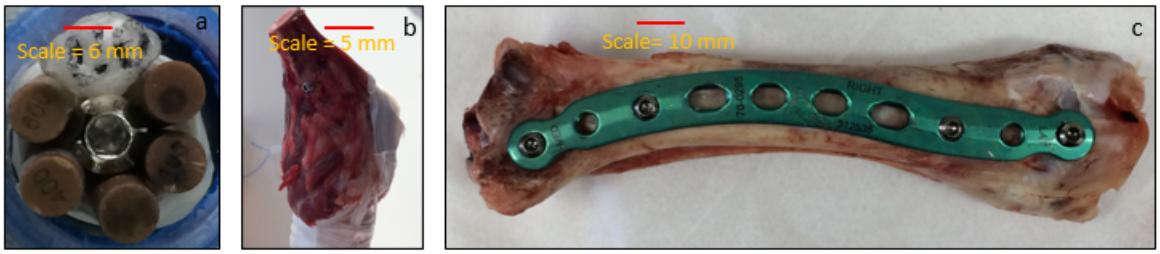

Figure 4.1: Calibration phantom and biological samples (a) A quality assurance (QA) cylindrical phantom containing lipid, water and different known concentrations of HA (104.3, 211.7, 404.3, 604.3 mg/cm^3) placed at the vicinity of the screw to assess impact of artefact on concentrations of the known HA rods. (b) sheep knee with titanium screw for quantitative evaluation of bone density and morphology (c) sheep clavicle with titanium plate and multiple screws for qualitative evaluation of streak artefacts at the bone-metal interface.

Titanium biomaterials, solid (screw) and porous (scaffold) were scanned with the optimised protocol to assess artefacts. Beam hardening makes it difficult to quantitatively interpret the images, because it changes the attenuation and complicates density measurement. We used calibration phantom consisting of known concentrations of bone-like material (calcium hydroxyapatite (HA)) as a quality assurance (QA) phantom. Calibration phantoms were used for experimentally establishing mass attenuation coefficients for the material decomposition algorithm and analysing material identification. Scaffolds were submerged in known concentrations of calcium chloride solutions (bone-like material) to assess the impact of metal artefacts on material density in the vicinity of the implant. Sequential scans of titanium scaffold submerged in known concentrations of calcium chloride solutions (0.05, 0.1, 0.2, 0.4, 0.8 g/ml) were performed. This allowed us to quantify calcium in and around the implant. Titanium scaffolds were washed and dried between scans. The vials of scaffold immersed in solution were centrifuged before each scan to ensure that air bubbles were not trapped within the pores. Multiple regions of interest were selected outside and inside the pores of the scaffold. Concentration of calcium within the pores

of the scaffold was averaged over the entire scaffold.

To assess the effect of solid implant on material density, a quality assurance (QA) cylindrical phantom consisting of known concentrations of HA along with water and lipid was scanned with a screw at the centre as in Figure 4.1 a. Further experiments were conducted with phantoms placed at 2 mm and 5 mm from the centre of the screw. Material information was used to determine concentration of calcium in the vicinity of the implant. A circular region of interest, each with an area of 1168 voxels across fifty slices of the calibration phantom was used to determine the effect of artefact on material concentration measured as mean ± standard error Raja *et al.* (2018).

4.2.2 Quantification of cupping artefacts

Cupping artefacts were quantified by using a horizontal line profile passing through the centre of a titanium phantom scanned in air. The cupping artefact in each energy bin was calculated as the percentage reduction in linear attenuation between the centre and the edges of the titanium screw along the horizontal line profile. The cupping artefact quantified from MARS spectral CT was compared with cupping artefacts from simulated datasets. For simulation, the source spectrum was simulated using a freely available tool from Siemens Boone (2019). We used two filters, aluminium and brass. The aluminium filter aims to model the intrinsic filtration of the MARS x-ray tube and brass filter models the extrinsic filter. The thresholds used correspond to 7 keV, 45 keV, 55 keV, 65 keV, and 75 keV to match those used in the scan. To simulate detector efficiency, we used CZT in modelling the sensor crystal. Physical effects such as fluorescence, scatter, charge sharing, and pulse pileup were not considered in the simulation.

4.2.3 Quantification of bone density and morphology

A sheep femur was scanned with and without a titanium screw to assess the impact of metal artefacts on bone density and morphology. To measure bone density and morphology, material decomposition was applied to the imaging data to distinguish water, lipid and calcium. We analysed one hundred slices with the centre of the screw

as slice 50. Quantitiative evaluation of bone density (cortical and trabecular) and bone morphology (cortical thickness, trabecular thickness and trabecular spacing) was performed.

The bone analysis tool integrated into visualisation software was tested and the measurements obtained from it were compared with the semi-automatic method used for bone morphological assessment described in Chapter 2 Section 2.2. The bone analysis tool enables the user to measure bone morphology such as thickness and spacing. The bone analysis tool calculates the local thickness and the local spacing of the given volume Hildebrand and Rüegsegger (1997). The input region of interest (ROI) can be segmented using manual threshold based methods or automatic segmentation methods such as Otsu to create a binary volume. The signed distance transformation Saito and Toriwaki (1994) is calculated at every voxel to measure local thickness/spacing at that location. The thickness calculation algorithm is adjusted to accommodate anisotropic voxel spacing. Thresholds were applied to 50 slices to segment the bone-like channel to cortical and trabecular bone. Otsu thresholding was applied to binarise images to measure bone architecture. The MARS visualisation tools were used to determine parameters that define bone strength such as cortical bone mineral density (BMD), trabecular BMD, cortical thickness, trabecular thickness and spacing.

4.2.4 Comparison

Single and dual energy images of the calibration phantom and biological samples with biomaterials were obtained from a single source dual energy CT scanner (Discovery CT750 HD, GE Healthcare, USA). The scan parameters for obtaining clinical CT image is as in Table 4.1. Dual energy on the 750 HD scanner is called Gemstone spectral imaging (GSI). GSI uses rapidly switching kVp technology (80-140 kVp at 0.25 milliseconds apart) to obtain dual energy information in the raw data space. From the raw data space monochromatic DECT images can be produced for any photon energy level between 40 and 140 keV. Monochromatic DECT images produced from projection space data are less affected by beam hardening artefacts. The GSI viewer

allows the radiologist to acquire the clinical information and adjust the energy level to reduce beam hardening artefacts. For improving the sharpness of the image, standard proprietary post processing techniques were used. For retrospective reconstruction, full mode was selected and images were reconstructed at 90 keV photon energy level with 30% adaptive statistical iterative reconstruction (ASIR) to see more detail and information around the screw. To sharpen the image, an Edge 3 filter was used.

Table 4.1: Scan parameters for calibration phantom and biological specimen with clinical CT

Clinical CT	**Single energy CT**	**Dual energy CT**
Scan type	**Helical**	**GSI Helical**
kV	**140**	**140**
mA	**250**	**630**
slice thickness	**0.625 mm**	**0.625 mm**
algorithm	**Bone plus**	**Standard**

4.3 Results

4.3.1 Assessment of artefacts

The impact of metal artefact on the concentrations of bone-like material in and around the implant were quantified.

Within the pores of the scaffold

The linearity response determines the relation between x-ray attenuation and material concentration. Energy information was used to plot the linearity response. Linearity of attenuation of calcium concentrations with five energy bins (Figure 4.2 a) establishes that the act of dividing counters into narrow bins reduces beam hardening. Results show that we were able to measure calcium concentrations accurately outside the implants. However, there was an overestimation of measured concentrations of calcium within the pores of the scaffold due to streak artefacts,

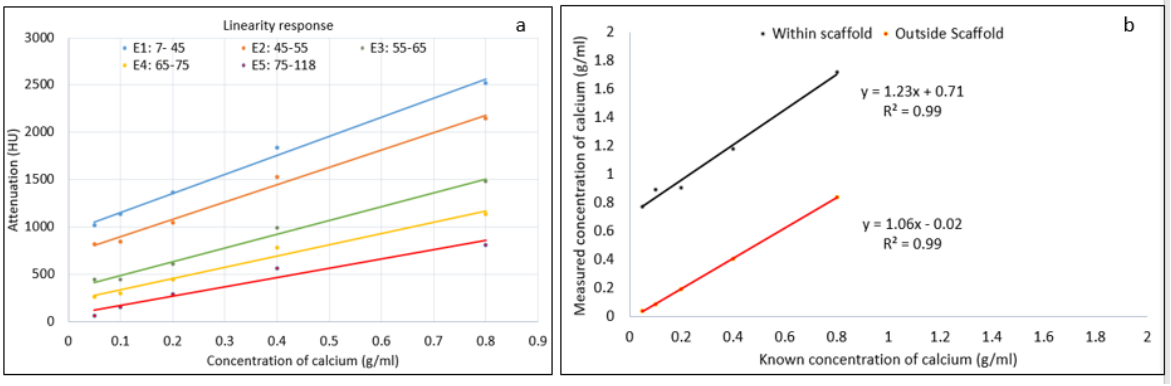

Figure 4.2: (a) Linearity response of attenuation of calcium depicting high correlation coefficient (0.96-0.99) (b) comparison of calcium concentration inside and outside the scaffold. Results demonstrate that we were able to measure known concentrations accurately outside the scaffold. The overestimation of calcium concentration within the scaffold is nearly constant and can be corrected by applying the correction factor.

photon starvation and partial volume effects. The increase in concentration of measured calcium within the scaffold, compared to concentration outside the scaffold, resulted in calculation of the correction factor as illustrated in Figure 4.2 b. The correction factor determined for calcium concentration was nearly constant (0.71 g Ca/ml). The variation could be due to the averaging of concentration over the entire scaffold. Further experiments on scaffolds with different architecture will indicate whether the correction factor is translatable to other specimens with implants.

At the vicinity of the implant

Material decomposition uses the energy dependence of x-ray attenuation of each voxel from different energy bins to estimate basis materials in the material volume. Circular regions of interest (ROI) were selected for 50 slices in each dataset to measure average concentration and standard error (Figure 4.3 a). Variation of measured concentration against known concentration of HA in the vicinity of the screw was quantified. We were able to measure known calcium hydroxyapatite concentrations at the proximities of the screw as in Figure 4.3 b. The accurate quantification of known calcium concentration demonstrates the ability of photon counting CT to measure BMD adjacent to the implant.

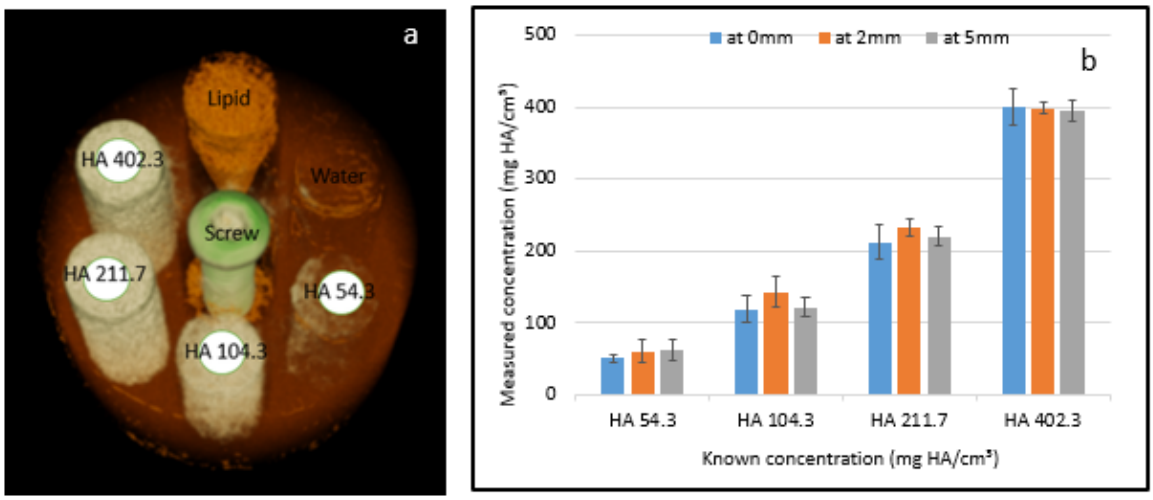

Figure 4.3: (a) MD image of the calibration phantom at 2 mm from the centre of the titanium screw. (b) Variation of measured concentration against known concentration of calcium hydroxyapatite (HA) at the vicinity of the screw shows that MARS spectral CT is able to measure known concentrations accurately outside the screw. This demonstrates the reliability of photon counting CT in measuring BMD in the vicinity of the implant.

Photon counting spectral CT has the ability to perform data acquisition and processing at multiple energy bins. The differences in material density or atomic numbers can be displayed either in greyscale or in colour. An example attenuation image of sheep clavicle with titanium plate and multiple screws in five energy bins is shown in Figure 4.4. The images show a decrease in the streak artefacts at the vicinity of the titanium plate with higher energy bins. Streak artefacts from metal in CT images reduce diagnostic accuracy and limit the assessment of complications such as osteolysis and implant loosening at the bone-metal interface. The ability of photon counting detectors to separate out high energy photons facilitates the visualisation of bone-metal interfaces with fewer artefacts.

The 3D volume rendering of the sheep clavicle with a titanium plate and multiple screws is displayed in Figure 4.5 and a sheep femur with a stainless steel plate and multiple screws is shown in Figure 4.6. Our results show that the bone-metal interface could be rendered almost artefact free using photon counting spectral CT. Marked reduction in artefacts can be achieved using photon counting detectors and polychromatic iterative reconstruction.

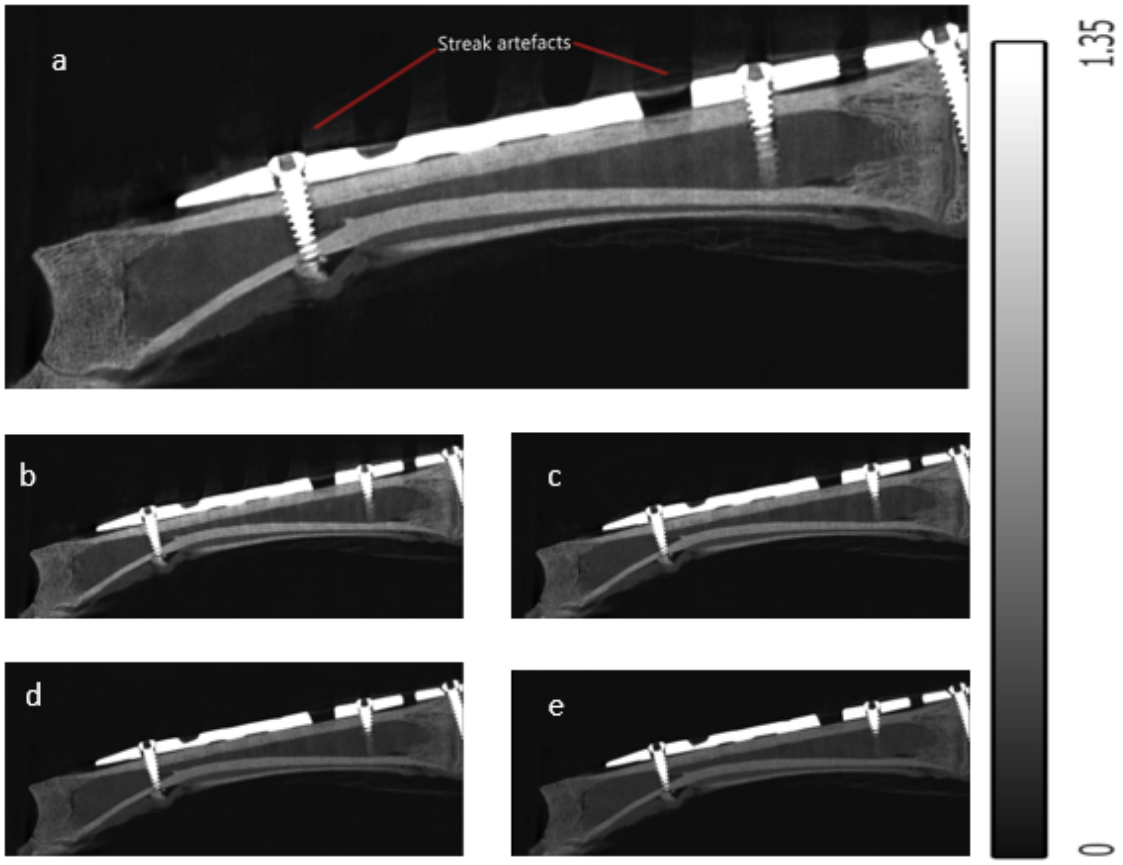

Figure 4.4: The coronal reconstruction of slice 289 of sheep clavicle with plate and screws at (a) 7-45 keV (b) 45-55 keV (c) 55-65 keV (d) 65-75 keV (e) 75-118 keV. The scale bar indicates linear attenuation (cm^{-1}). The figure demonstrates a decrease in streak artefacts in the bone-metal interface with an increase in energy bins. The artefact free bone-metal interface enables radiologists to diagnose implant loosening and bone resorption.

4.3.2 Quantification of cupping artefact from energy images

The cupping effect is displayed as attenuation line profiles in Figure 4.7. Cupping artefacts quantified from simulation were 7.6%, 5.2%, 4.7%, 4.3% and 4% respectively. The cupping effect from spectral CT images was 8.7%, 3.6%, 1.7%, 1.3% and 1.2% for five energy bins. Results demonstrate that there is a decrease in cupping artefact with increase in energy bins.

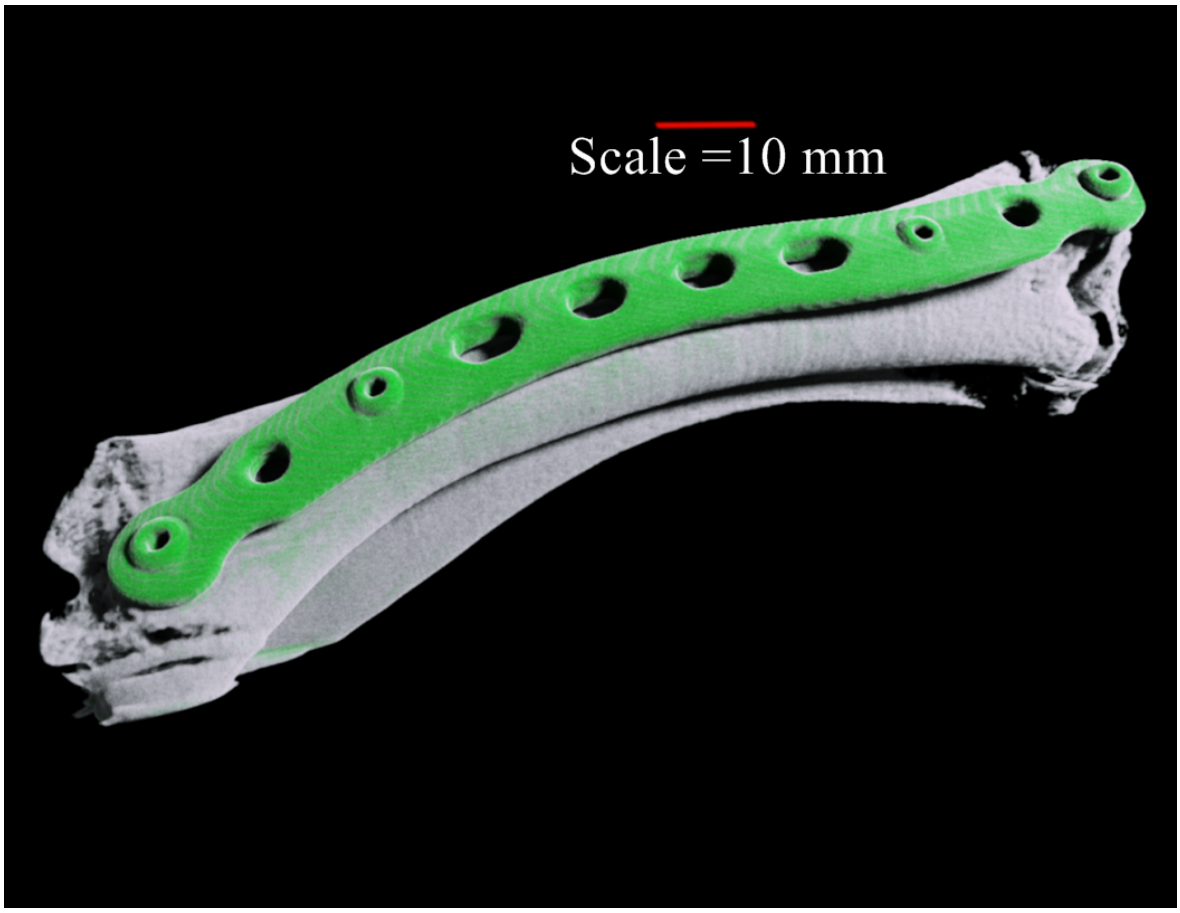

Figure 4.5: 3D volume rendering of sheep clavicle with titanium plate and multiple screws. Reduced artefacts and adequate contrast differentiation leads to better differentiation of implant from bone.

Table 4.2: Bone morphological assessment at the bone-metal interface with and without implant.

Bone morphology	Without implant	With implant
Cortical BMD	850 ± 30 mg/cm^3	880 ± 30 mg/cm^3
Trabecular BMD	240 ± 80 mg/cm^3	260 ± 60 mg/cm^3
Cortical thickness	1.4 ± 0.25 mm	1.4 ± 0.21 mm
Trabecular thickness	0.33 ± 0.06 mm	0.36 ± 0.07 mm
Trabecular spacing	0.80 ± 0.05 mm	0.81 ± 0.06 mm

4.3.3 Quantification of bone density and morphology

The mass attenuation values obtained from calibration vials were used for the MD of sheep knee with a screw. The MD images of the sheep knee with a screw is exhibited

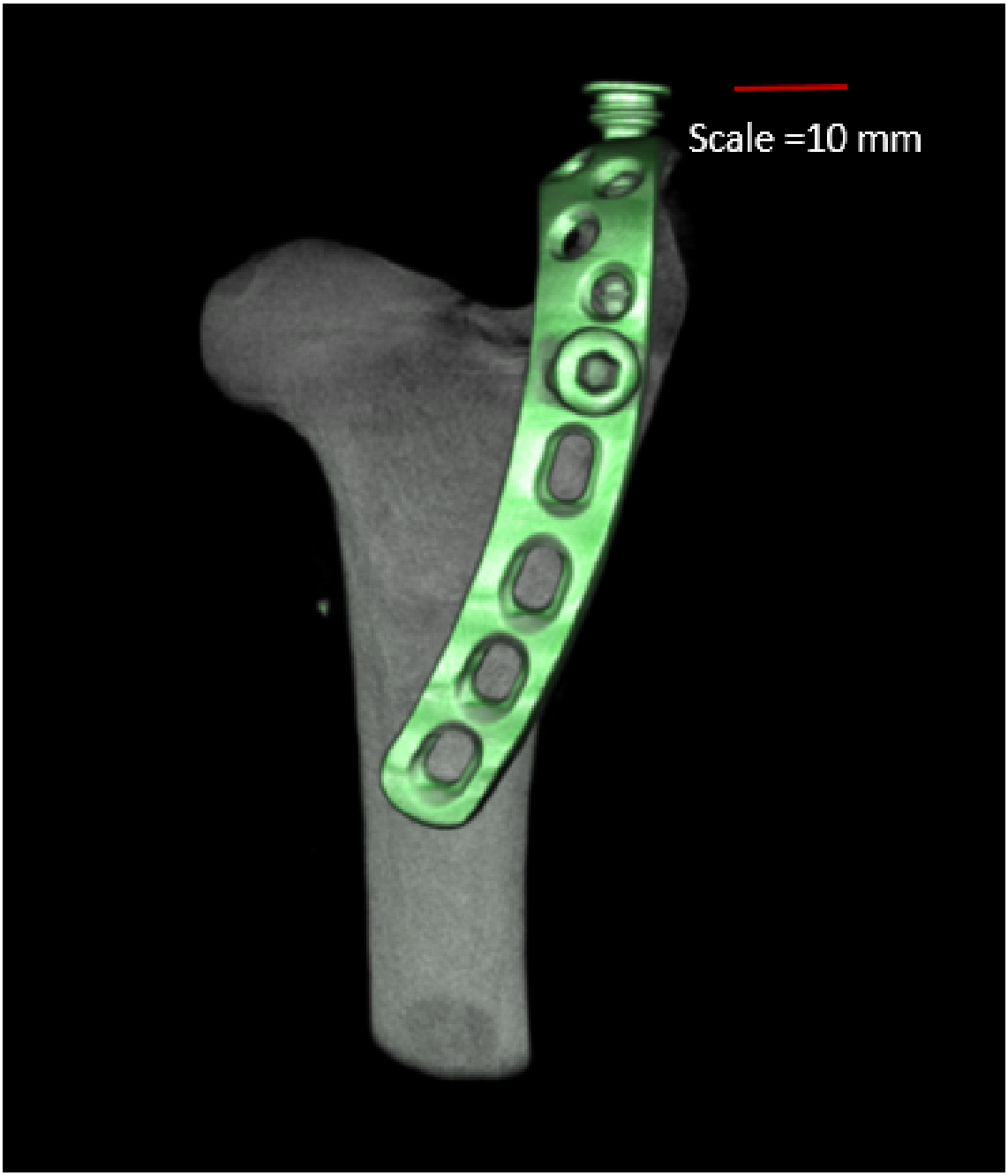

Figure 4.6: 3D volume rendering of sheep femur with stainless steel plate and multiple screws. Reduced artefacts at the bone-metal interface enables assessment of implant loosening and osteolysis.

in Figure 4.8. Bone health assessment requires knowledge of bone density as well as morphological parameters such as thickness and spacing. Utilisation of multiple energy bins enables MARS photon counting spectral CT to measure density and morphology simultaneously. MD images of HA-like channel were used to measure bone mineral

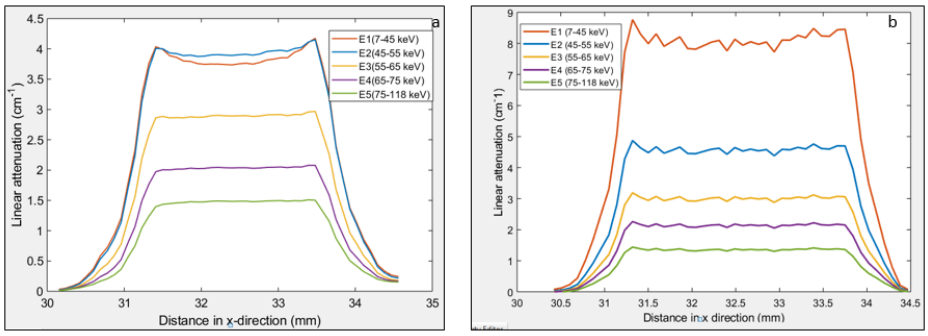

Figure 4.7: Quantification of cupping artefact from the (a) simulation (b) MARS images. Cupping artefacts quantified from spectral images of the titanium phantom from MARS reduced from 8.7% to 1.2% from the first to the fifth energy bin.

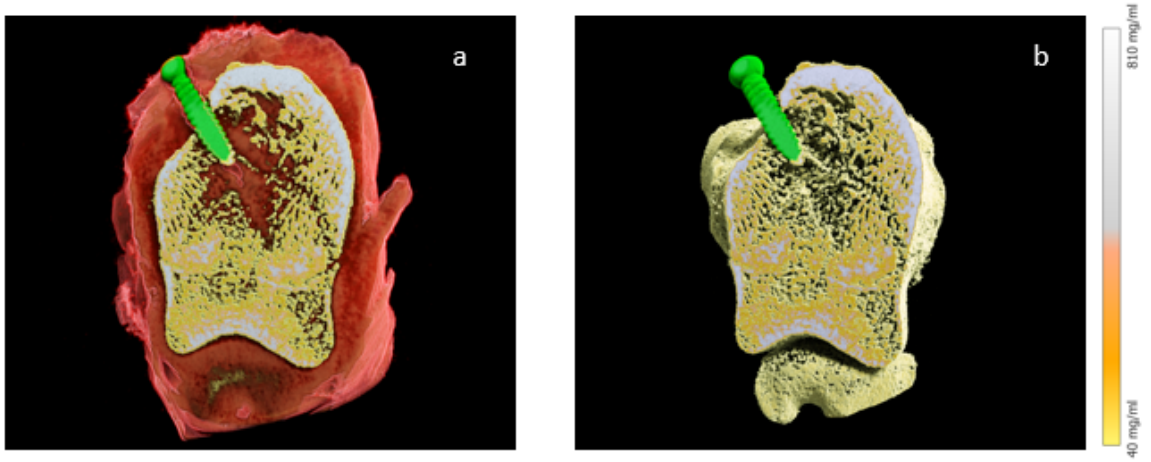

Figure 4.8: MD image of sheep knee with screw (a) Material channel containing soft tissue and bone-like material (b) material channel containing bone-like material and screw. The density of titanium screw is higher than bone and hence screw appears in the bone-like channel. The scale bar indicates density of bone-like material in mg/ml

density and morphology. The bone density and morphological parameters with and without a screw is given in Table 4.2. The quantitative evaluation of bone strength with and without a screw demonstrates that the bone density and morphology was not affected by the presence of the implant. This is in agreement with the calibration phantom density assessment which shows that spectral photon counting CT could measure accurate density outside the implant.

The bone analysis tool integrated into MARS Vision was used to measure bone morphology such as thickness and spacing using a multi-step process as illustrated in

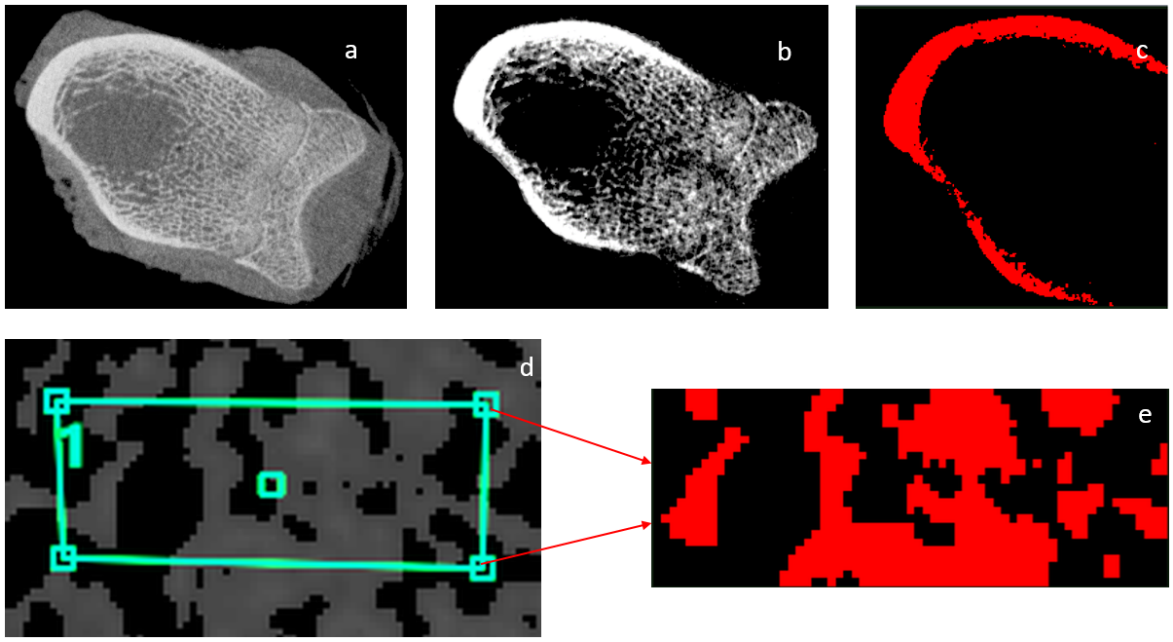

Figure 4.9: MARS visualisation (a) attenuation image of sheep knee at 7-45 keV (b) MD image displaying HA like channel (c) Binary segmented region for determining cortical thickness and density from HA-like channel (d) region of interest selected for analysing trabecular thickness and spacing (e) segmented trabecular region for measuring thickness and spacing from HA-like channel

Table 4.3: Comparison of bone density and morphological measurements obtained from bone analysis tool and ImageJ. Fifty slices were analysed to determine bone health

Bone morphology	Bone analysis tool	Image J
Total BMD	317 ± 18 mg/cm^3	296 ± 25 mg/cm^3
Cortical BMD	721 ± 14 mg/cm^3	671 ± 24 mg/cm^3
Trabecular BMD	154 ± 7 mg/cm^3	168 ± 14 mg/cm^3
Cortical thickness	1.5 ± 0.05 mm	1.3 ± 0.10 mm
Trabecular thickness	0.46 ± 0.07 mm	0.39 ± 0.10 mm
Trabecular spacing	0.65 ± 0.10 mm	0.66 ± 0.10 mm

Figure 4.9. MD images of HA-like channel used to determine bone strength is displayed in Figure 4.9 b. Thresholds were applied to 50 slices to separate HA-like channel to cortical and trabecular bone. Otsu thresholding was applied to binarise images. Binary images were used to measure morphological parameters such as thickness and spacing. For measuring cortical density and thickness, a cortical counter was generated for each

slice as shown in Figure 4.9 c. Region of interest selected for quantifying trabecular density and morphology is displayed in Figure 4.9 d. Segmented trabecular region for measuring trabecular thickness and spacing is shown in Figure 4.9 e.

The bone density and morphology parameters obtained from the bone analysis tool was compared with semi-automatic method to ensure the reproducibility of the results. Table 4.3 compares the quantitative evaluation of parameters such as cortical and trabecular density, cortical and trabecular thickness and spacing which defines bone health.

4.3.4 Comparison

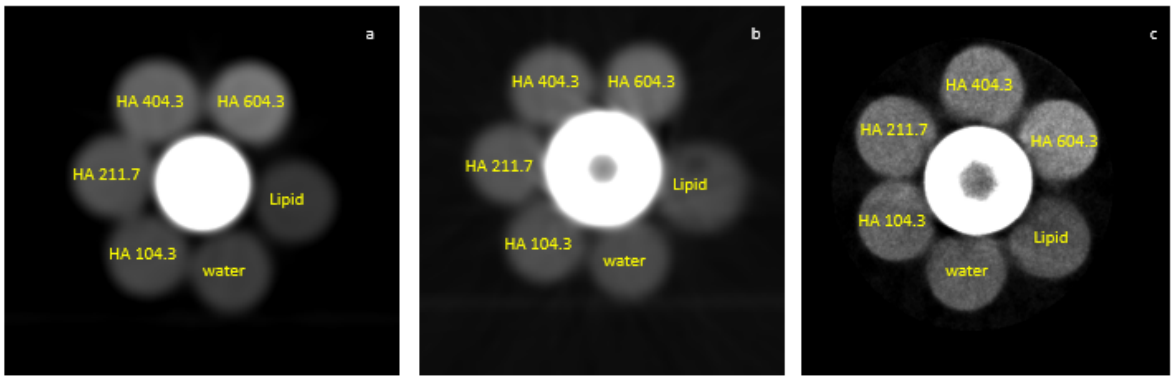

Figure 4.10: Qualitative evaluation of calibration phantom in the vicinity of the titanium screw (a) single energy CT (b) dual energy CT (c) spectral photon counting CT (75-118 keV) . These images exhibit streak artefacts in the single and dual energy CT images.

The MARS images were reconstructed at a voxel size of 90 μm wide. The coronal images from the clinical CT were reconstructed at a voxel size of 340 μm. Higher spatial resolution of MARS photon counting spectral CT compared to dual energy CT, enables visualisation of finer details of trabecular thickness and spacing near implants with less artefacts. The comparison of calibration phantom images depict that spectral CT images has fewer streak artefacts at the phantom-metal interface when compared to clinical CT (Figure 4.10). The images of sheep clavicle with titanium plate and multiple screws demonstrate that the bone-metal interface is clearly visualised in spectral CT images (Figure 4.11). The streak artefacts were more pronounced in dual energy CT images compared to spectral CT images for a sheep femur with stainless steel plate

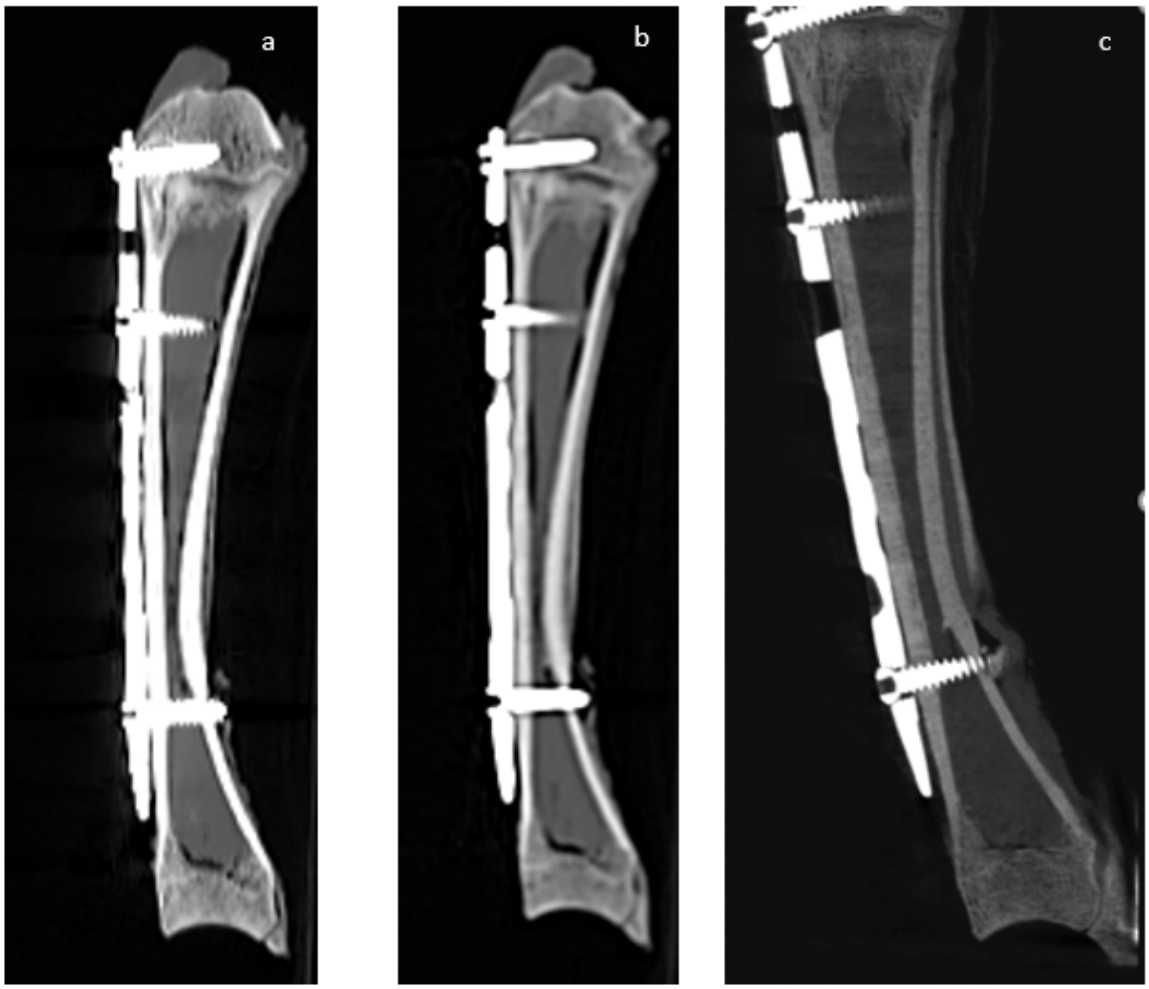

Figure 4.11: Sheep clavicle with titanium plate and multiple screws (a) single energy CT (b) dual energy CT (c) MARS spectral CT (75-118 keV). The photon counting spectral CT images displays how well the grooves of the screw is integrated with the bone adjacent to it.

and screw (Figure 4.12). Qualitative evaluation of spectral CT images of a sheep knee with a titanium screw, against single and dual energy clinical CT (Figure 4.13) shows that photon counting CT can visualise bone-metal interface with fewer artefacts as well as finer structures adjacent to the implant that enables assessment of bone strength. Data from spectral CT have five to eight energy bins which provides more energy information when compared to dual energy CT.

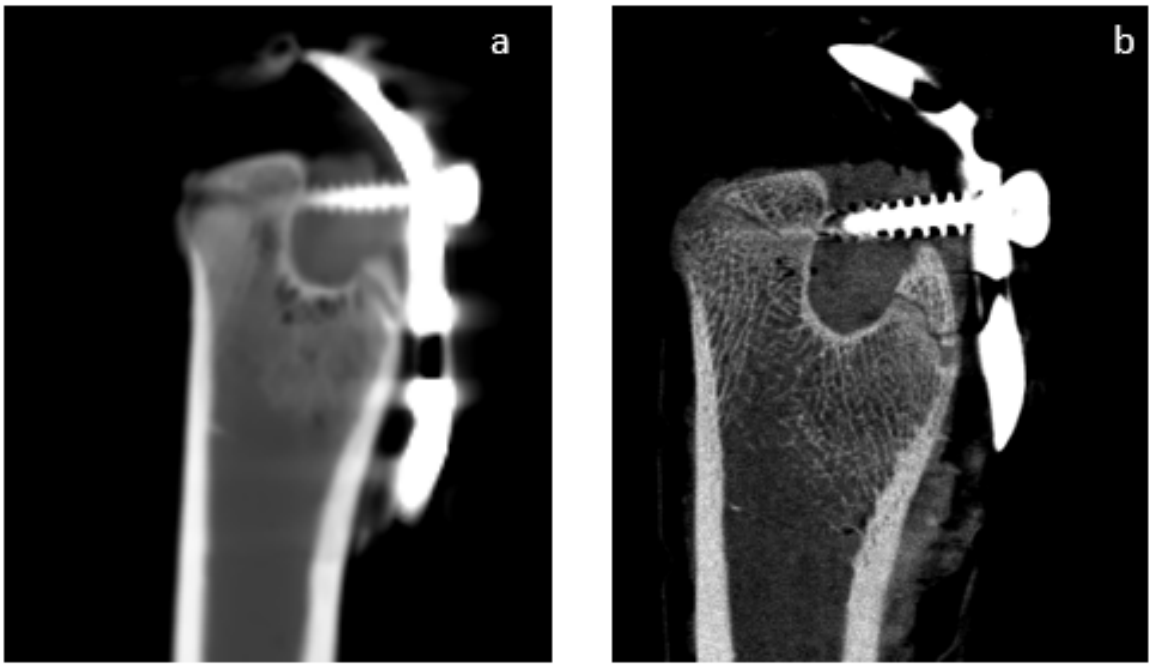

Figure 4.12: Sheep femur with stainless steel plate and screw (a) dual energy CT (c) MARS spectral CT (75-118 keV). Reduced metal artefacts at the bone-stainless steel interface is depicted in the MARS spectral CT images compared to clinical dual energy CT.

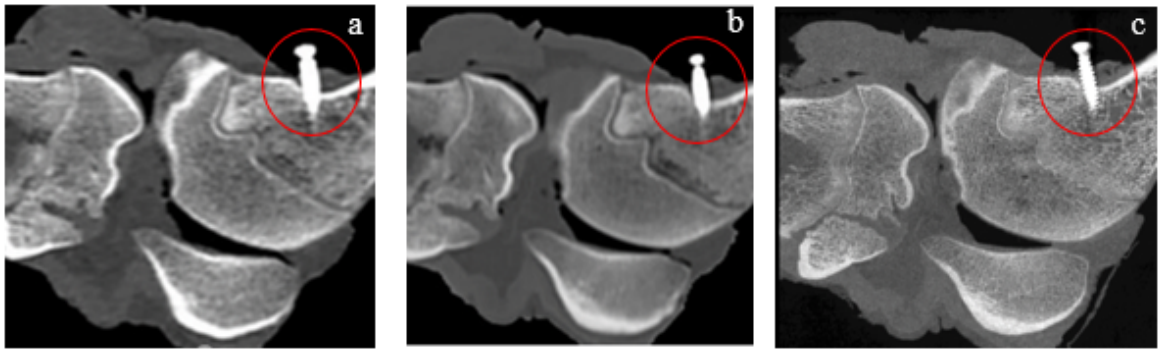

Figure 4.13: Sheep knee with titanium screw (a) single energy CT (b) dual energy CT (c) MARS spectral photon counting CT (75-118 keV). In spectral CT images the soft tissue as well as the trabecular structures in the vicinity of the screw can be clearly visualised.

4.4 Discussion

Existing imaging modalities have limitations in assessing bone-metal interface due to metal artefacts. A novel imaging tool for visualisation of the bone-metal interface with fewer artefacts is desirable. MARS spectral photon counting CT is a three

dimensional, non-invasive and non-destructive imaging modality to assess bone-metal interface with reduced metal artefacts. In this study we explored the potential of MARS photon counting CT in assessing bone-titanium and bone-stainless steel metal interfaces. We demonstrated that MARS spectral CT can assess bone-metal interface with fewer artefacts when compared to clinical CT. It's ability to image near metal might improve the imaging of common fracture treatments such as screws, plates, and k-wires. This might enable earlier detection of complications such as osteolysis, peri-implant micro-fractures, and infection. One of the major limitations of the study is that the studies were performed on excised sheep specimens and will have significant differences when it is extrapolated to a clinical situation for imaging a human torso.
We demonstrated that bone density and morphology can be quantified using the MARS visualisation tool. The presence of fewer artefacts in bone implant specimens enables segmentation of bone into cortical and trabecular regions leading to the simultaneous measurement of cortical and trabecular density (mg/cm^3). The improved spatial resolution of MARS photon counting CT compared to clinical CT enables visualisation of bone architecture such as trabecular thickness and spacing adjacent to the metal. The ability of the spectral CT to differentiate soft tissue with high energy bins (75-118 keV) has important clinical applications. MARS's ability to quantify bone structure and mineralisation might provide insight in to the fracture healing, delayed healing, and non-union. The major limitation of the study is that only qualitative comparison of bone-metal interface was performed. During this study the software used in clinical CT for bone density measurement was not available for comparison of the BMD measurements. An automated segmentation to segment the image using an interactive image segmentation method is an ongoing investigation in the MARS project. This automated segmentation method can be implemented in the bone analysis tool to make it more reliable and user independent. The bone analysis tool can be modified to assess morphological parameters such as trabecular number, volume fraction, bone surface per total volume, connectivity density, and structure model index which provides more insight to the bone strength. Improvement in material reconstruction algorithms will facilitate architectural analysis of biomaterial scaffolds and quantification of bone healing within the pores of the scaffolds. In the

next chapter we will discuss quantification of bone healing at the vicinity of the implant and compare the clinical utility of spectral photon counting CT with existing imaging modalities in determining bone healing.

4.5 Conclusion

MARS spectral photon counting CT can reduce metal artefacts by using narrow energy bins as well as high energy photons. MARS spectral photon counting CT can accurately quantify bone density and morphology outside the implant. Overestimation of bone density within the pores of the scaffold due to artefacts can be reduced by applying a correction factor. Spectral photon counting CT has the potential to more accurately assess bone health and analyse bone-metal interfaces with less pronounced artefacts. Comparison of spectral photon counting CT images with clinical CT demonstrates that MARS spectral CT will be a potential tool for evaluating bone-metal interface.

4.6 Dissemination of this research

The methods and results discussed in this chapter have led to a conference proceeding and a manuscript under preparation.

1. **Amma M.R**, Anthony P. H. Butler, Aamir Y. Raja, Benjamin Bamford, Philip Butler, et al. Assessment of metal implant induced artefacts using photon counting spectral CT, Proc. SPIE 11113, Developments in X-Ray Tomography XII, 111131D (September 2019); doi: 10.1117/12.2531003.
   This conference proceedings presents the assessment of metal implant induced artefacts in the vicinity of the implant. I am the primary author of this paper.

2. **Amma M.R** et al: Spectral photon counting CT to assess bone-metal interfaces. (Under preparation) This manuscript demonstrates the potential of MARS spectral photon counting CT in assessing bone-metal interface with reduced

artefacts in comparison with clinical single and dual energy CT. I am the primary author of this manuscript.

The titanium implants used in this study were provided by Dr.Peter Walker, Dr.Alex Malone (Orthopaedic surgeon, Christchurch hospital), Dr.Ram Chandru (Orthopaedic surgeon, Southern Cross Hospital) and CReATE group (University of Otago, Christchurch). The single and dual energy clinical CT images was acquired using GE HD 750 scanner by Dr. Nadia Mitchell, Dr. Samantha Murray (Lincoln University) and Ms. Jenifer Clarke (Radiographer). I contributed to the study conception and design, data collection and processing, analysis and interpretation. I am the primary author of the conference proceedings and presented this work in SPIE optics and Photonics conference at San Diego. I collaborated with HIT Lab, University of Canterbury, in developing bone analysis tool for measuring bone architectural parameters which is integrated in MARS Vision for future users. This research also led to three oral presentations

1. **Amma, M. R**, Tara Dalefield, Aamir Younus Raja, Nigel Anderson,Anthony Butler. Spectral CT Imaging of bone and implants using MARS CT. Amma, M. R presented at University of Otago Student Research Symposium (August 2017, Dunedin, New Zealand).

2. **Amma, M. R** Study of bone health using MARS spectral photon counting CT delivered to medical students at Christchurch school of Medicine, New Zealand, November 2017.

3. **Amma, M. R** Advantages of photon counting spectral CT in assessing bone-metal interfaces, CMDT emerging researcher award presentation held by MedTech CoRE, Auckland, July 2019.

4.7 Summary

• MARS spectral CT can visualise bone-metal interface with less pronounced artefacts.
• Cupping artefacts quantified from spectral images of a titanium cortical screw

reduced from 8.7 % to 1.2 % from the first to fifth energy bin.

• There is an overestimation of measured concentration of calcium (0.71 g Ca/ml) within the pores of the scaffold.

• The bone density and morphological parameters of a sheep knee quantified from bone analysis tool was compared with Image J.

• The higher spatial resolution of MARS spectral CT compared to single and dual energy clinical CT enables orthopaedic surgeons to view bone structures adjacent to implant.

• MARS photon counting CT has the potential to assess bone-metal interface with fewer artefacts and can help orthopaedic surgeons to quantify bone healing and osteolysis.

Chapter 5

Quantification of bone healing in the vicinity of the implant

The purpose of this study was to compare the potential of MARS spectral photon counting CT to assess bone healing in the vicinity of a titanium implant with respect to existing imaging modalities. We hypothesised that the ability of the MARS CT scanner to quantify bone density outside an implant with reduced artefacts along with high spatial resolution might enable assessment of bone healing in the vicinity of the implant. We qualitatively evaluated images obtained from spectral photon counting CT with plain radiographs, iDXA, and clinical single and dual energy CT. The bone mineral content measured from the MARS scanner were compared with iDXA. The results discussed in this chapter has led to a manuscript (Under preparation).

5.1 Introduction

Fracture fixation with implants (titanium, stainless steel or magnesium) is a widely used clinical application to restore the alignment of fractured bones or to enable fracture healing process Agarwal *et al.* (2014). There are several factors which affect fracture healing processes such as age, bone type, pre-existing bone pathology and drug therapy. Bone healing is a spontaneous and complex regenerative processes divided into four stages such as inflammation, soft callus formation, hard callus formation

and bone remodelling Weiss *et al.* (2009); Gerstenfeld and Einhorn (2003); Schindeler *et al.* (2008). The periosteum, the connective tissue membrane covering the bone mainly determines the healing process. Other sources of precursor cells which develop into chondroblasts (cell producing components of extracellular matrix) and osteoblasts (cell from which bone develops) essential for bone healing are endosteum, small blood vessels, bone marrow and fibroblasts. Seven to nine days after the fracture, the periosteal cells proximal to the fracture gap develop into chondroblasts and periosteal cells distal to the fracture gap develop into osteoblasts. When osteoblasts produce osteoid rapidly, woven (fibrous) bone is produced which is gradually replaced by lamellar bone (in the form of trabecular bone) during a process called bony substitution. This stage is called the soft-callus stage and lasts for 2-6 weeks. Bone remodelling begins as early as 3 to 4 weeks after fracture in which the lamellar bone is substituted with compact bone (hard callus formation). Bone remodelling may take 3 to 5 years to complete.

There are a number of invasive and destructive traditional methods such as histology, pull and push through testing and removal torque analysis to evaluate the bone density and osseointegration Turkyilmaz *et al.* (2006); Seong *et al.* (2009). Quantitative and qualitative assessment of fracture healing using non-invasive imaging methods is a challenging problem in clinical orthopaedics Morshed (2014). Traditionally, plain radiographs are used to determine fracture healing, but the assessment is mainly qualitative in nature Kooistra *et al.* (2010); Davis *et al.* (2004). The radiographic criterion used for defining fracture union is the bridging of fracture by callus, trabeculae or osseous bone Corrales *et al.* (2008). Also, calcification in newly laid down bone cannot be detected until weeks using x-ray. According to Grigoryan *et al.* (2003), CT is advantageous over plain radiographs in evaluating early fracture healing. Computed tomography (CT) and Dual energy x-ray absorptiometry (DXA) quantifies the bone mineral content (BMC) and the density of the newly formed bone in the vicinity of the implant Augat and Schorlemmer (2006). The advantage of CT over DXA is that while DXA measures areal BMD (g/cm^2), CT measures volumetric BMD (g/cm^3). The major limitation of the CT is the artefacts at the bone-metal interface due to multiple mechanisms such as beam hardening, scatter and partial volume effect. HR-pQCT can

be used to assess bone density along with micro-architectural changes, but its gantry size limits its assessment to peripheral fracture sites.

Previous studies with photon counting spectral CT have proved its potential to assess bone-metal interfaces with fewer artefacts Rajendran *et al.* (2014); Rajendran (2016); Amma *et al.* (2019). Also, simultaneous quantification of bone mineral density and micro-architecture, made possible by the utilisation of multiple energy bins and high spatial resolution, is an added advantage to assess fracture healing in the vicinity of the metal implant. The aim of this study was to compare the clinical utility of photon counting spectral CT in assessing bone healing with respect to existing imaging modalities.

5.2 Methods and materials

Six four-month-old male sheep were used in this study to assess fracture healing at the bone-metal interface (Lincoln University Animal Ethics Approval (AEC 2018-31)). Two sheep were used as controls and were not fed with strontium. Four sheep were fed daily with strontium ranelate (33 mg/kg) in a gelatin capsule two weeks prior to and after surgery. Under the care of a veterinarian, the six sheep were given prophylactic cephoxitin sodium (500 mg) prior to surgery to prevent infection from the implant, as titanium is a foreign body. The sheep were given intramuscular (IM) ketamine 10 mg/kg live weight and Diazepam 0.5 mg/kg on induction, then incubated with a 5.0-7.0 mm endotracheal tube and put onto isoflurane in oxygen gas inhalation, 1.5-3 v/v % (volume/volume percent) to effect surgical plane anaesthesia. The sheep were placed in a supine position on the operating table. The operative areas on the proximal and medial tibia were prepared by shaving, then painting the area with betadine antiseptic solution. Under sterile conditions, flaps were raised from the proximal and medial tibia of both left and right rear legs to expose the bone. A 4 mm drill hole was made in each tibia and a titanium screw used in dentistry was used for internal fixation to study membranous bone healing at the bone-titanium interface. The flaps were closed and sutured and the sheep were given pain relief (Temgesic (324 μg) administered every 8 hours for two days). The six sheep were returned to field post surgery and monitored

twice daily for four days to assess well-being and the need for analgesia as well as to change dressing. Every two weeks after the placement of titanium implant, one of the four strontium treated sheep was euthanised by penetrating captive bolt. The blood samples were taken ante mortem for alkaline phosphatase test associated with bone formation. For all sheep at post mortem, the flaps over the tibia were raised again and bone specimens of the sheep were collected in 0, 2, 4, 6 and 8 weeks after surgery. Specimens were preserved in 10 % formalin and refrigerated at 4 °C.

The collected specimens (n= 12, two from each sheep) were imaged with x-ray, iDXA, single and dual energy clinical CT, and MARS photon counting CT. Qualitative evaluation included comparison of fracture gap, external callus appearance and bridging of bone with all imaging modalities. For quantitative assessment the bone mineral content was measured by drawing freeform regions of interest (ROI) in the vicinity of the implant. The bone mineral content measured from spectral photon counting CT was compared with iDXA. An alkaline phosphatase level test (ALP test) was performed on the blood samples collected from the sheep to identify bone remodelling at the fracture site. Alkaline phosphatase testing measures the level of alkaline phosphatase which aids bone formation. The ALP level in a healthy adult sheep is 27-156 units per litre. An abnormal level of alkaline phosphatase indicates bone remodelling.

5.2.1 Imaging modalities

5.2.1.1 Plain x-ray radiograph

Digital radiography was performed on a Digital Diagnost C90 (Philips Healthcare) in two views (anteroposterior and lateral) according to standard procedures. The images were acquired at 52 kVp with a spatial resolution of 148 μm. The fully processed images were automatically sent to the PACS station in DICOM format.

5.2.1.2 Clinical conventional and dual energy CT

Conventional and dual energy CT images were obtained from a single source dual energy CT scanner (Discovery CT750 HD, GE Healthcare, USA). Single energy CT

images were obtained at 140 kVp with a slice thickness of 0.625 mm. The images were reconstructed using bone plus algorithm to enhance bone quality at the proximity of the implant. Dual energy on 750 HD scanner, also known as Gemstone spectral imaging, uses an x-ray source with fast kVp switching between two kilovoltages (80 and 140 kVp at intervals of 0.25 ms) to produce low and high energy x-ray spectra. Monochromatic DECT images at 90 kVp were generated from projection space data to reduce beam hardening artefacts. For retrospective reconstruction, full mode was selected and images were reconstructed using a standard algorithm with 50 % adaptive statistical reconstruction technique (ASIR) to view the details of the tissues around the screw. To improve the visualisation of tissue in the vicinity of the implant, a vendor-specific metal artefact reduction software was used. With Gemstone spectral imaging metal artefact reduction software, the metal implant is segmented based on the CT number threshold. The metal artefact corrected image is overlaid on the original image by forward projection. The metal artefact reduction software replaces the regions around the implant suffering from photon starvation with information from accurate projection measurements improving the image quality Brook *et al.* (2012); Lee *et al.* (2012).

5.2.1.3 Spectral photon counting CT

Spectral photon counting images were obtained from MARS CT scanner (MARS 11, MARS Bioimaging Ltd, New Zealand). The protocol optimised for imaging bone-metal interfaces was used for scanning the samples. For image acquisition, a tube voltage of 118 kVp and a tube current of 26 μA was used at constant exposure time of 220 ms per frame. Image acquisition was done with 720 circular projections over 360 ° using a 2 mm thick CZT sensor layer bump bonded to the Medipix3RX readout chip.

5.2.1.4 iDXA

DXA images were obtained from Lunar iDXA (GE Healthcare Lunar, Madison, WI) which uses photon counting based detector technology (Cadmium telluride) that simultaneously counts high and low energy photons. Multi-view image reconstruction

was used to create high resolution images. The BMC was quantified using forearm software by drawing a freeform regions of interest in the vicinity of the implant.

5.3 Results

5.3.1 Qualitative evaluation of bone healing

For qualitative evaluation, the samples were scanned with x-ray, clinical single and dual energy CT, and spectral photon counting CT.

5.3.1.1 Plain x-ray radiograph

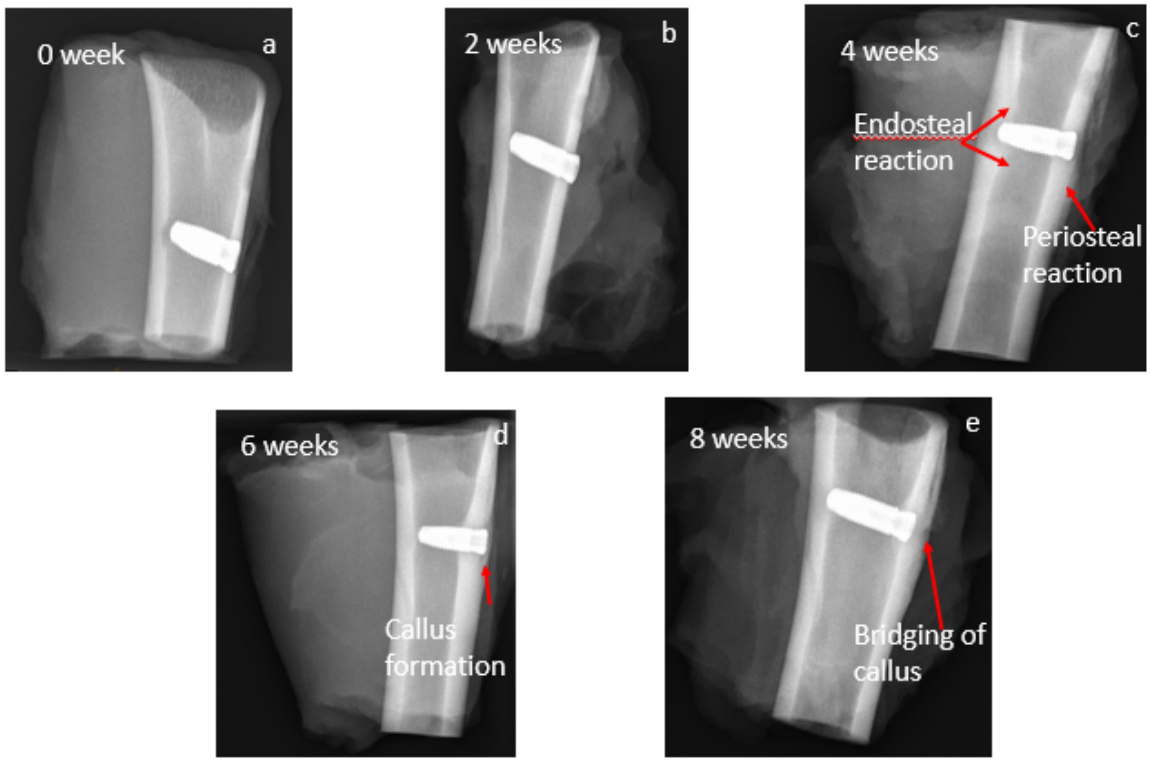

Figure 5.1: Progression of bone healing observed using x-ray radiographs.

The endosteal or periosteal reaction, which is the formation of new bone in response to bone healing due to fracture was identified in the x-ray radiographs at four weeks (Figure 5.1 c). The endosteal reaction was observed due to the piercing of the screw

to the endosteum of the tibia during the surgery. Callus formation was observed at 6 weeks (Figure 5.1 d) and bridging of callus at eight weeks (Figure 5.1 e).

5.3.1.2 Clinical conventional and dual energy CT

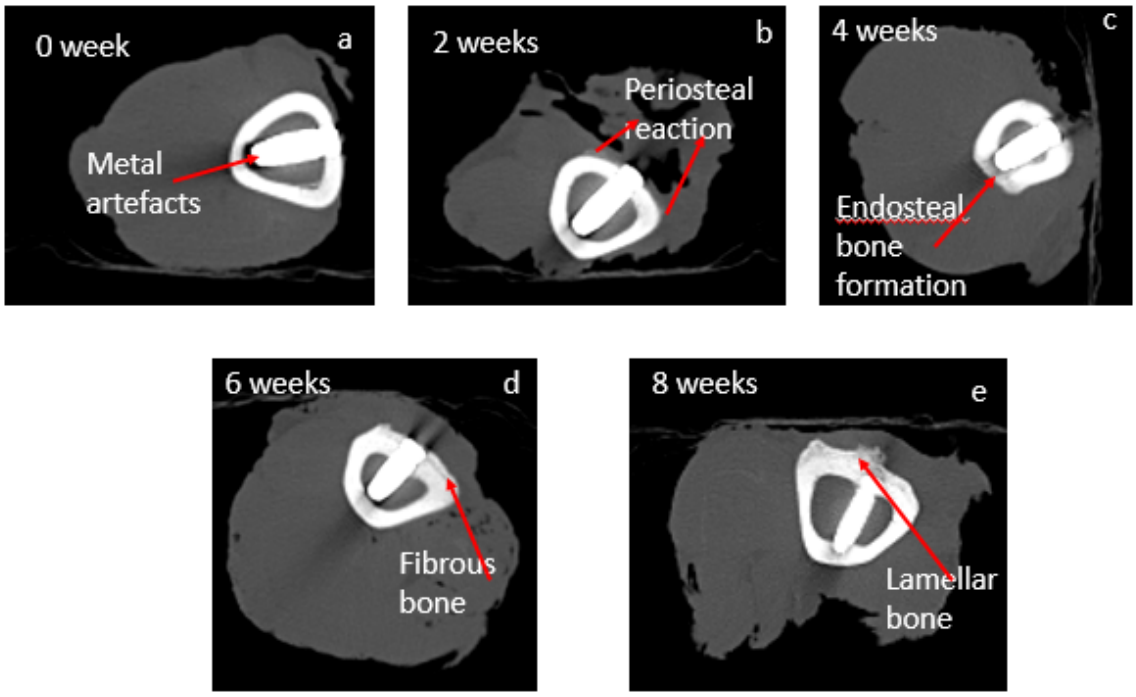

Figure 5.2: Conventional CT images displaying different stages of bone healing at the bone-metal interface.

In conventional CT images, metal artefacts originating from the titanium screw impaired the detection of tissue at the vicinity of the screw (Figure 5.2 a). Periosteal reaction was observed at two weeks (Figure 5.2 b) and fibrous and lamellar bone formation at 6 and 8 weeks respectively (Figure 5.2 d and e).
In Gemstone spectral imaging the artefacts were reduced when compared to conventional CT. The contrast between soft tissue, titanium and bone improved with dual energy CT (Figure 5.3).

5.3.1.3 Spectral photon counting CT

The images obtained from spectral photon counting CT demonstrated periosteal reaction at 2 weeks, endosteal and periosteal bone formation at 4 weeks and the

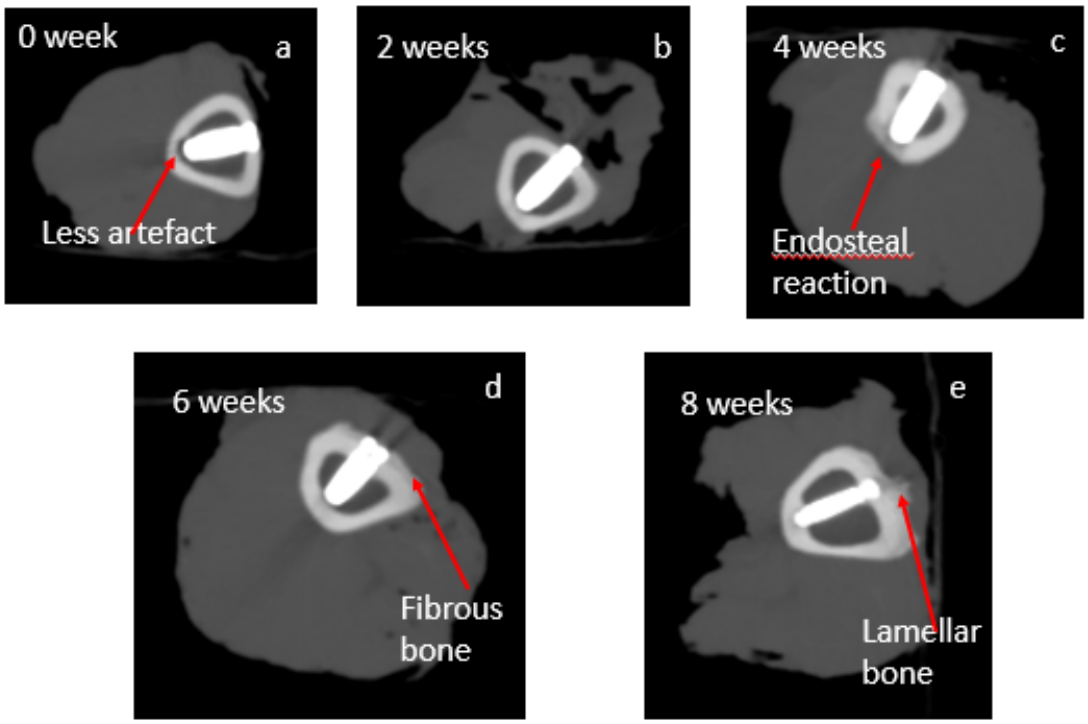

Figure 5.3: Dual energy CT images showing bone healing at the bone-metal interface with reduced artefacts and better contrast compared to single energy CT.

development of fibrous bone and bridging of callus at 6 and 8 weeks respectively (Figure 5.4).

5.3.2 Comparison of images obtained with different imaging modalities

The images obtained from conventional CT suffered from artefacts obscuring the information of the soft issue at the rear end of the screw (Figure 5.5 c). In dual energy CT, even though there were no artefacts the contrast between the metal and bone was very low compared to spectral photon counting CT (Figure 5.5 d). Contrary to our expectations, the images obtained from dual energy CT with metal artefact reduction software displayed a distorted screw (Figure 5.5 e) which could misinterpret the information of the tissue in the proximity of the implant.

Periosteal reaction was not observed in the x-ray obtained at two weeks (Figure 5.6 a). Whereas the images obtained from conventional CT (Figure 5.6 c) and spectral

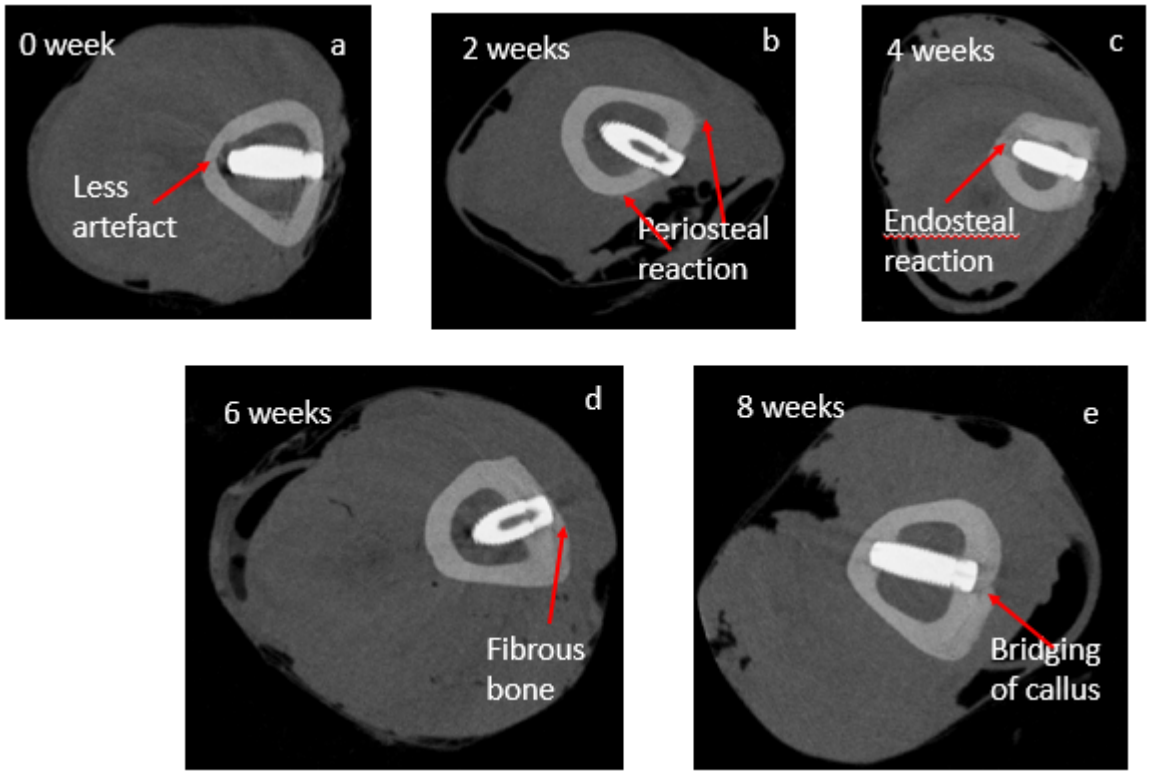

Figure 5.4: Different stages of bone healing observed in images obtained from spectral photon counting CT.

photon counting CT (Figure 5.6 f) displayed periosteal reaction at the far end of the fracture site indicating bone repair.

Periosteal as well as endosteal reaction was observed at the fracture sites from the samples obtained at four weeks after implantation (Figure 5.7). The endosteal bone formation is evident in the images due to the piercing of the rear end of the screw to the cortical bone.

Calcific callus was identified at the fracture site imaged at four weeks. Bone tissue primarily observed at the far end of the fracture gap advanced towards the fracture gap in four weeks (Figure 5.7 f).

Thickening of the cortical bone was observed at six weeks (Figure 5.8). A new bone layer formation was visualised in CT images.

At eight weeks, in the x-ray image the low density periosteal new bone was separable from higher density callus displaying remodelling of the bone at the bone-metal interface (Figure 5.9 a). Periosteal bone formation was observed in all the images

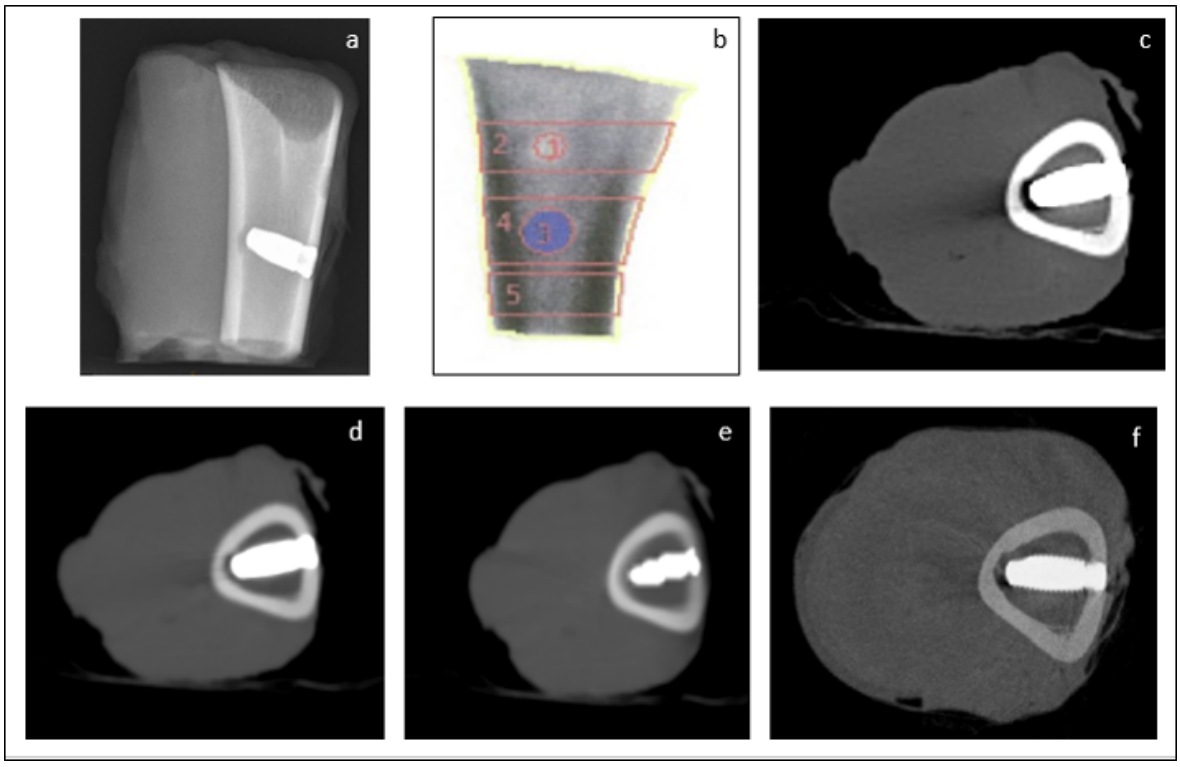

Figure 5.5: Images of the control sheep tibia a) plain radiograph b) iDXA c) conventional CT d) GSI spectral Imaging e) GSI spectral imaging with metal artefact reduction software d) spectral photon counting CT.

obtained eight weeks after implantation (Figure 5.9 f).

5.3.3 Quantification of bone mineral content (BMC)

The region of interest selected for measuring bone mineral content in the vicinity of the implant is highlighted in the iDXA images (Figure 5.10 a). A region of interest 5 mm away from the centre of the screw on either side was selected for determining bone mineral content from spectral CT (Figure 5.10 b). The BMC quantified from iDXA and spectral CT exhibited a linear trend (R^2 =0.72) of increasing bone mineral content till six weeks followed by a decreasing trend at eight weeks. This results demonstrated a similar trend to the blood test for alkaline phosphatase associated with the bone formation. The bone mineral content estimated using iDXA for the control sheep (left tibia) and treated sheep (right tibia at 8 weeks) were less compared to spectral CT measurements. This could be due to the limitation of iDXA in drawing

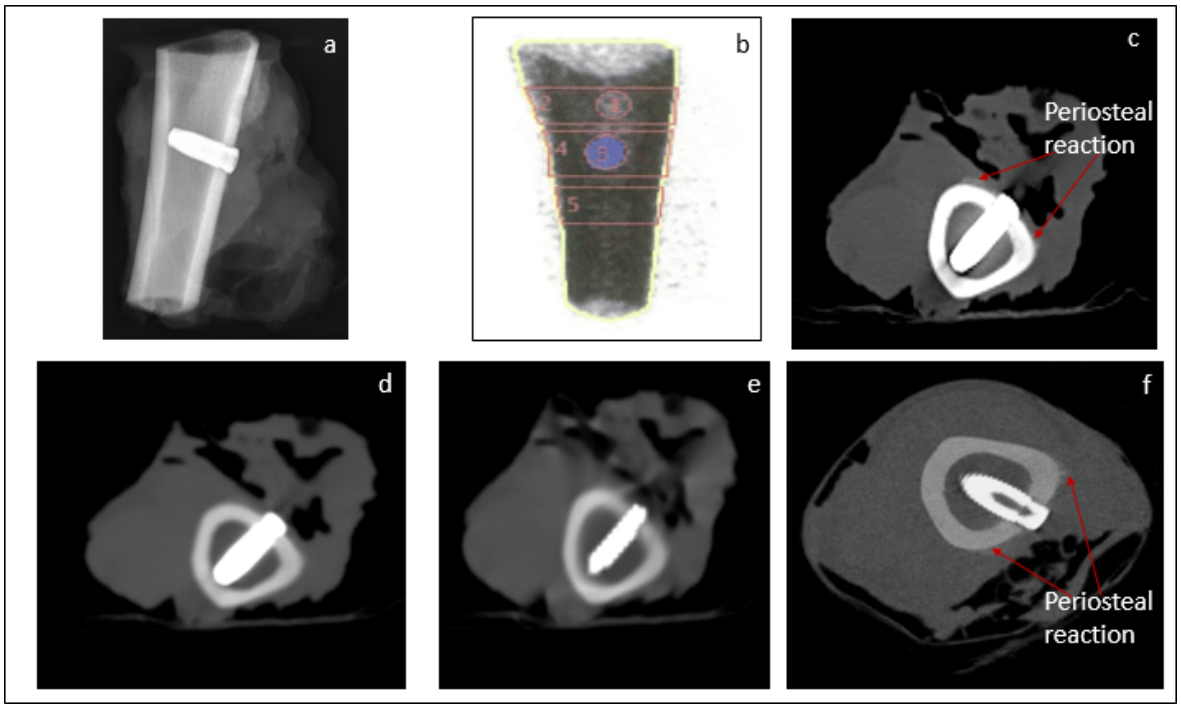

Figure 5.6: Images of the sheep sample obtained after two weeks of implantation a) plain radiograph b) iDXA c) conventional CT d) GSI spectral Imaging e) GSI spectral imaging with metal artefact reduction software d) spectral photon counting CT.

Table 5.1: Comparison of bone mineral content quantified from spectral CT with iDXA

Bone mineral content (g)				
Sheep	**Left tibia**		**Right tibia**	
Time of observation	**spectral CT**	**iDXA**	**spectral CT**	**iDXA**
0 days	**0.07**	**0.05**	**0.10**	**0.15**
2 weeks	**0.08**	**0.17**	**0.14**	**0.20**
4 weeks	**0.17**	**0.24**	**0.22**	**0.32**
6 weeks	**0.21**	**0.32**	**0.27**	**0.21**
8 weeks	**0.17**	**0.17**	**0.20**	**0.17**

manual ROI in the vicinity of the screw. The results obtained from the imaging modalities were compared with alkaline phosphatase test results measuring the level of alkaline phosphatase which aids bone formation. The alkaline phosphatase in the

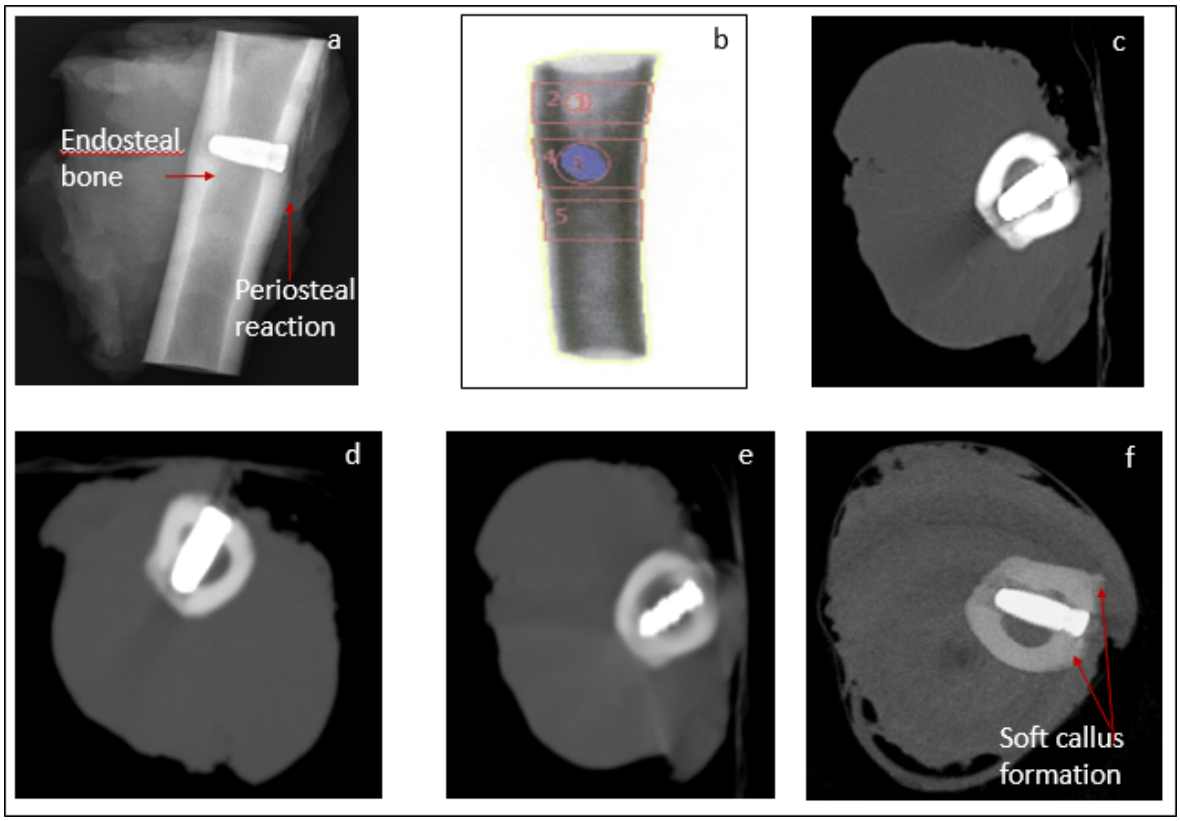

Figure 5.7: Images of the sheep sample after four weeks of implantation a) plain radiograph b) iDXA c) conventional CT d) GSI spectral Imaging e) GSI spectral imaging with MARS d) spectral photon counting CT.

blood samples increased for six weeks followed by a reduction at eight weeks suggesting bone resorption. From the quantitative analysis, the reduced BMC quantified from spectral CT and iDXA also indicated bone resorption at eight weeks.

5.4 Discussion

The bone-implant interface is challenging to visualise even with highly sophisticated imaging modalities. Despite ongoing preclinical and clinical studies, the process of bone remodelling in the vicinity of the implant is not yet completely understood Pearce *et al.* (2007). Hence a reliable imaging tool to evaluate the osseointegration at the bone-metal interface is essential to understand bone healing. From the qualitative evaluation of the images, it is clear that the spectral CT images displayed bone-metal interface with high contrast between bone, soft tissue and the titanium screw and fewer artefacts. Also,

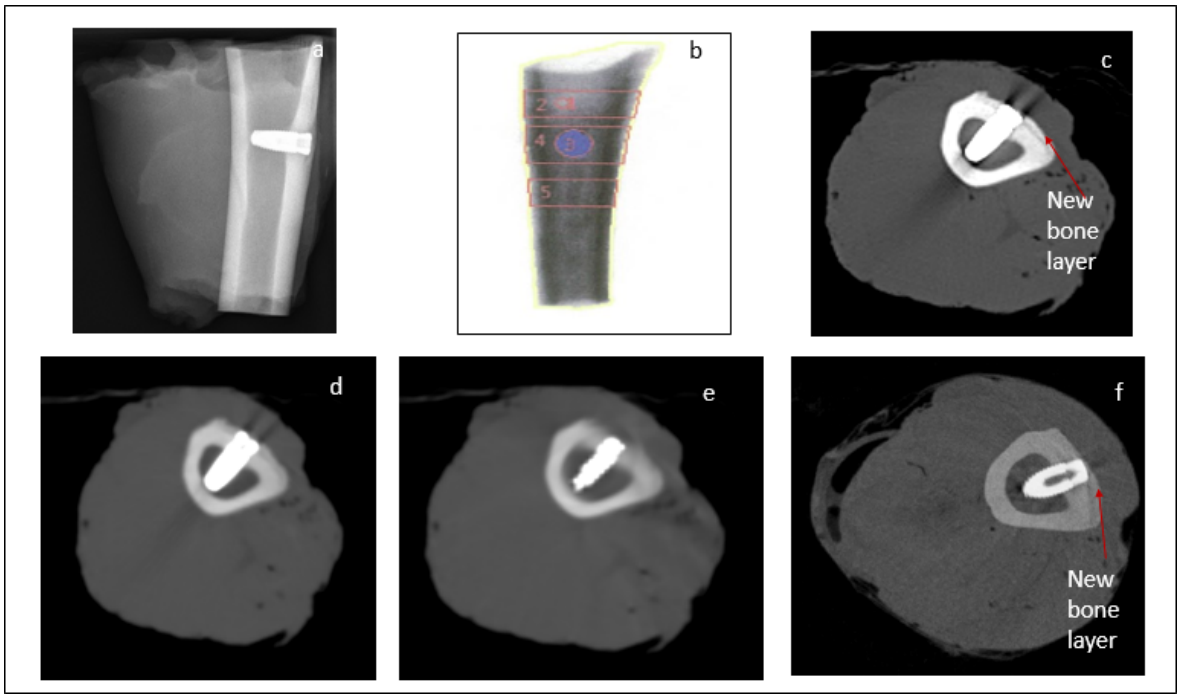

Figure 5.8: Images of the sheep sample at six weeks of implantation a) plain radiograph b) iDXA c) conventional CT d) GSI spectral Imaging e) GSI spectral imaging with metal artefact reduction software d) spectral photon counting CT.

an earlier detection of periosteal reaction at two weeks was observed with spectral CT. Single energy CT also demonstrated an earlier detection of periosteal reaction but the lower contrast between the bone and metal, and the artefacts reduced the reliability in predicting the bone healing at the interface. The dual energy CT images were devoid of artefacts but poor contrast resolution at the bone-metal interface is a disadvantage for assessing bone healing. The images reconstructed using metal artefact reduction software depends on the prosthesis material. GSI metal artefact reduction software is more effective with dense metal prostheses such as stainless steel than the titanium prosthesis Douglas-Akinwande *et al.* (2006). In the present study, 5 mm from the centre of the screw and outwards was selected to determine BMC at the bone-metal interface, indicating close contact between the bone and titanium screw, and suggesting fracture healing. The BMC quantified from iDXA and spectral photon counting CT displayed an increasing trend to six weeks indicating bone formation, and reduced at eight weeks suggesting bone resorption. Similar results were reported previously by Chen *et al.* (2015) in an immature rabbit model, where the remodelling reached a peak at 6 weeks.

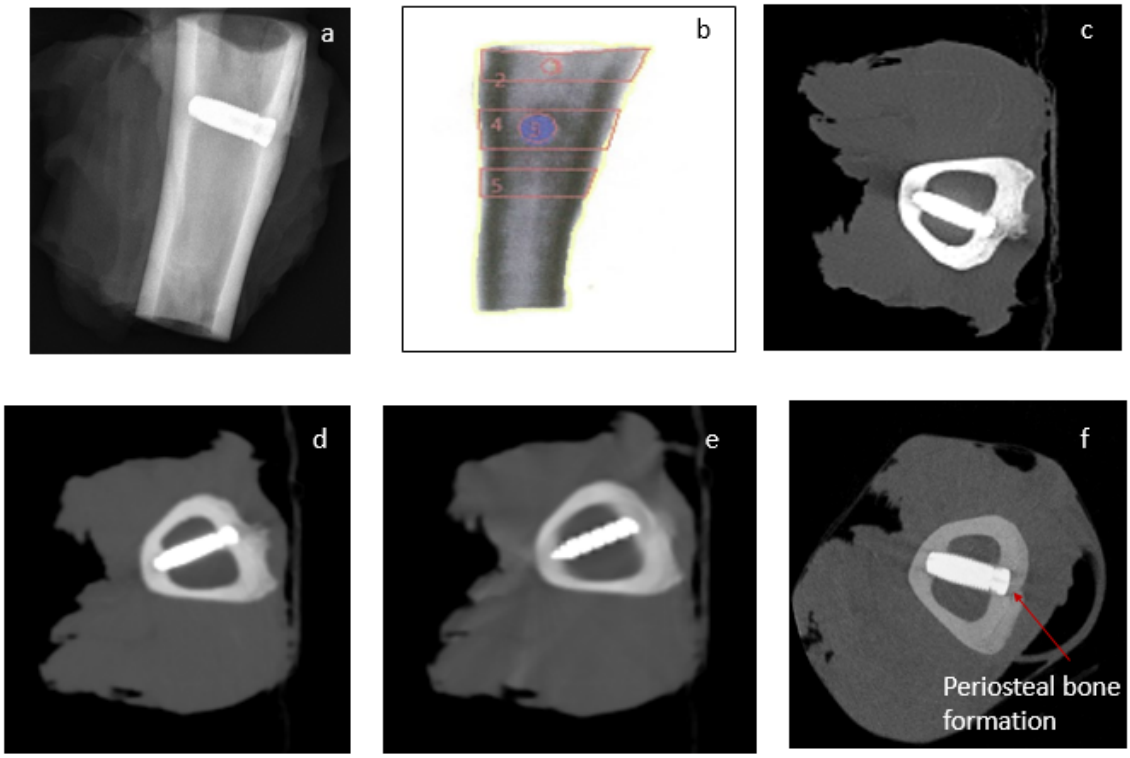

Figure 5.9: Images of the sheep sample at eight weeks of implantation a) x-ray b) iDXA c) conventional CT d) GSI spectral Imaging e) GSI spectral imaging with MARS d) spectral photon counting CT.

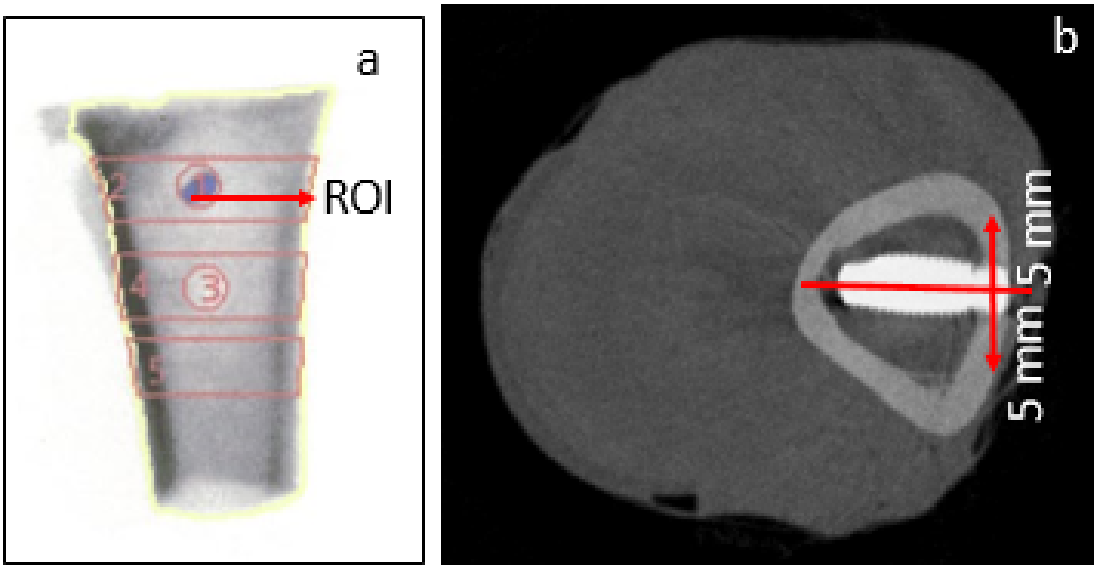

Figure 5.10: Region of interest selected for determining bone mineral content a. iDXA b. Spectral photon counting CT

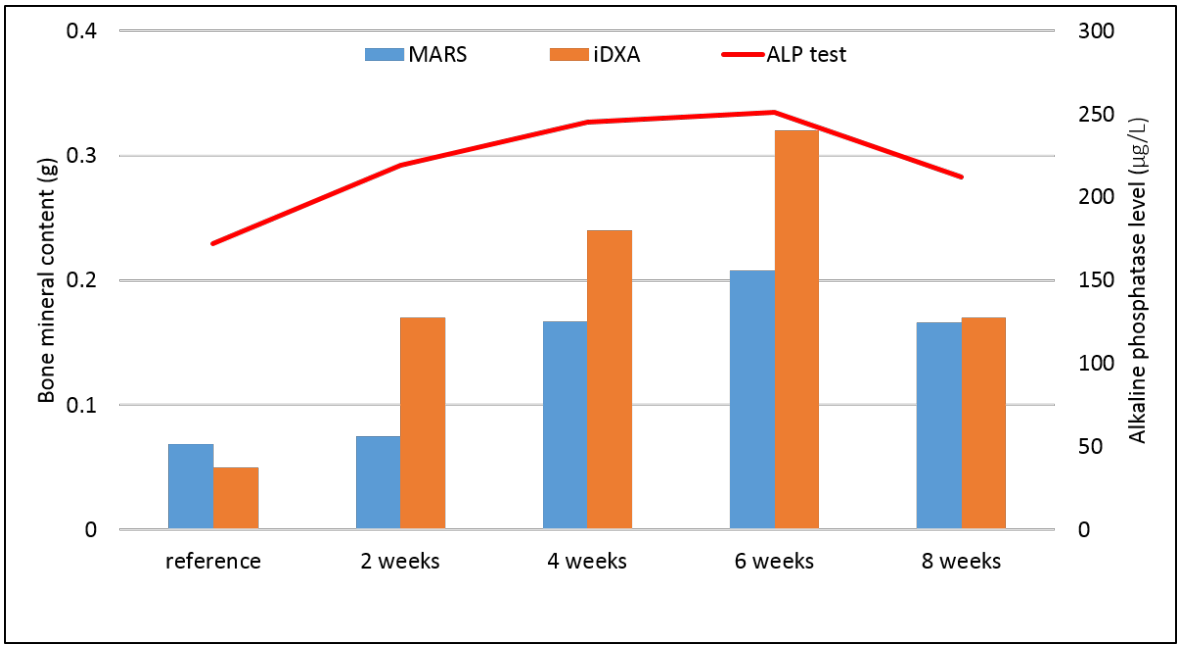

Figure 5.11: Bone mineral content measured from left tibia using spectral CT and iDXA displayed an increasing BMC till six weeks followed by a reduction in the BMC at eight weeks. The results were compared with alkaline phosphastase test which also exhibited an increased level of alkaline phosphatase till six weeks followed by a reduction at eight weeks.

The ALP test also displayed an increasing level of alkaline phosphatase to six weeks which reduced after eight weeks. However the BMC quantified from iDXA and spectral CT are difficult to compare as there is no unified reference. One of the limitations of the study is that the studies were performed on a sheep model and will have significant differences when it is extrapolated to a clinical situation due to differences between the species. Another limitation of the study was the small sample size (n=11). One of the control sheep lacked a metal implant during sample extraction. However, the BMC content quantified from the left and right hind legs of the sheep reduces the number of sheep needed to answer the research question meaningfully. Another limitation of this study is that the histological analysis of osseointegration was not performed. Another limitation of the study is that even though an abnormal level of ALP indicates bone healing many other factors can influence ALP concentrations Sousa *et al.* (2014). In the present study, the sheep samples lacked any trabecular region which would have been a clear indicator of bone remodelling at the bone-metal interface. Future studies on more sheep samples with trabecular region will enable quantification of trabecular

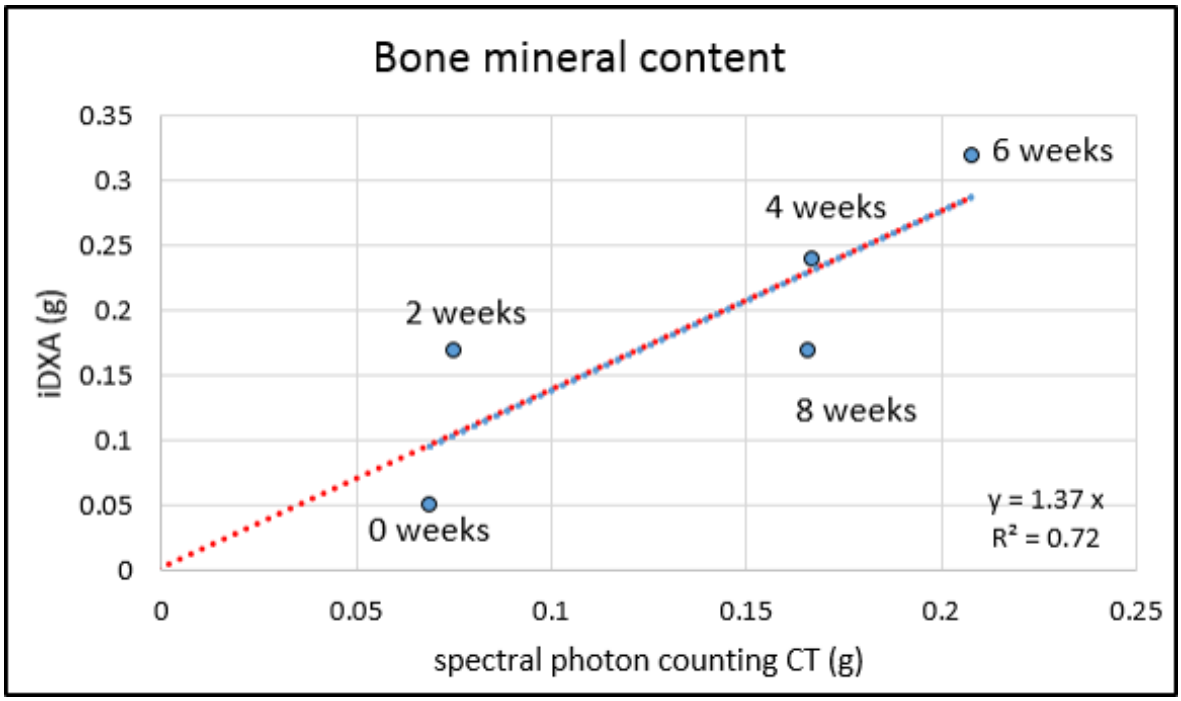

Figure 5.12: Linearity response of BMC quantified from spectral CT and iDXA. The coefficient of determination R^2= 0.72 depicts stronger correlation between the BMC measurements obtained from spectral CT and iDXA.

density, thickness and spacing at the bone-metal interface during fracture healing.

5.5 Conclusion

Spectral photon counting CT is a non-invasive three dimensional imaging modality to assess osseointegration at the bone-metal interface. The high spatial resolution as well as the reduced artefacts at the bone-metal interface enables earlier detection of bone healing at the bone-metal interface. The BMC quantified from spectral photon counting CT demonstrated increased mineralisation of bone to six weeks. The layers of the newly formed bone were clearly visualised in spectral CT images. Spectral photon counting CT can be used as a potential tool to assess early bone healing at the bone-metal interface.

5.6 Dissemination of the research

The methods and results discussed in this chapter have led to a manuscript (under preparation) and an oral presentation.

Amma M. R et al Assessment of bone healing at the bone-metal interface using spectral photon counting CT (Under preparation)

This manuscript describes the advantages of using spectral photon counting CT scanner for assessing early fracture healing at the bone-metal interface. The qualitative and quantitative evaluation of early fracture healing at the bone-metal interface was compared with plain radiographs, iDXA and clinical single and dual energy CT. I am the primary author of this manuscript.

This work was done in collaboration with the Lincoln University (AEC 2018-31). The surgical preparation of the sheep were performed by Dr.E Peter Walker. The samples were imaged with different imaging modalities to assess bone healing. I scanned the samples using spectral photon counting CT. I also contributed to the data analysis and interpretation of the results. The methods discussed in this chapter led to an oral presentation

Amma, M. R. Bone implant imaging. MARS Spectral CT Workshop held at Christchurch, New Zealand, November 2018.

5.7 Summary

• Spectral photon counting CT is a potential tool to assess bone healing.

• Fewer artefacts and high contrast in the images makes spectral CT a superior tool in evaluating bone-metal interface compared to clinical single and dual energy CT.

• The high spatial resolution of spectral CT and its ability to capture soft tissue contrast at the vicinity of the implant might enable clinicians to assess fracture healing and osseointegration.

Chapter 6

Crystal arthritis-diagnosis and monitoring

This chapter describes the osteoarthritis (OA) imaging capabilities of the MARS photon counting spectral CT scanner. The purpose of this chapter is to investigate whether the multiple energy binning capacity of photon counting spectral CT could not only differentiate monosodium urate (MSU) from calcium crystals, but also distinguish different calcium crystal types despite slight variations in their x-ray attenuation properties. Currently, there is no imaging modality capable of non-invasively identifying one calcium crystal type from another in crystal induced arthropathies. We aimed to specifically identify calcium pyrophosphate dihydrate (CPPD) in a human knee meniscus and distinguish it from calcium hydroxyapatite (HA) using MARS spectral photon counting CT. Since calcium pyrophosphate dihydrate (CPPD) is clinically heterogeneous form of arthritis, accurate diagnosis of CPPD will facilitate capability of non-invasive diagnosis. It is evident that advances in imaging for discriminating crystal and non-crystal arthritis will increase diagnostic accuracy required for deciding treatment strategy. The work presented in this chapter has already been published in which I was a co-author Stamp *et al.* (2019); Aamir *et al.* (2018)].

6.1 Introduction

Osteoarthritis (OA) is the most common form of arthritis which predominantly affect elderly population. With the increasingly aging population in New Zealand, the incidence of OA affecting hip and knee resulting in total hip replacement (THR) and knee arthroplasty (TKA) is expected to increase in the next 10 to 20 years Hooper *et al.* (2014). Calcium containing crystals are found in 60% of synovial fluids collected from osteoarthritic patients undergoing TKA Viriyavejkul *et al.* (2007) . Differentiating crystal type, whether monosodiumurate (MSU) or one of the calcium crystal types is a clinical challenge particularly in musculoskeletal imaging, cardiovascular, genitourinary, and breast Rosenthal (2007); Morgan *et al.* (2005). Crystal-induced arthropathies frequently require joint aspiration Pascual and Sivera (2011) or biopsy and to identify crystals using x-ray diffraction or polarised light microscopy. Non-invasive characterisation of crystals by imaging tissues is desirable as it would facilitate faster detection of articular crystals.

In conventional radiology, plain x-ray radiograph have poor sensitivity and may miss calcium crystals due to its small size and concentrations Jacques *et al.* (2017). In MRI, calcifications are not well visualised in articular tissues due to poor sensitivity and specificity Dirim *et al.* (2013). Ultrasound imaging is an ideal tool to diagnose and monitor rheumatic diseases including gout Codreanu and Enache (2015) but it can be challenging to distinguish gout from pseudogout Löffler *et al.* (2015). Dual energy CT (DECT) has shown some promise in crystal detection at high concentrations. DECT is relatively accurate in distinguishing monosodium urate (MSU) Desai *et al.* (2011) from deposits of calcium pyrophosphate dihydrate (CPPD) and calcium hydroxyapatite (HA). MARS is an emerging photon counting spectral CT which allows characterisation and quantification of materials without loss of spatial resolution by utilising data collected from multiple narrow energy bins Anderson *et al.* (2010). The attenuation of material is based upon the effective atomic mass, and the material density. The aim of this chapter is to demonstrate that MARS photon counting spectral CT could differentiate calcium crystal types despite slight variations in their x-ray attenuation

properties (Figure 6.1).

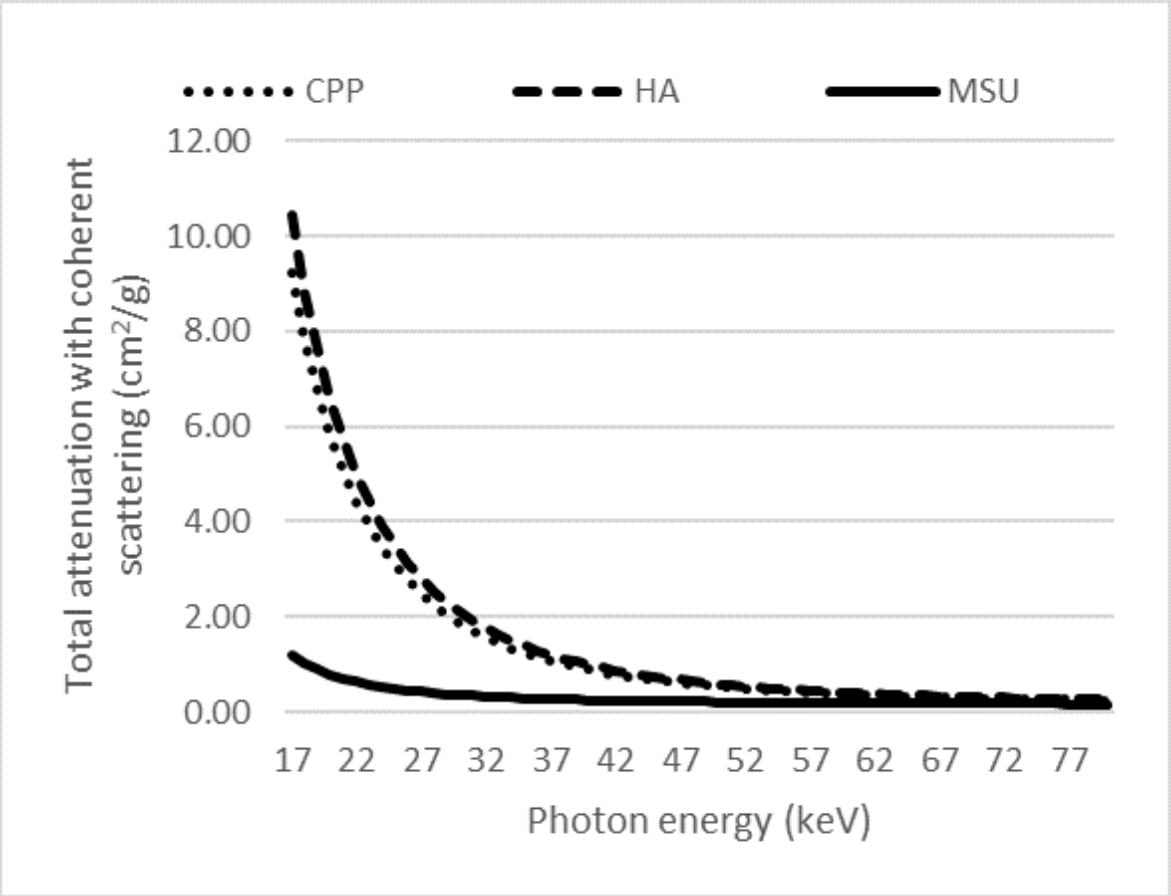

Figure 6.1: Simulated total attenuation of CPPD, HA and MSU depending on the photon energy range of 17-80 keV, simulated using NIST XCOM. This figure displays similar attenuation properties for CPPD and HA, which in turn points towards the difficulty in separating these crystals.

6.2 Methods and materials

Three different rods with known concentrations of MSU (200, 400, 600 mg/cm^3), CPPD (50, 100, 200 mg/cm^3) and HA (50, 100, 200 mg/cm^3) were obtained from Computerised Imaging Reference Systems, Inc (CIRS). We used a 25-mm-diameter PMMA phantom with multiple 6 mm diameter inserts containing various concentrations of MSU, CPPD and HA as shown in Figure 6.2 a. The calibration phantom was scanned using parameters set on the MARS scanner controller software as in Table 6.1. After data acquisition the projection images in DICOM format were

transferred to PACS where automated image processing was performed. The spectral data was reconstructed using a customised polychromatic iterative reconstruction algorithm. Histograms of linear attenuation coefficients were plotted for each energy bin and crystal type. This shows the potential separability of the materials using a pairwise comparison of specificity and sensitivity through a receiver operating characteristic (ROC) curve. The area under the ROC curve (AUC) was determined and used as the figure of merit to distinguish two crystals. The higher the AUC value, the easier the discrimination task. The differentiation between any two crystal concentrations was considered successful if AUC > 0.95 Viry *et al.* (2018). A calcified osteoarthritic medial meniscus was excised at the time of total knee replacement with institutional human ethics approval. Ethics approval was obtained from the University of Otago Human Health Ethics Committee (URB/07/02/001), and from the Institutional Ethics Committee (CER-VD) of Lausanne University Hospital. A calibration phantom containing known concentrations of CPPD and HA (Figure 6.2 a) and a whole meniscus (Figure 6.2 b) were scanned using energy thresholds: 20, 30, 40 and 50 keV at 80 kVp. MD was applied to the imaging data to distinguish the

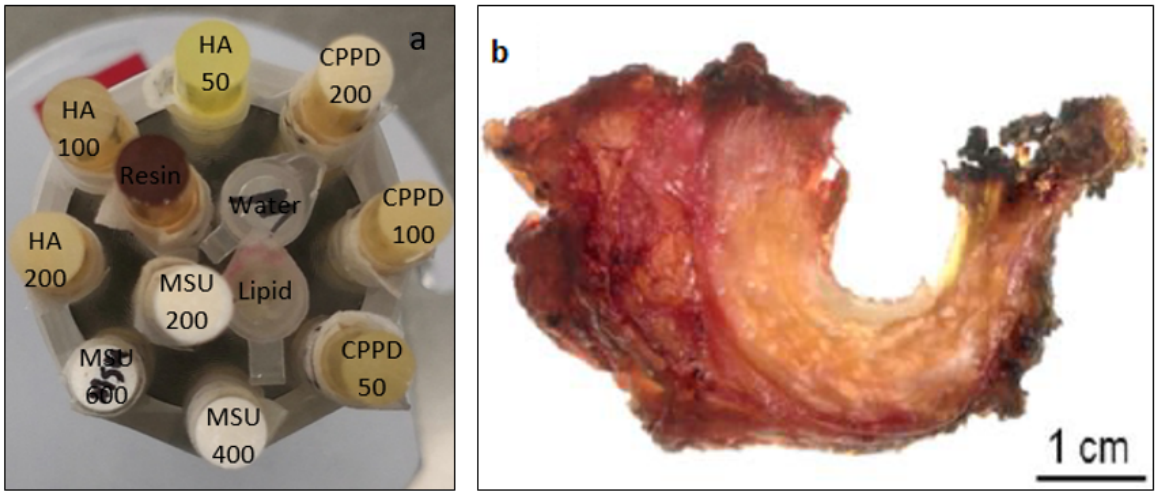

Figure 6.2: (a)PMMA phantom with calibration vials of various known concentrations of CPPD, HA and MSU (b) Excised knee meniscus with crystal deposits.

two calcium phosphate crystal types. High resolution material images of the meniscus were generated using MARS Vision. For validation of the crystal type, crystals were scraped from the meniscus and examined by x-ray diffraction (XRD) and polarised

light microscopy. For XRD, samples were mounted on a nylon loop in a minimum amount of perfluorinated oil at 298 K. Data was collected on an Agilent SuperNova (Dual, copper at zero, Atlas) diffractometer (Agilent Technologies, Yarnton, UK). The images were integrated using CrysAlisPro (1.171.38.43 (Rigaku Oxford Diffraction, 2015)) and the background was manually subtracted using Origin 8.6001 Stamp *et al.* (2019).

Table 6.1: Scanning protocol for crystal differentiation

Protocol	**Crystal protocol @ 80 kVp**
Filter	**2mm Al (extrinsic) +1.8 mm Al (intrinsic)**
Tube current	**29 uA**
Exposure time	**220 ms**
Voxel size	**90 um (isotropic)**

6.3 Results

6.3.1 Histogram analysis

Histogram plots of linear attenuation coefficients for each energy bin and lower concentrations (HA 50 mg/cm^3, CPPD 50 mg/cm^3, MSU 200 mg/cm^3) of different crystals showed graphically that HA and CPPD, and CPPD and MSU can be differentiated at 20-30 keV, and that their overlapping increases with higher energy bins (Figure 6.3). The histogram plots revealed that there is misidentification between lower concentrations of HA and MSU even at lower energy bins.

6.3.2 ROC curves

ROC curves were plotted for the two combinations of CPPD and HA, and CPPD and MSU as shown in Figure 6.4. For each material combination, AUC was plotted as a function of the energy bins. AUC values decrease for the higher energy bins which shows that different crystal compositions cannot be distinguished at higher

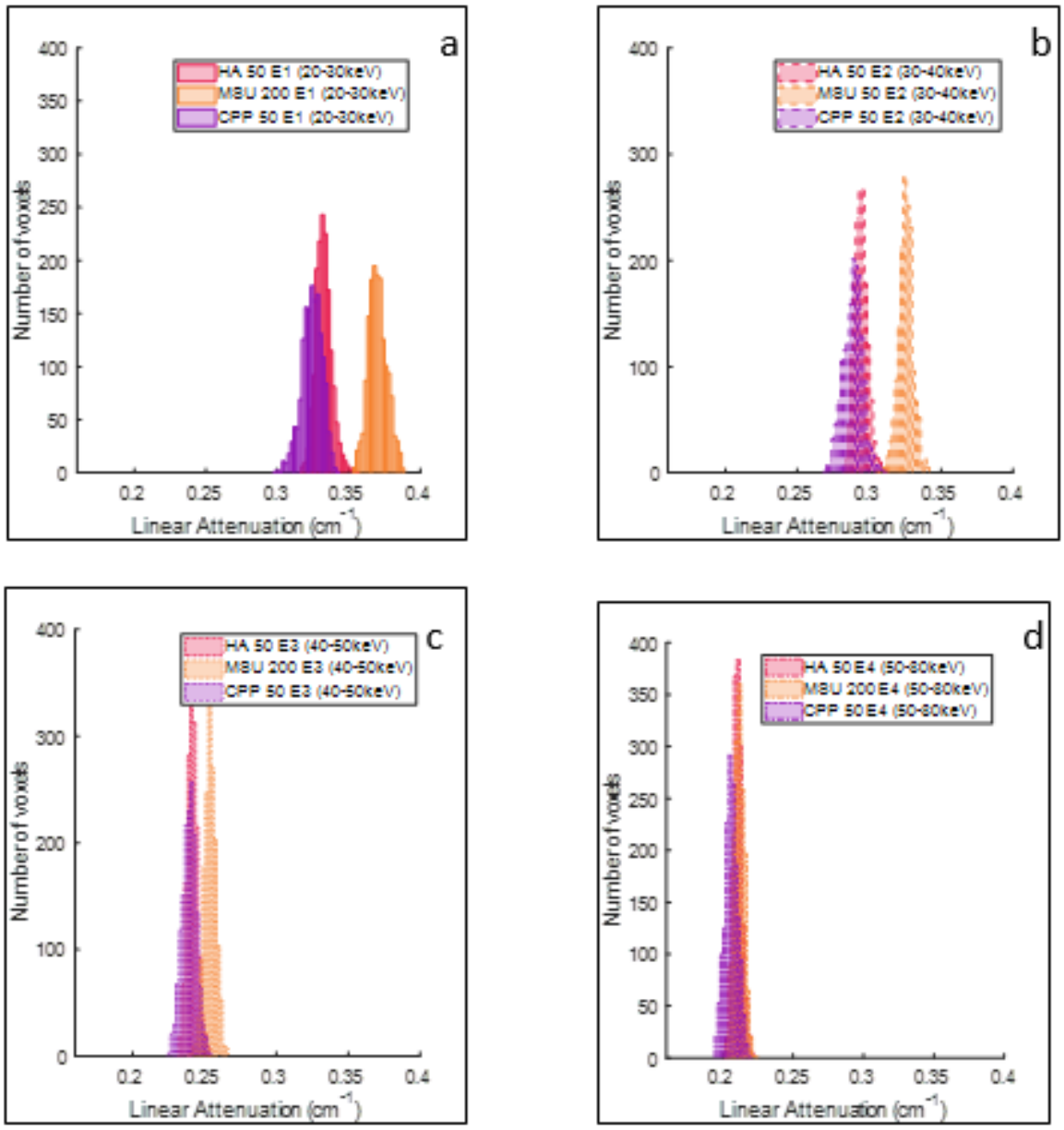

Figure 6.3: Histogram plots for lower concentrations of HA, CPPD, MSU at (a) 20-30 keV (b) 30-40 keV (c) 40-50 keV (d) 50-80 keV. These plots demonstrate that even lower concentrations of pairs of MSU and CPPD, CPPD and HA, and MSU and HA can be differentiated at low energy bins.

energy bins (Figure 6.5). For pairwise comparison, the AUC value is maximum for the lowest energy range (20-30 keV). The AUC values illustrates that there is an excellent discrimination between different crystal concentrations in the first two energy bins. The discrimination between crystal concentrations increases as the concentration increases.

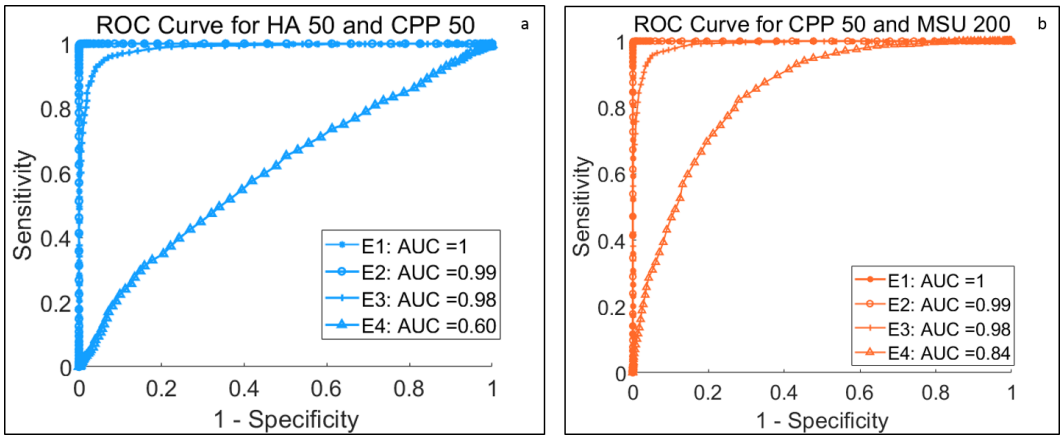

Figure 6.4: ROC curves for pairwise analysis of (a) HA 50 and CPPD 50 (b) CPPD 50 and MSU 200 at energy levels E1 (20-30 keV), E2 (30-40 keV), E3 (40-50 keV), E4 (50-80 keV)

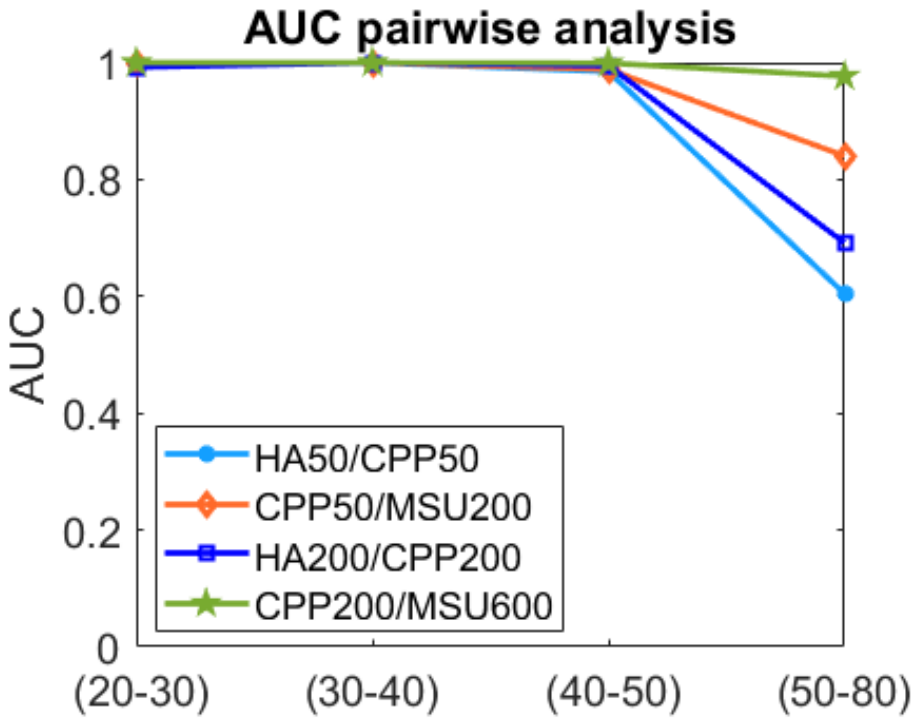

Figure 6.5: Area under curve displaying excellent differentiation between various crystal types at lower energy bins and with increased concentrations

6.3.3 Material discrimination

The mass attenuation values obtained from the calibration phantom were applied for the MD of an excised knee meniscus. MD was applied to the meniscus to separate water, CPPD, and HA. The MD image of the meniscus and the quantified materials

are shown in the Figure 6.6.

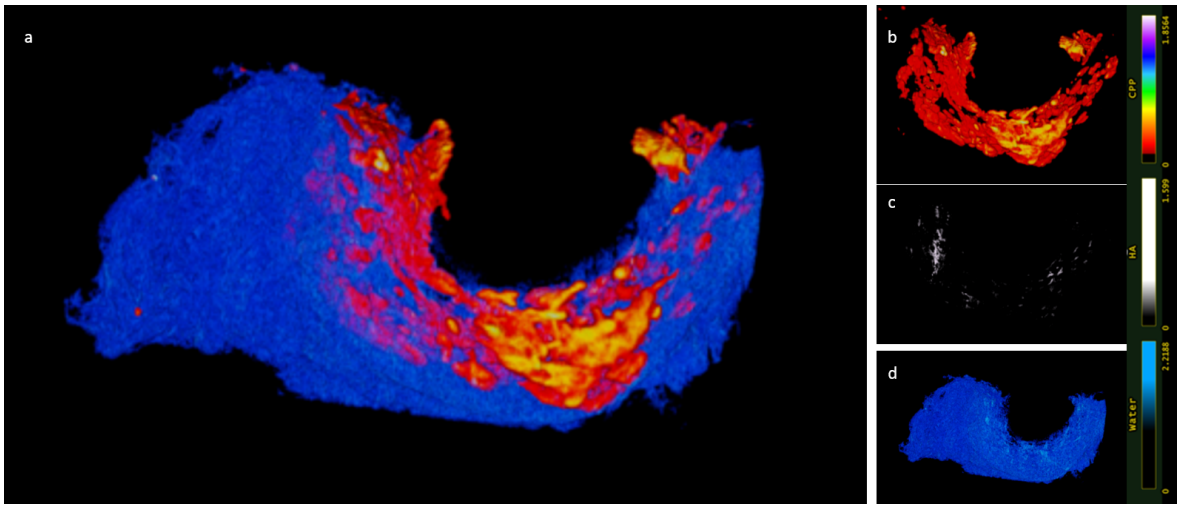

Figure 6.6: (a)MD image of excised knee meniscus displaying predominance of CPPD crystal deposits (blue-water like, red to yellow- CPPD like, and white- HA like) (b) CPPD like material (c) HA-like material (d) water-like material

6.3.4 Validation

The gold standard for the diagnosis of CPPD crystals are expensive research tools such as Fourier Transform Infrared (FTIR) spectroscopy or x-ray diffraction. The commonly used clinical tool is x-ray, which confirms CPPD disease by linear calcification of cartilage. For validation of CPPD crystals, x-ray diffraction and polarised microscopy was used.

6.3.4.1 Plain x-ray

Pre-operative plain x-ray of the right knee revealed pseudogout (Figure 6.7 a), due to the presence of CPPD. A plain x-ray of the excised knee meniscus shows the crystal deposit (Figure 6.7 b), but is unable to distinguish different crystal types which is clinically relevant for administering treatment. MARS photon counting spectral CT was able to distinguish CPPD and HA in the excised knee meniscus (Figure 6.6 b and c).

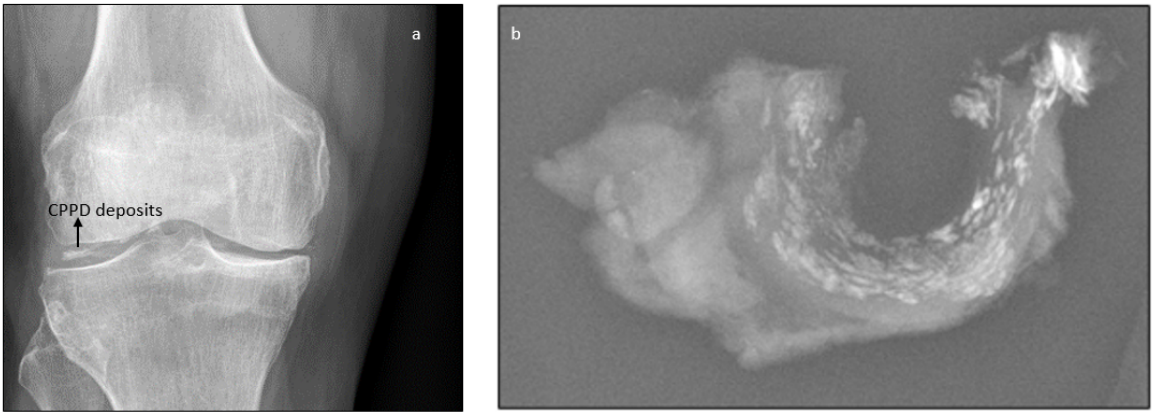

Figure 6.7: (a) Preoperative plain x-ray of the right knee revealing crystal deposit (b) plain x-ray of the excised meniscus confirming calcifications within the meniscus.

6.3.4.2 X-ray Diffraction (XRD)

XRD is a rapid analytical technique widely used for the identification of crystalline samples MacMullan *et al.* (2011). X-rays are passed through prepared powdered sample and the intensity of diffracted x-rays are continuously recorded as the sample and detector rotates through angle 2θ. The diffracted x-rays are detected, processed and counted. The diffraction peaks are converted into d-spacing using Bragg's law $n\lambda = 2d\text{Sin}\theta$. As each mineral has unique d-spacing, conversion of diffraction peaks to d-spacing allows accurate identification of any crystals present. The diffraction pattern obtained from the sample was assigned as a mixture of monoclinic and triclinic CPP dihydrate (m-CPPD and t-CPPD). There were no significant peaks to indicate the presence of HA (Figure 6.8 a).

6.3.4.3 Polarised light microscopy

Polarised light microscopy is an illumination technique commonly used on birefringent samples where the polarised light interacts with the sample generating a contrast with background. Polarised light microscopy was used to identify the presence of positively birefringent rhomboid shaped CPPD crystals (Figure 6.8 b).

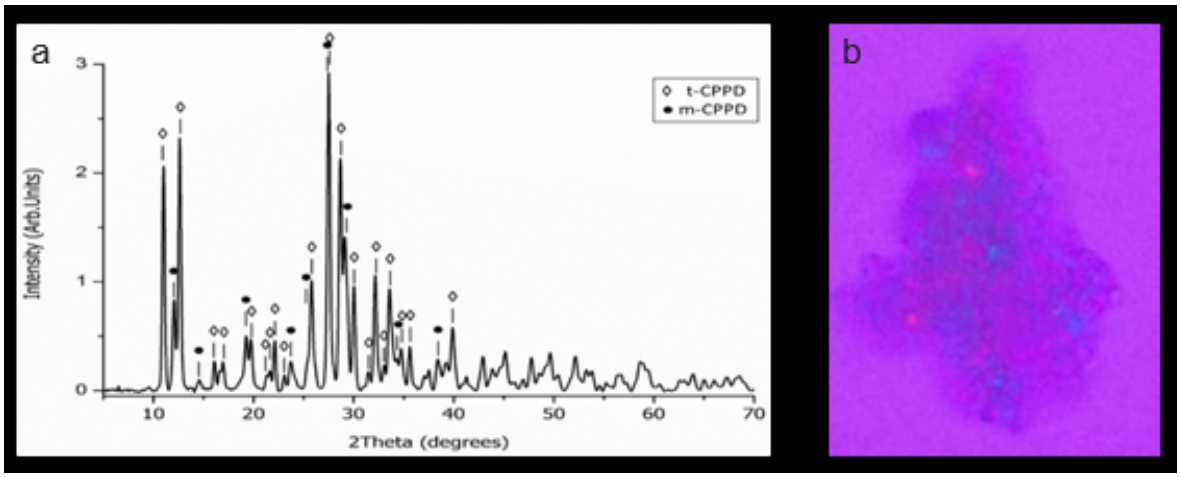

Figure 6.8: (a) XRD of the crystal scrapings confirming the presence of weakly positively birefringent CPPD crystals with a diffraction pattern assigned as a mixture of monoclinic and triclinic CPPD (b) Polarised light microscopy displays positively birefringent rhomboid shaped CPPD crystals.

6.4 Discussion

MARS spectral photon counting CT images showed a predominance of CPPD crystals in the calcified meniscus. In parts of the meniscus, there was a mixture of HA and CPPD. Identification of the type of the crystal will increase diagnostic accuracy required for deciding treatment strategy. MARS images of the meniscus were validated by polarised light microscopy and XRD of the crystal scrapings. While XRD and polarised light microscopy can be used to validate presence of CPPD crystals, it is more difficult to validate HA which cannot be identified using these techniques. As an alternate validation method, we have shown that MARS photon counting spectral CT, especially when using lower energy bins such as 20-30 keV, can differentiate clinically relevant concentrations of MSU and CPPD, and HA and CPPD with excellent diagnostic accuracy. Previous studies were performed with CPPD and MSU crystals dissolved in agar solution. Later, CPPD, MSU and HA calibration rods were obtained from CIRS. For pairwise analysis, CPPD 100 mg/ml and HA 100 mg/ml concentrations were not considered. There was an error in linear attenuation values of HA 100/CPPD 100 rods, leading to the conclusion that there was a manufacturing defect for one of those vials. MARS photon counting spectral CT can identify and characterise CPPD crystals within a human knee meniscus and distinguish them from HA. In this study

only one biological specimen was scanned as a proof of concept. Further optimisation of the protocol and refinement of the material decomposition algorithm will improve the differentiability of crystals inducing arthritis. Future studies will involve scanning of more menisci and tibial plateau to confirm the findings. The scans of nine osteoarthritic knee samples and tibial plateau obtained from Lausanne and stored in the freezer at the CARA facility, will be performed by a subsequent PhD student. The accurate discrimination of the crystal types could improve the diagnosis of microcalcification types found in the breast, detecting the vulnerability of atherosclerotic plaques, and in the treatment and management of urinary stone diseases Kirkbride *et al.* (2017).

6.5 Conclusion

MARS spectral photon counting CT can distinguish different crystal types inducing arthritis non-invasively. Spectral CT has the potential to diagnose and monitor crystal induced arthritis. Pairwise analysis of different crystals showed improved distinction at higher crystal concentrations and in lower energy bins. Photon counting spectral CT can distinguish different clinically relevant concentrations of CPPD and HA, and CPPD and MSU, confidently (AUC $>$ 0.95) in the first three energy bins.

6.6 Dissemination of this research

The methods and results from this chapter have led to the following journal articles and conference proceedings, and the supervision of a summer student and an intern student.

1. Stamp, L. K., Anderson, N. G., Becce, F., **Rajeswari, M.**, Polson, M., Guyen, O., Viry,A., Choi, C., Kirkbride, T. E., and Raja, A. Y. (2019). Clinical utility of multi-energy spectral photon-counting ct in crystal arthritis. Arthritis and Rheumatology (Journal article).

   This article discusses the clinical utility of MARS scanner in differentiating gout and pseudogout. The image of the gouty finger in this article was the **cover page of the journal** published on July 2019.

2. Becce F, Viry, Anais, K Stamp, Lisa, Pascart Tristan, Francois Jean, Sikiru A Adebileje, Steven D Alexander, **Maya R Amma**, Marzieh Anjomrouz et.al. Winds of change in imaging of calcium crystal deposition diseases. Joint Bone Spine (May 2019), https://doi.org/10.1016/j.jbspin.2019.04.005 (Journal article).
   This article emphasises the potential of MARS CT in the diagnosis of crystal arthritis and to provide a better understanding and deeper insights into the possibly pathogenic role that various calcium crystals play within joints in vivo, including in osteoarthritis.

3. R.Aamir, A.Viry, T.E.Kirkbride, **M. Rajeswari**, L.Stamp, M.Polson, O.Guyen, F. Becce, N. Anderson, Characterisation of calcium crystal types in osteoarthritic meniscus at spectral photon-counting CT, Proceedings of European Society of Radiology (ESR) 2018, http://dx.doi.org/10.1594/ecr2018/C-1731 (Conference proceedings).
   This proceeding shows that MARS spectral CT can non-invasively differentiate calcium hydroxyapatite and calcium pyrophosphate crystals present in the meniscus.

This study was done in collaboration with Lausanne University, Switzerland. The knee meniscus samples were provided by Lausanne University Hospital, Switzerland. I collaborated with Anais Viry from Lausanne University to scan calibration phantoms and meniscus samples. I also contributed to the data analysis by performing material decomposition and post processing of meniscus images. I supervised Bradon Noordanus (Summer student, University of Canterbury) for experimental planning and analysis of the newly obtained calibration phantoms to ensure the reproducibility and repeatability of the scans. I also supervised Joosje de Bakker (intern student, University of Twente, Netherland) in optimising the existing protocol and improving the material decomposition algorithm. This research also led to one oral and two poster presentations.

1. **Amma, M. R**. Imaging of crystal induced arthritis using MARS spectral CT. 3 Minute thesis competition held at the University of Otago, Christchurch, New Zealand, July 2018.

2. R.Aamir, A.Viry, T.E.Kirkbride, **Amma, M. R**, L.Stamp, M.Polson, O.Guyen, F. Becce, N. Anderson. Characterisation of calcium crystal types in osteoarthritic meniscus at spectral photon-counting CT. T.E Kirkbride presented ePoster at European Society of Radiology (ESR) held at Vienna from February 28- March 4, 2018.

3. Lisa K. Stamp, Nigel Anderson, Fabio Becce, **Amma, M. R**, Matthew Polson, Olivier Guyen, Anais Viry, Chloe Choi, Tracy Kirkbride and Aamir Raja. Clinical Utility of a Multi-Energy Spectral CT in Crystal Arthritis. Lisa K Stamp presented the poster at ACR/ARHP Annual meeting held on 23rd October, Chicago, 2018.

6.7 Summary

• MARS photon counting spectral CT can distinguish different crystal types inducing arthritis non-invasively.

• The results obtained from MARS CT were partially validated against XRD and polarised light microscopy.

• Optimisation of protocol and material decomposition algorithms can further improve the accuracy of diagnosis of different crystal types inducing arthritis.

Chapter 7

Conclusion

This chapter provides the summary of the results discussed in this thesis, conclusion of the research and the suggestions for future work.

7.1 Summary

Chapter 1 provided a brief explanation of the working of MARS spectral photon counting CT and its unique features which make it a superior imaging tool compared to conventional CT imaging modalities.

Chapter 2 investigated the effect of external parameters such as temperature, field of view and decalcification on the assessment of bone density and morphology. This study also led to the development of a bone analysis tool which is integrated into MARS visualisation software for morphological quantification.

Chapter 3 described the process of optimising a protocol for imaging bone-metal interfaces and how changes in acquisition parameters affect signal-to-noise ratio and image quality.

Chapter 4 discussed the assessment of metal induced artefacts on tissue density using spectral photon counting CT. Qualitative comparison of bone-metal interface with clinical single and dual energy CT was performed.

Chapter 5 demonstrated the clinical potential of MARS spectral photon counting CT in quantifying bone healing at the bone-metal interface. The bone mineral content

quantified from spectral photon counting CT was compared with iDXA.

Chapter 6 confirmed the diagnostic utility of spectral photon counting CT in differentiating calcium crystals inducing crystal arthritis. The results obtained were validated against XRD and polarised light microscopy.

7.2 Conclusion

MARS spectral photon counting CT is a potential tool to identify and monitor slight changes in bone mineral density and morphology. Improved spectral and spatial resolution of MARS spectral CT might enable earlier detection of osteoporosis and monitor response to the treatment. The MARS human and arm scanner uses the same hardware and software as the preclinical scanner. The protocol optimised for imaging biological samples with implants in the preclinical scanner should be altered to achieve optimal imaging while translating to human imaging. MARS CT scanner can accurately quantify tissue density outside the implant with reduced artefacts. However, there is an overestimation of tissue density within the pores of the scaffold due to artefacts. Qualitative evaluation of different biological samples with clinical single and dual energy CT demonstrates that MARS CT is a potential tool for evaluating bone-metal interface. The high spatial resolution as well as artefact less bone-metal interface enables earlier detection of bone healing. MARS spectral photon counting CT can differentiate crystal types inducing arthritis non-invasively.

7.3 Future work

Photon counting spectral imaging is rapidly becoming accepted as the next major advance in hospital x-ray scanners with several manufacturers developing prototype system (MARS Bioimaging Ltd., Philips, Siemens). The human ethics approval (approval no: 18/STH/221 from the NZ Ministry of Health (MoH), Health and Disability ethics Committee) permits scanning patients and volunteers. These patients will have a range of osteoporosis conditions from normal, through to advanced disease,

to complications such as fracture, and various stages of drug therapy. A finite element model analysis will be developed to evaluate the bio mechanical behaviour of bone under various loading condition to predict fracture risk. The improvisation of the bone analysis tool incorporating more morphological parameters such as volume fraction and structure model index will be an added advantage to quantify bone strength.
The major challenges in the clinical implementation of the scanner is the scanning time and the reconstruction time. The advancement in the Medipix chip design such as redesigning the chip geometry to tile it on all the four sides and increasing the sensor area will improve the count rate capability and energy resolution. Proper modelling of the pulse pile up effect will reduce the scanning time. Splitting the data set into different energy bins and processing it simultaneously will reduce the reconstruction time. Use of graphics processing unit (GPU) to perform computations handled by the central processing unit (CPU) can reduce the computational time and improve the efficiency of handling large data sets. The application of artificial intelligence in spectral CT imaging can effectively improve image interpretation, diagnosis of disease and provide suggestions for treatment. Advancement in the material reconstruction techniques to reduce artefacts even in low energy bins is essential to improve material differentiation and quantification. Adding respiratory gating, motion correction, and better anesthetics to the scanner will enable cardiovascular and lung imaging.
In conclusion, photon counting spectral CT scanners have the potential to be used as the next generation clinical scanners due to the following applications:

1. The ability to spatially locate fracture risk bone sites in advance, visualise bone-metal interface with fewer artefacts, quantify new bone growth during treatment, distinguish between different crystals inducing arthritis, and detection of earlier degradation of osteoarthritic cartilage will potentially replace traditional CT systems with spectral CT in orthopaedic applications.

2. The capability to identify tissue type and quantify disease activity in plaques using potential imaging targets will provide cardiologists better understanding and early detection of cardiovascular diseases.

3. The potential to quantify targeted nanoparticles will help clinicians in better

characterisation of tumours, and monitoring of drug delivery making it a cost effective alternative choice for radiotracers.

4. The technology embodied in photon counting spectral CT will spur drug development, enable rapid assessment of the efficiency of the new drugs for the treatment and prevention of diseases making it a potential choice for precision medicine and treatment planning.

References

Aamir, R., Viry, A., Kirkbride, T., Rajeswari Amma, M., Stamp, L., Polson, M., Guyen, O., Becce, F., and Anderson, N. (2018). Characterisation of calcium crystal types in osteoarthritic meniscus at spectral photon-counting CT.

Adams, J. E. (2013). Advances in bone imaging for osteoporosis. *Nature Reviews Endocrinology*, **9**(1), 28.

Agarwal, S., Sharma, R. K., and Jain, J. K. (2014). Periprosthetic fractures after total knee arthroplasty. *Journal of Orthopaedic Surgery*, **22**(1), 24–29.

Ahmed, N., Fleming, D. E., and O'Meara, J. M. (2004). Monte carlo investigations of distance-dependent effects on energy deposition in k-shell x-ray fluorescence bone lead measurement. *Physics in Medicine & Biology*, **49**(17), N267.

Alvarez, R. E. and Macovski, A. (1976). Energy-selective reconstructions in x-ray computerised tomography. *Physics in Medicine & Biology*, **21**(5), 733.

Amma, M., Tara, D., Aliakbar, A., Aamir, Y. R., Nigel, A., Benjamin, B., and Anthony, B. (2018). Optimisation of parameters for imaging bone metal interface using spectral photon counting computed tomography. *Journal of Medical Radiation Sciences*, **65**, 116–117.

Amma, M. R., Butler, A. P., Raja, A. Y., Bamford, B., Butler, P., Walker, E. P., Matanaghi, A., Adebileje, S. A., Anderson, N., Anjomrouz, M., *et al.* (2019). Assessment of metal implant induced artefacts using photon counting spectral CT. In *Developments in X-Ray Tomography XII*, volume 11113, page 111131D. International Society for Optics and Photonics.

Anderson, N., Butler, A., Scott, N., Cook, N., Butzer, J., Schleich, N., Firsching, M., Grasset, R., De Ruiter, N., Campbell, M., *et al.* (2010). Spectroscopic (multi-energy) CT distinguishes iodine and barium contrast material in mice. *European radiology*, **20**(9), 2126–2134.

Augat, P. and Schorlemmer, S. (2006). The role of cortical bone and its microstructure in bone strength. *Age and ageing*, **35**(suppl_2), ii27–ii31.

Ballabriga, R. (2009). *The Design and Implementation in 0.13μm CMOS of an Algorithm Permitting Spectroscopic Imaging with High Spatial Resolution for Hybrid Pixel Detectors*. Ph.D. thesis, CERN.

Ballabriga, R., Alozy, J., Blaj, G., Campbell, M., Fiederle, M., Frojdh, E., Heijne, E., Llopart, X., Pichotka, M., Procz, S., *et al.* (2013). The Medipix3RX: a high resolution, zero dead-time pixel detector readout chip allowing spectroscopic imaging. *Journal of Instrumentation*, **8**(02), C02016.

Ballabriga, R., Alozy, J., Campbell, M., Frojdh, E., Heijne, E., Koenig, T., Llopart, X., Marchal, J., Pennicard, D., Poikela, T., *et al.* (2016). Review of hybrid pixel detector readout ASICs for spectroscopic x-ray imaging. *Journal of Instrumentation*, **11**(01), P01007.

Ballabriga, R., Campbell, M., and Llopart, X. (2018). ASIC developments for radiation imaging applications: The Medipix and Timepix family. *Nuclear Instruments and Methods in Physics Research Section A: Accelerators, Spectrometers, Detectors and Associated Equipment*, **878**, 10–23.

Bamberg, F., Dierks, A., Nikolaou, K., Reiser, M. F., Becker, C. R., and Johnson, T. R. (2011). Metal artifact reduction by dual energy computed tomography using monoenergetic extrapolation. *European radiology*, **21**(7), 1424–1429.

Barrett, J. F. and Keat, N. (2004). Artifacts in CT: recognition and avoidance. *Radiographics*, **24**(6), 1679–1691.

Bateman, C., Knight, D., Brandwacht, B., Mc Mahon, J., Healy, J., Panta, R., Aamir, R., Rajendran, K., Moghiseh, M., Ramyar, M., *et al.* (2018). MARS-MD: rejection

based image domain material decomposition. *Journal of Instrumentation*, **13**(05), P05020.

Bech, M., Bunk, O., David, C., Kraft, P., Brönnimann, C., Eikenberry, E., and Pfeiffer, F. (2008). X-ray imaging with the PILATUS 100k detector. *Applied Radiation and Isotopes*, **66**(4), 474–478.

Bechara, B., Moore, W., McMahan, C., and Noujeim, M. (2012). Metal artefact reduction with cone beam CT: an in vitro study. *Dentomaxillofacial Radiology*, **41**(3), 248–253.

Beutel, J., Kundel, H. L., and Van Metter, R. L. (2000). *Handbook of medical imaging*, volume 1. SPIE Press.

Boas, F. E. and Fleischmann, D. (2012). CT artifacts: causes and reduction techniques. *Imaging in Medicine*, **4**(2), 229–240.

Bonnick, S. L. and Shulman, L. (2006). Monitoring osteoporosis therapy: bone mineral density, bone turnover markers, or both? *The American journal of medicine*, **119**(4), S25–S31.

Boone, J. (2019).

Bosley, C. and Miles, K. (2009). https://nzoa.org.nz/system/files/The Crippling Burden.pdf.

Bouxsein, M. L. and Seeman, E. (2009). Quantifying the material and structural determinants of bone strength. *Best practice & research Clinical rheumatology*, **23**(6), 741–753.

Briggs, A. M., Perilli, E., Parkinson, I. H., Wrigley, T. V., Fazzalari, N. L., Kantor, S., and Wark, J. D. (2010). Novel assessment of subregional bone mineral density using DXA and pQCT and subregional microarchitecture using micro-CT in whole human vertebrae: applications, methods, and correspondence between technologies. *Journal of Clinical Densitometry*, **13**(2), 161–174.

Brook, O. R., Gourtsoyianni, S., Brook, A., Mahadevan, A., Wilcox, C., and Raptopoulos, V. (2012). Spectral CT with metal artifacts reduction software for improvement of tumor visibility in the vicinity of gold fiducial markers. *Radiology*, **263**(3), 696–705.

Bugaev, A. S., Eroshkin, P. A., Romanko, V. A., and Sheshin, E. P. (2013). Low-power x-ray tubes (the current state). *Physics-Uspekhi*, **56**(7), 691.

Butler, P. H., Adebileje, S. A., Alexander, S. D., Amma, M. R., Amjomrouz, M., Aghariomabad, F., Atharifard, A., Atlas, J., Bamford, B., Bell, S. T., *et al.* (2019). MARS pre-clinical imaging: the benefits of small pixels and good energy data. In *Developments in X-Ray Tomography XII*, volume 11113, page 111130C. International Society for Optics and Photonics.

Carter, D. R. and Beaupré, G. S. (2007). *Skeletal function and form: mechanobiology of skeletal development, aging, and regeneration*. Cambridge University Press.

Castania, V. A., Silveira, J. W. d. S. d., Issy, A. C., Pitol, D. L., Castania, M. L., Neto, A. D., Del Bel, E. A., and Defino, H. L. A. (2015). Advantages of a combined method of decalcification compared to EDTA. *Microscopy research and technique*, **78**(2), 111–118.

Chen, W., Cormode, D. P., Fayad, Z. A., and Mulder, W. J. (2011). Nanoparticles as magnetic resonance imaging contrast agents for vascular and cardiac diseases. *Wiley Interdisciplinary Reviews: Nanomedicine and Nanobiotechnology*, **3**(2), 146–161.

Chen, W. T., Han, D. C., Zhang, P. X., Han, N., Kou, Y. H., Yin, X. F., and Jiang, B. G. (2015). A special healing pattern in stable metaphyseal fractures. *Acta orthopaedica*, **86**(2), 238–242.

Cheung, A. M., Adachi, J. D., Hanley, D. A., Kendler, D. L., Davison, K. S., Josse, R., Brown, J. P., Ste-Marie, L.-G., Kremer, R., Erlandson, M. C., *et al.* (2013). High-resolution peripheral quantitative computed tomography for the assessment of bone strength and structure: a review by the canadian bone strength working group. *Current osteoporosis reports*, **11**(2), 136–146.

Codreanu, C. and Enache, L. (2015). Is ultrasound changing the way we understand rheumatology? including ultrasound examination in the classification criteria of polymyalgia rheumatica and gout. *Medical ultrasonography*, **17**(1), 97.

Corrales, L. A., Morshed, S., Bhandari, M., and Miclau III, T. (2008). Variability in the assessment of fracture-healing in orthopaedic trauma studies. *The Journal of Bone and Joint Surgery. American volume.*, **90**(9), 1862.

Davis, B., Roberts, P., Moorcroft, C., Brown, M., Thomas, P., and Wade, R. (2004). Reliability of radiographs in defining union of internally fixed fractures. *Injury*, **35**(6), 557–561.

De Ruiter, N. J., Butler, P. H., Butler, A. P., Bell, S. T., Chernoglazov, A. I., and Walsh, M. F. (2017). MARS imaging and reconstruction challenges. In *Proceedings of the 14th International Meeting on Fully Three-Dimensional Image Reconstruction in Radiology and Nuclear Medicine, Xi'an, China*, pages 18–23.

Delpierre, P. (2014). A history of hybrid pixel detectors, from high energy physics to medical imaging. *Journal of Instrumentation*, **9**(05), C05059.

Desai, M. A., Peterson, J. J., Garner, H. W., and Kransdorf, M. J. (2011). Clinical utility of dual-energy CT for evaluation of tophaceous gout. *Radiographics*, **31**(5), 1365–1375.

Dirim, B., Resnick, D., Abreu, M., Wangwinyuvirat, M., Trudell, D. J., and Haghighi, P. (2013). Relationship between the degeneration of the cruciate ligaments and calcium pyrophosphate dihydrate crystal deposition: anatomic, radiologic study with histologic correlation. *Clinical imaging*, **37**(2), 342–347.

Doube, M., Kłosowski, M. M., Arganda-Carreras, I., Cordelières, F. P., Dougherty, R. P., Jackson, J. S., Schmid, B., Hutchinson, J. R., and Shefelbine, S. J. (2010). BoneJ: free and extensible bone image analysis in ImageJ. *Bone*, **47**(6), 1076–1079.

Douglas-Akinwande, A. C., Buckwalter, K. A., Rydberg, J., Rankin, J. L., and Choplin, R. H. (2006). Multichannel CT: evaluating the spine in postoperative patients with orthopedic hardware. *Radiographics*, **26**(suppl_1), S97–S110.

El Maghraoui, A. and Roux, C. (2008). DXA scanning in clinical practice. *QJM: An International Journal of Medicine*, **101**(8), 605–617.

Felsenberg, D. and Boonen, S. (2005). The bone quality framework: determinants of bone strength and their interrelationships, and implications for osteoporosis management. *Clinical therapeutics*, **27**(1), 1–11.

Fornaro, J., Leschka, S., Hibbeln, D., Butler, A., Anderson, N., Pache, G., Scheffel, H., Wildermuth, S., Alkadhi, H., and Stolzmann, P. (2011). Dual-and multi-energy CT: approach to functional imaging. *Insights into imaging*, **2**(2), 149–159.

Freire, V., Moser, T. P., and Lepage-Saucier, M. (2018). Radiological identification and analysis of soft tissue musculoskeletal calcifications. *Insights into imaging*, **9**(4), 477–492.

Fripp, J., Crozier, S., Warfield, S. K., and Ourselin, S. (2007). Automatic segmentation of the bone and extraction of the bone–cartilage interface from magnetic resonance images of the knee. *Physics in Medicine & Biology*, **52**(6), 1617.

Gerstenfeld, L. and Einhorn, T. (2003). Developmental aspects of fracture healing and the use of pharmacological agents to alter healing. *Journal of Musculoskeletal and Neuronal Interactions*, **3**(4), 297–303.

Giavarina, D. (2015). Understanding bland altman analysis. *Biochemia medica: Biochemia medica*, **25**(2), 141–151.

Goldhahn, J., Jenet, A., Schneider, E., and Christoph, A. L. (2005). Slow rebound of cancellous bone after mainly steroid-induced osteoporosis in ovariectomized sheep. *Journal of orthopaedic trauma*, **19**(1), 23–28.

Gordon, C., Lang, T., Augat, P., and Genant, H. (1998). Image-based assessment of spinal trabecular bone structure from high-resolution CT images. *Osteoporosis international*, **8**(4), 317–325.

Grajo, J. R., Patino, M., Prochowski, A., and Sahani, D. V. (2016). Dual energy CT in practice: basic principles and applications. *Appl Radiol*, **45**(7), 6–12.

Grigoryan, M., Lynch, J. A., Fierlinger, A. L., Guermazi, A., Fan, B., MacLean, D. B., MacLean, A., and Genant, H. K. (2003). Quantitative and qualitative assessment of closed fracture healing using computed tomography and conventional radiography1. *Academic radiology*, **10**(11), 1267–1273.

Guerra, P., Santos, A., and Darambara, D. (2009). An investigation of performance characteristics of a pixellated room-temperature semiconductor detector for medical imaging. *Journal of Physics D: Applied Physics*, **42**(17), 175101.

Hargreaves, B. A., Worters, P. W., Pauly, K. B., Pauly, J. M., Koch, K. M., and Gold, G. E. (2011). Metal-induced artifacts in MRI. *American Journal of Roentgenology*, **197**(3), 547–555.

Heismann, B., Leppert, J., and Stierstorfer, K. (2003). Density and atomic number measurements with spectral x-ray attenuation method. *Journal of applied physics*, **94**(3), 2073–2079.

Heismann, B., Henseler, D., Niederloehner, D., Hackenschmied, P., Strassburg, M., Janssen, S., and Wirth, S. (2008). Spectral and spatial resolution of semiconductor detectors in medical x-and gamma ray imaging. In *2008 IEEE Nuclear Science Symposium Conference Record*, pages 78–83. IEEE.

Hildebrand, T. and Rüegsegger, P. (1997). A new method for the model-independent assessment of thickness in three-dimensional images. *Journal of microscopy*, **185**(1), 67–75.

Hooper, G., Lee, A. J., Rothwell, A., and Frampton, C. (2014). Current trends and projections in the utilisation rates of hip and knee replacement in New Zealand from 2001 to 2026. *The New Zealand Medical Journal (Online)*, **127**(1401), 82.

Hsu, J.-T., Chen, Y.-J., Ho, J.-T., Huang, H.-L., Wang, S.-P., Cheng, F.-C., Wu, J., and Tsai, M.-T. (2014). A comparison of micro-CT and dental CT in assessing cortical bone morphology and trabecular bone microarchitecture. *PLoS One*, **9**(9), e107545.

Huttunen, T. T., Launonen, A. P., Berg, H. E., Lepola, V., Felländer-Tsai, L., and Mattila, V. M. (2016). Trends in the incidence of clavicle fractures and surgical repair in Sweden: 2001-2012. *JBJS*, **98**(21), 1837–1842.

Huynh, T., Gao, Y., Kang, J., Wang, L., Zhang, P., Lian, J., and Shen, D. (2015). Estimating CT image from MRI data using structured random forest and auto-context model. *IEEE transactions on medical imaging*, **35**(1), 174–183.

Jacques, T., Michelin, P., Badr, S., Nasuto, M., Lefebvre, G., Larkman, N., and Cotten, A. (2017). Conventional radiology in crystal arthritis: Gout, calcium pyrophosphate deposition, and basic calcium phosphate crystals. *Radiologic Clinics*, **55**(5), 967–984.

Johnson, T., Fink, C., Schönberg, S. O., and Reiser, M. F. (2011). *Dual energy CT in clinical practice*. Springer Science & Business Media.

Kalender, W. A., Buchenau, S., Deak, P., Kellermeier, M., Langner, O., van Straten, M., Vollmar, S., and Wilharm, S. (2008). Technical approaches to the optimisation of CT. *Physica Medica*, **24**(2), 71–79.

Kalkwarf, H., Laor, T., and Bean, J. A. (2011). Fracture risk in children with a forearm injury is associated with volumetric bone density and cortical area (by peripheral QCT) and areal bone density (by DXA). *Osteoporosis international*, **22**(2), 607–616.

Kanis, J., McCloskey, E., Johansson, H., Oden, A., Ström, O., and Borgström, F. (2010). Development and use of FRAX® in osteoporosis. *Osteoporosis international*, **21**(2), 407–413.

Kirkbride, T. E., Raja, A. Y., Müller, K., Bateman, C. J., Becce, F., and Anderson, N. G. (2017). Discrimination between calcium hydroxyapatite and calcium oxalate using multienergy spectral photon-counting ct. *American Journal of Roentgenology*, **209**(5), 1088–1092.

Kooistra, B. W., Dijkman, B. G., Busse, J. W., Sprague, S., Schemitsch, E. H., and Bhandari, M. (2010). The radiographic union scale in tibial fractures: reliability and validity. *Journal of orthopaedic trauma*, **24**, S81–S86.

Kuhnigk, J.-M., Dicken, V., Bornemann, L., Bakai, A., Wormanns, D., Krass, S., and Peitgen, H.-O. (2006). Morphological segmentation and partial volume analysis for volumetry of solid pulmonary lesions in thoracic CT scans. *IEEE transactions on medical imaging*, **25**(4), 417–434.

Lee, Y. H., Park, K. K., Song, H.-T., Kim, S., and Suh, J.-S. (2012). Metal artefact reduction in gemstone spectral imaging dual-energy CT with and without metal artefact reduction software. *European radiology*, **22**(6), 1331–1340.

Lespessailles, E., Chappard, C., Bonnet, N., and Benhamou, C. L. (2006). Imaging techniques for evaluating bone microarchitecture. *Joint bone spine*, **73**(3), 254–261.

Lill, C. A., Fluegel, A. K., and Schneider, E. (2000). Sheep model for fracture treatment in osteoporotic bone: a pilot study about different induction regimens. *Journal of orthopaedic trauma*, **14**(8), 559–565.

Lin, S.-K., Kok, S.-H., Kuo, M. Y.-P., Lee, M.-S., Wang, C.-C., Lan, W.-H., Hsiao, M., Goldring, S. R., and Hong, C.-Y. (2003). Nitric oxide promotes infectious bone resorption by enhancing cytokine-stimulated interstitial collagenase synthesis in osteoblasts. *Journal of bone and mineral research*, **18**(1), 39–46.

Link, T. M. (2012). Osteoporosis imaging: state of the art and advanced imaging. *Radiology*, **263**(1), 3–17.

Link, T. M., Majumdar, S., Lin, J. C., Newitt, D., Augat, P., Ouyang, X., Mathur, A., and Genant, H. K. (1998). A comparative study of trabecular bone properties in the spine and femur using high resolution MRI and CT. *Journal of bone and mineral research*, **13**(1), 122–132.

Liu, H., Zhu, R., Liu, C., Ma, R., Wang, L., Chen, B., Li, L., Niu, J., Zhao, D., Mo, F., *et al.* (2017). Evaluation of decalcification techniques for rat femurs using HE and immunohistochemical staining. *BioMed research international*, **2017**.

Liu, X., Yu, L., Primak, A. N., and McCollough, C. H. (2009). Quantitative imaging of element composition and mass fraction using dual-energy CT: Three-material decomposition. *Medical physics*, **36**(5), 1602–1609.

Löffler, C., Sattler, H., Peters, L., Löffler, U., Uppenkamp, M., and Bergner, R. (2015). Distinguishing gouty arthritis from calcium pyrophosphate disease and other arthritides. *The Journal of rheumatology*, **42**(3), 513–520.

Lohman, M., Kivisaari, A., Kallio, P., Puntila, J., Vehmas, T., and Kivisaari, L. (2001). Acute paediatric ankle trauma: MRI versus plain radiography. *Skeletal radiology*, **30**(9), 504–511.

Lufkin, E. G., Wahner, H. W., O'Fallon, W. M., Hodgson, S. F., Kotowicz, M. A., Lane, A. W., Judd, H. L., Caplan, R. H., and Riggs, B. L. (1992). Treatment of postmenopausal osteoporosis with transdermal estrogen. *Annals of internal medicine*, **117**(1), 1–9.

Lusic, H. and Grinstaff, M. W. (2012). X-ray-computed tomography contrast agents. *Chemical reviews*, **113**(3), 1641–1666.

MacMullan, P., McMahon, G., and McCarthy, G. (2011). Detection of basic calcium phosphate crystals in osteoarthritis. *Joint Bone Spine*, **78**(4), 358–363.

Mandalika, V. B. H., Chernoglazov, A. I., Billinghurst, M., Bartneck, C., Hurrell, M. A., De Ruiter, N., Butler, A. P., and Butler, P. H. (2018). A hybrid 2d/3d user interface for radiological diagnosis. *Journal of digital imaging*, **31**(1), 56–73.

Matanaghi, A., Raja, A., Leary, C., Amma, M. R., Panta, R., Anjomrouz, M., Moghiseh, M., Butler, A., Bamford, B., Collaboration, M., *et al.* (2019). Semi-automatic quantitative assessment of site-specific bone health using spectral photon counting CT. *Journal of Nuclear Medicine*, **60**(supplement 1), 1297–1297.

Medjoubi, K., Bucaille, T., Hustache, S., Bérar, J.-F., Boudet, N., Clemens, J.-C., Delpierre, P., and Dinkespiler, B. (2010). Detective quantum efficiency, modulation transfer function and energy resolution comparison between cdte and silicon sensors bump-bonded to XPAD3S. *Journal of synchrotron radiation*, **17**(4), 486–495.

Meganck, J. A., Kozloff, K. M., Thornton, M. M., Broski, S. M., and Goldstein, S. A. (2009). Beam hardening artifacts in micro-computed tomography scanning can be

reduced by x-ray beam filtration and the resulting images can be used to accurately measure BMD. *Bone*, **45**(6), 1104–1116.

Meyer, E., Raupach, R., Lell, M., Schmidt, B., and Kachelrieß, M. (2010). Normalized metal artifact reduction (NMAR) in computed tomography. *Medical physics*, **37**(10), 5482–5493.

Meyer, E., Raupach, R., Lell, M., Schmidt, B., and Kachelrieß, M. (2012). Frequency split metal artifact reduction (FSMAR) in computed tomography. *Medical physics*, **39**(4), 1904–1916.

Mohsen (2017). *MARS spectral CT technology for simultaneous assessment of articular cartilage and bone*. Ph.D. thesis, University of Otago.

Morgan, M. P., Cooke, M. M., and McCarthy, G. M. (2005). Microcalcifications associated with breast cancer: an epiphenomenon or biologically significant feature of selected tumors? *Journal of mammary gland biology and neoplasia*, **10**(2), 181–187.

Mori, I., Machida, Y., Osanai, M., and Iinuma, K. (2013). Photon starvation artifacts of x-ray CT: their true cause and a solution. *Radiological physics and technology*, **6**(1), 130–141.

Morshed, S. (2014). Current options for determining fracture union. *Advances in medicine*, **2014**.

Nicolaou, S., Yong-Hing, C. J., Galea-Soler, S., Hou, D. J., Louis, L., and Munk, P. (2010). Dual-energy CT as a potential new diagnostic tool in the management of gout in the acute setting. *American Journal of Roentgenology*, **194**(4), 1072–1078.

Oei, L., Koromani, F., Rivadeneira, F., Zillikens, M. C., and Oei, E. H. (2016). Quantitative imaging methods in osteoporosis. *Quantitative imaging in medicine and surgery*, **6**(6), 680.

Panta, R. K., Walsh, M. F., Bell, S. T., Anderson, N. G., Butler, A. P., and Butler, P. H. (2014). Energy calibration of the pixels of spectral x-ray detectors. *IEEE transactions on medical imaging*, **34**(3), 697–706.

Panta, R. K., Butler, A. P., Butler, P. H., de Ruiter, N. J., Bell, S. T., Walsh, M. F., Doesburg, R. M., Chernoglazov, A. I., Goulter, B. P., Carbonez, P., *et al.* (2018). First human imaging with MARS photon-counting CT. In *2018 IEEE Nuclear Science Symposium and Medical Imaging Conference Proceedings (NSS/MIC)*, pages 1–7. IEEE.

Pappou, I. P., Girardi, F. P., Sandhu, H. S., Parvataneni, H. K., Cammisa Jr, F. P., Schneider, R., Frelinghuysen, P., and Lane, J. M. (2006). Discordantly high spinal bone mineral density values in patients with adult lumbar scoliosis. *Spine*, **31**(14), 1614–1620.

Pascual, E. and Sivera, F. (2011). Synovial fluid crystal analysis. *SD-Gout & Other Crystal Arthropathies E-Book: Expert Consult: Online and Print*, page 20.

Pearce, A., Richards, R., Milz, S., Schneider, E., Pearce, S., *et al.* (2007). Animal models for implant biomaterial research in bone: a review. *Eur Cell Mater*, **13**(1), 1–10.

Perilli, E., Briggs, A. M., Kantor, S., Codrington, J., Wark, J. D., Parkinson, I. H., and Fazzalari, N. L. (2012). Failure strength of human vertebrae: prediction using bone mineral density measured by DXA and bone volume by micro-CT. *Bone*, **50**(6), 1416–1425.

Poludniowski, G., Landry, G., DeBlois, F., Evans, P., and Verhaegen, F. (2009). Spekcalc: a program to calculate photon spectra from tungsten anode x-ray tubes. *Physics in Medicine & Biology*, **54**(19), N433.

Popovtzer, R., Agrawal, A., Kotov, N. A., Popovtzer, A., Balter, J., Carey, T. E., and Kopelman, R. (2008). Targeted gold nanoparticles enable molecular CT imaging of cancer. *Nano letters*, **8**(12), 4593–4596.

Raja, A., Moghiseh, M., Bateman, C., de Ruiter, N., Schon, B., Schleich, N., Woodfield, T., Butler, A., and Anderson, N. (2018). Measuring identification and quantification errors in spectral CT material decomposition. *Applied Sciences*, **8**(3), 467.

Rajendran, K. (2016). *MARS spectral CT technology for orthopaedic applications.* Ph.D. thesis, University of Otago.

Rajendran, K., Walsh, M., De Ruiter, N., Chernoglazov, A., Panta, R., Butler, A., Butler, P., Bell, S., Anderson, N., Woodfield, T., *et al.* (2014). Reducing beam hardening effects and metal artefacts in spectral CT using Medipix3RX. *Journal of Instrumentation*, **9**(03), P03015.

Rajendran, K., Löbker, C., Schon, B. S., Bateman, C. J., Younis, R. A., de Ruiter, N. J., Chernoglazov, A. I., Ramyar, M., Hooper, G. J., Butler, A. P., *et al.* (2017). Quantitative imaging of excised osteoarthritic cartilage using spectral CT. *European radiology*, **27**(1), 384–392.

Rajiah, P., Sundaram, M., and Subhas, N. (2019). Dual-energy CT in musculoskeletal imaging: What is the role beyond gout? *American Journal of Roentgenology*, pages 1–13.

Richmond, C. (2004). Sir godfrey hounsfield.

Rinkel, J., Dillon, W. P., Funk, T., Gould, R., and Prevrhal, S. (2008). Computed tomographic metal artifact reduction for the detection and quantitation of small features near large metallic implants: a comparison of published methods. *Journal of computer assisted tomography*, **32**(4), 621–629.

Ronaldson, J. P., Zainon, R., Scott, N. J. A., Gieseg, S. P., Butler, A. P., Butler, P. H., and Anderson, N. G. (2012). Toward quantifying the composition of soft tissues by spectral CT with medipix3. *Medical physics*, **39**(11), 6847–6857.

Rosenthal, A. K. (2007). Update in calcium deposition diseases. *Current opinion in rheumatology*, **19**(2), 158–162.

Saito, T. and Toriwaki, J.-I. (1994). New algorithms for euclidean distance transformation of an n-dimensional digitized picture with applications. *Pattern recognition*, **27**(11), 1551–1565.

Santos, G. (2017). The importance of metallic materials as biomaterials. *Adv Tissue Eng Regen Med Open Access*, **3**(1), 00054.

Schindeler, A., McDonald, M. M., Bokko, P., and Little, D. G. (2008). Bone remodeling during fracture repair: The cellular picture. In *Seminars in cell & developmental biology*, volume 19, pages 459–466. Elsevier.

Schioppa, E. J. (2014). *The color of X-rays*. Ph.D. thesis, Ph. D. Thesis, University of Amsterdam.

Schlomka, J., Roessl, E., Dorscheid, R., Dill, S., Martens, G., Istel, T., Bäumer, C., Herrmann, C., Steadman, R., Zeitler, G., *et al.* (2008). Experimental feasibility of multi-energy photon-counting k-edge imaging in pre-clinical computed tomography. *Physics in Medicine & Biology*, **53**(15), 4031.

Searle, E. K., Butler, A. P., Raja, A. Y., Gieseg, S. P., Adebileje, S. A., Alexander, S. D., Amma, M. R., Anjomrouz, M., Asghariomabad, F., Atharifard, A., *et al.* (2018). Distinguishing iron and calcium using MARS spectral CT. In *2018 IEEE Nuclear Science Symposium and Medical Imaging Conference Proceedings (NSS/MIC)*, pages 1–4. IEEE.

Seong, W.-J., Conrad, H. J., and Hinrichs, J. E. (2009). Potential damage to bone–implant interface when measuring initial implant stability. *Journal of periodontology*, **80**(11), 1868–1874.

Shampo, M. A. and Kyle, R. A. (1996). Godfrey hounsfield—developer of computed tomographic scanning. In *Mayo Clinic Proceedings*, volume 71, page 990. Elsevier.

Shikhaliev, P. M. (2005). Beam hardening artefacts in computed tomography with photon counting, charge integrating and energy weighting detectors: a simulation study. *Physics in Medicine & Biology*, **50**(24), 5813.

Sousa, C., Azevedo, J., Silva, A., Viegas, C., Reis, R., Gomes, M., and Dias, I. (2014). Serum total and bone alkaline phosphatase levels and their correlation with serum minerals over the lifespan of sheep. *Acta Veterinaria Hungarica*, **62**(2), 205–214.

Srinivasan, B., Kopperdahl, D. L., Amin, S., Atkinson, E. J., Camp, J., Robb, R. A., Riggs, B. L., Orwoll, E. S., Melton, L., Keaveny, T. M., *et al.* (2012). Relationship of femoral neck areal bone mineral density to volumetric bone mineral density, bone size, and femoral strength in men and women. *Osteoporosis international*, **23**(1), 155–162.

Stamp, L. K., Anderson, N. G., Becce, F., Rajeswari, M., Polson, M., Guyen, O., Viry, A., Choi, C., Kirkbride, T. E., and Raja, A. Y. (2019). Clinical utility of multi-energy spectral photon-counting CT in crystal arthritis. *Arthritis & Rheumatology*.

Stradiotti, P., Curti, A., Castellazzi, G., and Zerbi, A. (2009). Metal-related artifacts in instrumented spine. techniques for reducing artifacts in CT and MRI: state of the art. *European Spine Journal*, **18**(1), 102–108.

Sun, H., Qiu, S., Lou, S., Liu, J., Li, C., and Jiang, G. (2004). A correction method for nonlinear artifacts in CT imaging. In *Engineering in Medicine and Biology Society, 2004. IEMBS'04. 26th Annual International Conference of the IEEE*, volume 1, pages 1290–1293. IEEE.

Symons, R., Cork, T. E., Sahbaee, P., Fuld, M. K., Kappler, S., Folio, L. R., Bluemke, D. A., and Pourmorteza, A. (2016). Low-dose lung cancer screening with photon-counting CT: a feasibility study. *Physics in Medicine & Biology*, **62**(1), 202.

Taguchi, K. and Iwanczyk, J. S. (2013). Vision 20/20: Single photon counting x-ray detectors in medical imaging. *Medical physics*, **40**(10).

Taguchi, K., Zhang, M., Frey, E. C., Wang, X., Iwanczyk, J. S., Nygard, E., Hartsough, N. E., Tsui, B. M., and Barber, W. C. (2011). Modeling the performance of a photon counting x-ray detector for CT: Energy response and pulse pileup effects. *Medical physics*, **38**(2), 1089–1102.

Tassani, S., Korfiatis, V., and Matsopoulos, G. (2014). Influence of segmentation on micro-CT images of trabecular bone. *Journal of microscopy*, **256**(2), 75–81.

Trudel, G., Koike, Y., Dinh, L., and Uhthoff, H. K. (2005). Thawing of frozen calcaneus bone specimens has no effect on the bone mineral density using dual energy x-ray

absorptiometry: a study in rabbits and humans. *Physiological measurement*, **26**(5), 769.

Turkyilmaz, I., Sennerby, L., Tumer, C., Yenigul, M., and Avci, M. (2006). Stability and marginal bone level measurements of unsplinted implants used for mandibular overdentures: a 1-year randomized prospective clinical study comparing early and conventional loading protocols. *Clinical oral implants research*, **17**(5), 501–505.

Viriyavejkul, P., Wilairatana, V., Tanavalee, A., and Jaovisidha, K. (2007). Comparison of characteristics of patients with and without calcium pyrophosphate dihydrate crystal deposition disease who underwent total knee replacement surgery for osteoarthritis. *Osteoarthritis and cartilage*, **15**(2), 232–235.

Viry, A., Raja, A. Y., Kirkbride, T. E., Choi, C., Stamp, L. K., Dalbeth, N., Combes, C., Verdun, F. R., Anderson, N. G., and Becce, F. (2018). Multi-energy spectral photon-counting CT in crystal-related arthropathies: initial experience and diagnostic performance in vitro. In *Medical Imaging 2018: Physics of Medical Imaging*, volume 10573, page 1057351. International Society for Optics and Photonics.

Wähnert, D., Hoffmeier, K. L., Lehmann, G., Fröber, R., Hofmann, G. O., and Mückley, T. (2009). Temperature influence on DXA measurements: bone mineral density acquisition in frozen and thawed human femora. *BMC musculoskeletal disorders*, **10**(1), 25.

Wang (2013). https://www.astm.org/Standards/ E1695.htm.

Weiss, S., Zimmermann, G., Pufe, T., Varoga, D., and Henle, P. (2009). The systemic angiogenic response during bone healing. *Archives of orthopaedic and trauma surgery*, **129**(7), 989–997.

Wu, X., Langan, D. A., Xu, D., Benson, T. M., Pack, J. D., Schmitz, A. M., Tkaczyk, E. J., Leverentz, J., and Licato, P. (2009). Monochromatic CT image representation via fast switching dual kVp. In *Medical Imaging 2009: Physics of Medical Imaging*, volume 7258, page 725845. International Society for Optics and Photonics.

Yazdi, M. and Mohammadi, M. (2017). Metal artifact reduction in dental computed tomography images based on sinogram segmentation using curvelet transform followed by hough transform. *Journal of medical signals and sensors*, **7**(3), 145.

Zainon, R., Ronaldson, J., Janmale, T., Scott, N., Buckenham, T., Butler, A., Butler, P., Doesburg, R., Gieseg, S., Roake, J., *et al.* (2012). Spectral CT of carotid atherosclerotic plaque: comparison with histology. *European radiology*, **22**(12), 2581–2588.

Zeller, H., Dufreneix, S., Clark, M., Butler, P., Butler, A., Cook, N., and Tlustos, L. (2009). Charge sharing between pixels in the spectral Medipix2 x-ray detector. In *2009 24th International Conference Image and Vision Computing New Zealand*, pages 363–366. IEEE.

Zhou, B., Wang, J., Yu, Y. E., Zhang, Z., Nawathe, S., Nishiyama, K. K., Rosete, F. R., Keaveny, T. M., Shane, E., and Guo, X. E. (2016). High-resolution peripheral quantitative computed tomography (HR-pQCT) can assess microstructural and biomechanical properties of both human distal radius and tibia: ex vivo computational and experimental validations. *Bone*, **86**, 58–67.

Zlowodzki, M., Zelle, B. A., Cole, P. A., Jeray, K., and McKee, M. D. (2005). Treatment of acute midshaft clavicle fractures: systematic review of 2144 fractures: on behalf of the evidence-based orthopaedic trauma working group. *Journal of orthopaedic trauma*, **19**(7), 504–507.